5-1-2010

Modeling mantle convection using an internal state variable model framework

Jesse Andrew Sherburn

MODELING MANTLE CONVECTION USING AN INTERNAL STATE VARIABLE MODEL FRAMEWORK

By

Jesse Andrew Sherburn

A Dissertation
Submitted to the Faculty of
Mississippi State University
in Partial Fulfillment of the Requirements
for the Degree of Doctor of Philosophy
in Mechanical Engineering
in the Department of Mechanical Engineering

Mississippi State, Mississippi

May 2010

MODELING MANTLE CONVECTION USING AN INTERNAL

STATE VARIABLE MODEL FRAMEWORK

By

Jesse Andrew Sherburn

Approved:

Mark F. Horstemeyer Professor of Mechanical Engineering (Director of Dissertation)	Douglas J. Bammann Professor of Mechanical Engineering (Committee Member)
D. Keith Walters Associate Professor of Mechanical Engineering (Committee Member)	Philip M. Gullett Assistant Professor of Civil and Environmental Engineering (Committee Member)
Haitham El Kadiri Assistant Professor of Mechanical Engineering (Committee Member)	David L. Marcum Professor of Mechanical Engineering (Graduate Coordinator)
Sarah A. Rajala Dean of the Bagley College of Engineering	

Name: Jesse Andrew Sherburn

Date of the Degree: May 1, 2010

Institution: Mississippi State University

Major Field: Mechanical Engineering

Major Professor: Dr. Mark F. Horstemeyer

Title of Study: MODELING MANTLE CONVECTION USING AN INTERNAL STATE VARIABLE MODEL FRAMEWORK

Pages in Study: 152

Candidate for Degree of Doctor of Philosophy

In the current study we developed an internal state variable (ISV) model based on the Bammann inelasticity internal state variable model (BIISV) to include damage, recrystallization, and texture development, which we then implemented into a mantle convection code, TERRA2D, to incorporate higher fidelity material behavior into mantle convection simulations. With experimental stress strain data found in the literature model constants for the BIISV model were determined for a number of geologic materials. The BIISV model was shown to be far superior to the steady state power law model currently used by the geologic community to capture the deformation of geologic materials. Once implemented and verified in TERRA2D the BIISV model revealed locations of hardened material that behaved like diverters in the cold thermal boundary layer that the power law model could never produce. These hardened regions could be a plausible reason for the current subduction zones present on the earth.

We then altered the BIISV model equation to include the effects of damage, recrystallization, and texture development in order to model possible weakening

mechanisms in the cold thermal boundary layer of the mantle. Inclusion of damage and recrystallization allowed the cold thermal boundary layer to mobilize and plunge downward into the hotter region below. Texture development increased the intensity of rotational flow within the hotter zone as cold boundary material plunged downward which aided in destabilizing the cold upper thermal boundary layer. The inclusion of an internal state variable model with damage, recrystallization, and texture development represents a significant advancement in handling deformational physics for mantle phenomena in a comprehensive, unified, and automatic manner.

Key words: internal state variable modeling, mantle convection, damage, recrystallization, texture

DEDICATION

I would like to dedicate this research first to my loving wife Kristi Lynn because without her support and sacrifice during my time in school this document could not have been realized, and second to my children Coralee Dale and Andrew Joseph who were born while pursuing my degree.

ACKNOWLEDGEMENTS

I would like to take the opportunity thank all those who helped me throughout the process of performing my research and writing this dissertation. I first want to thank my advisor Dr. Mark F. Horstemeyer who I first met at the International Conference on Creationism back in August 2003. Dr. Horstemeyer's guidance, encouragement, wisdom, and friendship have encouraged me to become a godly researcher in an ungodly world. I would next like to thank my committee member Dr. Douglas Bammann for his insight, guidance, and friendship during the process of my graduate education. He has taught me to think in ways I never thought possible. I would like to express gratitude to my other committee members, Dr. Keith Walters, Dr. Philip M. Gullett, and Dr. Haitham El Kadiri whose advice and willingness to listen have been invaluable in this process. I also want to thank the Center for Advanced Vehicular Systems and the James Worth Bagley College of Engineering for the financial support of this research.

Outside of Mississippi State University I would like to thank Dr. John Baumgardner for giving me the opportunity to work with him back in the summer of 2006 and graciously giving me the source code to TERRA, which this dissertation revolved around. His willingness to help me whenever I needed it will never be forgotten. I would also like to thank my church family at Bible Baptist Church, and specifically my pastor, Alan Garbutt, for the spiritual guidance during my time in school. Words cannot describe my appreciation to my wife, Kristi Lynn, for her sacrifice and encouragement

during this process. I also want to thank my young children Coralee Dale and Andrew Joseph who sometimes sat on my lap while I ran and postprocessed countless numbers of TERRA simulations. I also want to thank my parents, Joseph and Michele Sherburn, as well as my wife's parents Dale and Alicia Hess, for all their steadfast love and support.

Last and most importantly I want to thank my Creator, Savior, and Lord Jesus Christ who gave me the ability to understand His creation that He gave man to study. All I understand is because He gave me the understanding.

> Giving thanks unto the Father, which hath made us meet to be partakers of the inheritance of the saints in light: Who hath delivered us from the power of darkness, and hath translated us into the kingdom of his dear Son: In whom we have redemption through his blood, even the forgiveness of sins: Who is the image of the invisible God, the firstborn of every creature: For by him were all things created, that are in heaven, and that are in earth, visible and invisible, whether they be thrones, or dominions, or principalities, or powers: all things were created by him, and for him: And he is before all things, and by him all things consist.
>
> *Colossians 1:12-17*

TABLE OF CONTENTS

DEDICATION ii

ACKNOWLEDGEMENTS iii

LIST OF TABLES vii

LIST OF FIGURES viii

CHAPTER

I. INTRODUCTION 1

II. APPLICATION OF THE BAMMANN INELASTICITY INTERNAL STATE VARIABLE CONSTITUTIVE MODEL TO SILICATE MATERIALS 4

Introduction 4
Model Description 6
Kinematics 6
Continuum Balance Equations 9
Constitutive Equations 11
Internal State Variable Formulation 12
Hardening-Recovery ISV Equations 17
Experiments 18
Results 20
Discussion 27
Conclusions 33
References 34

III. TWO DIMENSIONAL MANTLE CONVECTION SIMULATIONS USING THE BAMMANN INELASTICTY INTERNAL STATE VARIABLE MODEL 38

Introduction 38
Model Description 41
Implementation 48

Step 1 48
Step 2 48
Step 3 49
Step 4 50
Step 5 50
Step 6 50
Step 7 51
Step 8 51
Numerical Simulations Setup 52
Results 65
Discussion and Conclusions 82
References 85

IV. MODELING DAMAGE, RECRYSTALLIZATION, AND TEXTURE USING AN INTERNAL STATE VARIABLE FRAMEWORK WITH APPLICATION TO MANTLE DYNAMICS PROCESSES 89

Introduction 89
Model Description 91
Numerical Simulations Setup 107
Results 111
Discussion and Conclusions 137
References 141

V. CONCLUSIONS AND FUTURE WORK 146

Conclusions 146
Future Work 147
Three Dimensional Implementation 147
Heterogeneous Grain Sizes 147
Pressure Dependence 147
Quantifying Heat Released During Avalanche Event 148
Model Constants for Olivine 148
Initialization of Damage and Thermal Cracks 148
Multiple Materials 149
Relationship between Recrystallization and Texture 149
Kinematic Hardening 150
Relate Texture Development to Seismic Anisotropy 150
Deep Earthquake Study 150
Length Scales 151
Shorter Time Scales 151
References 152

LIST OF TABLES

2.1 BIISV material constants for wet and dry polycrystalline olivine aggregates, lherzolite, Carrara Marble, and rock salt. Constants C_6-C_{12} are omitted because they are zero 24

2.2 Power law hardening parameters for dry olivine and lherzolite 28

3.1 Input parameters used for numerical simulations in this study.....53

3.2 Power law parameters used in this study 55

3.3 BIISV model parameters used in this study.....55

4.1 Stress invariant expressions for different stress states. Reproduced from Horstemeyer & Gokhale (1999).....95

4.2 BIISV model parameters used in this study.....98

4.3 Input parameters common to all the illustrative cases in this study 109

4.4 TERRA2D parametric study cases 110

LIST OF FIGURES

2.1 Illustration of multiplicative decomposition of the deformation gradient into elastic and inelastic parts 7

2.2 Comparison of model to experimental data for wet polycrystalline olivine 22

2.3 Comparison of model to experimental data for dry polycrystalline olivine 23

2.4 Comparison of model results to experimental data for lherzolite 25

2.5 Comparison of model results to experimental data for Carrara Marble for varying temperatures and strain rate 26

2.6 Comparison of model results to experimental data for rock salt 27

2.7 Comparison of BIISV model and power law model to experimental data for dry polycrystalline olivine for a varying strain rate history at 1573K 30

2.8 Comparison of BIISV model and power law model to the experimental data for lherzolite for a varying strain rate history at 1333K 31

2.9 Comparison of BIISV model and power law model to experimental data for lherzolite for a varying temperature history at a constant strain rate of 7.8e-5 s^{-1} 32

3.1 Comparison between the power law model used in Yang and Baumgardner, 2000, and BIISV model in the pertinent strain rate range at a temperature of 1000 K 57

3.2 Comparison between BIISV perfectly plastic case and BIISV viscoplastic case over the pertinent range of strain rates 59

3.3 Comparison of BIISV model correlation to Lherzolite experimental data (Carter and Ave'Lallemant, 1970) 60

3.4 Comparison of BIISV model and power law model to Lherzolite experimental data (Carter and Ave'Lallemant, 1970) for a varying strain rate history at 1333K.....62

3.5 Comparison of BIISV model and power law model to Lherzolite experimental data (Carter and Ave'Lallemant, 1970) for a varying temperature history at 7.8e-5 s^{-1} 63

3.6 Initial temperature fields for the lherzolite simulations. Plot (a) shows the temperatures for the case of internal heating with no basal heating. Plot (b) shows the initial temperatures for the case that includes both internal and basal heating 64

3.7 Viscosity contour plot for both a) power law model and b) BIISV model at the end of the first time step.....66

3.8 The first avalanche from case with internal heating only 67

3.9 The temperature field for the a) power law model and the b) BIISV model at the time just before the second set of avalanches occurs.....68

3.10 Temperature fields after the second set of avalanches in the a) power law model and the b) BIISV model 70

3.11 Horizontal surface velocity of both the power law model and BIISV model during the second set of avalanches.....71

3.12 Viscoplastic BIISV test simulation with the a) isotropic history variable and the b) temperature field at the end of the second set of avalanches indicating that hardened material persists and influences the subsequent flow pattern 73

3.13 Contours of a) plastic strain and b) strain rate for the viscoplastic BIISV test simulation. Note the enormous plastic strains in the earth's mantle (up to 2000%).....74

3.14 Comparison of horizontal surface velocities for the BIISV viscoplastic and BIISV perfectly plastic cases 75

3.15 Temperature fields for a case with internal heating only using the power law model constants for lherzolite. Snapshots in time at a) 135 Myr, b) 170 Myr, and c) 220 Myr.....76

3.16 Temperature fields for a case with internal heating only using the BIISV viscoplastic model for lherzolite. Snapshots in time at a) 150 Myr, b) 200 Myr, and c) 280 Myr....77

3.17 Isotropic hardening fields for case shown in Figure 3.16 using the BIISV viscoplastic model for lherzolite. Snapshots in time at a) 150 Myr, b) 200 Myr, and c) 280 Myr....78

3.18 Velocity magnitude contours for a) power law model at 220 Myr and b) BIISV viscoplastic model at 280 Myr....79

3.19 Temperature fields for the internally heated and basally heated simulation using the power law model constants for lherzolite. Snapshots in time at a) 15 Myr, b) 150 Myr, and c) 220 Myr....80

3.20 Temperature fields for the internally heated and basally heated simulation using the BIISV viscoplastic model constants for lherzolite. Snapshots in time at a) 17 Myr, b) 175 Myr, and c) 280 Myr....81

3.21 Isotropic hardening fields for the internally heated and basally heated simulation using the BIISV model constants for lherzolite. Snapshots in time at a) 17 Myr, b) 175 Myr, and c) 280 Myr....82

4.1 Damage accumulation versus inelastic strain for tension and shear stress states....95

4.2 Comparison between the BIISV model with and without inclusion of damage model for a tension test. The strain rate for this test was 1.0×10^{-5} s^{-1} at a temperature of 1000 K....100

4.3 Comparison between the BIISV base model and including recrystallization for different r_1 values. (Units for r_1 are MPa^{-2}). The strain rate for these tests was 1.0×10^{-4} s^{-1} at a temperature of 1200 K....103

4.4 Comparison between BIISV model in torsion with and without texture model. The strain rate involved in these tests was 1.0×10^{-7} s^{-1} at a temperature of 1000 K....106

4.5 Thermal and velocity boundary conditions for illustrative TERRA2D simulations....109

4.6 Temperature fields for the baseline BIISV Case 1. Snapshots in time at a) 50 Myr, b) 200 Myr, and c) 700 Myr.....112

4.7 Temperature fields for Case 2 with damage contribution only from the shear/torsion. Snapshots in time at a) 30 Myr, b) 50 Myr, and c) 200 Myr.....113

4.8 Temperature fields for Case 3 with damage only from tension/compression. Snapshots in time at a) 30 Myr, b) 50 Myr, and c) 200 Myr.....114

4.9 Temperature fields for Case 4 with damage only from triaxial deformation. Snapshots in time at a) 30 Myr, b) 50 Myr, and c) 200 Myr.....116

4.10 Plots of the damage field for the three damage cases at a time of 50 Myr a) torsion/shear component alone (Case 2), b) tension/compression component alone (Case 3), and c) triaxiality component alone (Case 4).....117

4.11 Temperature fields for Case 5 with all damage components active . Snapshots in time at a) 30 Myr, b) 50 Myr, and c) 200 Myr 119

4.12 Temperature fields for Case 6 with the recrystallization parameter $r_1 = 1000\ MPa^{-2}$. Snapshots in time at a) 30 Myr, b) 170 Myr, and c) 380 Myr.....121

4.13 Comparison of temperature fields from a) recrystallization Case 6 with $r_1 = 1000\ MPa^{-2}$ at 170 Myr and b) yield stress case with $\tau_y = 100$ MPa (reported in chapter three) at 150 Myr.....122

4.14 Temperature fields for Case 7 with recrystallization parameter $r_1 = 10\ MPa^{-2}$. Snapshots in time at a) 30 Myr, b) 170 Myr, and c) 380 Myr.....123

4.15 Temperature fields for Case 8 with recrystallization parameter $r_1 = 0.1\ MPa^{-2}$. Snapshots in time at a) 50 Myr, b) 200 Myr, and c) 700 Myr.....125

4.16 Isotropic hardening fields for the three recrystallization cases at 170 Myr for a) $r_1 = 1000\ MPa^{-2}$(Case 6), b) $r_1 = 10\ MPa^{-2}$(Case 7), and c) $r_1 = 0.1\ MPa^{-2}$(Case 8) 126

4.17 Temperature fields for Case 9 with texture development and no initial texture. Snapshots in time at a) 50 Myr, b) 200 Myr, and c) 600 Myr.....128

4.18 Temperature fields for Case 10 with texture development and initial plane strain texture. Snapshots in time at a) 50 Myr, b) 200 Myr, and c) 600 Myr.....129

4.19 Temperature fields for Case 11 with texture development and initial shear texture. Snapshots in time at a) 50 Myr, b) 200 Myr, and c) 600 Myr.....130

4.20 Plots of velocity and temperature fields for texture cases at 180 Myr for a) no texture (Case 1), b) texture model with no initial history (Case 9), c) texture model with plane strain initial history (Case 10), and d) texture model with shear initial history (Case 11). Reference velocity vector is located in bottom left corner. 131

4.21 Plots of ISV tensor component A_{12} (a measure of texture development) for the different texture cases at 180 Myr for a) no initial history (Case 9) b) plane strain compression initial history (Case 10), and c) shear initial history (Case 11) 132

4.22 Temperature fields for Case 12 with damage, recrystalization, and texture all active. Snapshots in time at a) 30 Myr, b) 50 Myr, and c) 300 Myr.....134

4.23 Plots of damage accumulation for Case 12 with damage, recrystallization, and texture all active. Snapshots in time at a) 30 Myr, b) 50 Myr, and c) 300 Myr.....135

4.24 Plots of the ISV tensor component A_{12} (a measure of texture development) for Case 12 with damage, recrystalization, and texture all active. Snapshots in time at a) 30 Myr, b) 50 Myr, and c) 300 Myr 136

4.25 Plots of velocity and temperature fields for Case 12 with damage, recrystalization, and texture all active. Snapshot in time at a) 120 Myr, b) 300 Myr, and c) 530 Myr. Reference velocity vector is in lower left corner 137

CHAPTER 1

INTRODUCTION

The geologic community over the past 50 years has made amazing progress in our understanding of the solid Earth. Mantle convection has been recognized as the driving mechanism for plate tectonics, which explains earthquakes and volcanism on our planet. Due to the vast size scales involved with our Earth laboratory experiments can only give us some insight into the behavior of mantle convection. The only way to fully understand the mantle's role in the dynamics of the Earth is through computer simulations. With the advent of the modern computer and the ability to perform simulations on massively parallel computers the goal of accurately modeling the Earth's dynamics is becoming a reality.

This dissertation brings a sophisticated continuum material model to the geologic community that aids our understanding of silicate material and large geologic processes. An internal state variable model based on the Bammann inelasticity internal state variable (BIISV) model will be developed and applied to geologic materials in contrast to the power law model currently used by the community. The BIISV model has proven highly effective in describing the behavior of materials that deform due to the motion of dislocations. The community has been using a simple power law model to describe geologic material behavior for almost 40 years. The power law model inherently assumes steady state behavior and this simply is not the response of real materials even at larger

spatial and temporal scales. This work will address the need of a sophisticated material model for application to geologic materials.

The three main chapters of this dissertation were all submitted for publication as three separate documents prior to putting it together. The chapters were slightly modified to bring them together as one cohesive document.

The second chapter describes the BIISV model for application to silicate materials. The BIISV model equations are described as well as model calibration to stress strain data of a number of silicate materials. Contrasts are made the power law model to show the BIISV superiority to capture the transient behavior of silicate deformation.

Chapter three takes the BIISV model described in chapter two and implements into a mantle convection code, TERRA2D. The equations are briefly described, and the implementation using the radial return method is also described. The BIISV model in TERRA2D is then compared to previously published simulations using the power law model in TERRA2D to confirm the model works correctly. A different set of TERRA2D simulations are conducted that use experimentally based constants for both the BIISV and power law model.

Chapter four takes the implementation of BIISV into TERRA2D in chapter three and adds weakening mechanisms necessary to break up the upper thermal boundary layer of the upper mantle. Models for damage, recrystallization, and texture are described in the BIISV model framework. Each one of the models are used in TERRA2D simulations to show the changes in mantle convection dynamics. A simulation is also described that mixes all three of the models together to come up with a more realistic case of the breaking up of the upper thermal boundary layer in the upper mantle.

Chapter five will draw brief conclusions from the work done in chapters two, three, and four as well as describe future work that needs to be addressed regarding both mantle convection simulations and the enhanced BIISV model.

CHAPTER II

APPLICATION OF THE BAMMANN INELASTICITY INTERNAL STATE VARIABLE CONSTITUTIVE MODEL TO SILICATE MATERIALS

Introduction

The rheology of silicate materials plays a central role in the internal dynamics and thermal histories of planetary bodies. To gain accurate insight into the larger scale dynamical processes, we must ultimately understand the processes that govern the mechanical behavior of rocks at the microscale. Owing to its stability in laboratory conditions and its prevalence in the earth's upper mantle, our focus will be on the silicate mineral olivine. Considerable experimental effort has been undertaken over the last several decades to characterize the microstructural and mechanical behavior of olivine and olivine-rich rocks as described in reviews, for example by Nicolas and Poirier (1976), Carter (1976), Kirby (1983), Kirby and Kronenberg (1987), and Karato and Toriumi (1989).

The most commonly used model for representing the mechanical response of silicates under varying conditions has been a power law equation that depends on a hardening exponent, hardening coefficient, and activation energy (Kirby, 1983; Goetze, 1978; Frost and Ashby, 1982; Karato and Toriumi, 1989; Chopra and Paterson, 1981, 1984). Such power law models, however, do not possess in general the ability to include time dependent history effects that arise from temperature, strain rate, pressure, and

deformation path. As an example of an effort to overcome some of these limitations, Covey-Crump (1994) employed the Hart internal state variable model (1970, 1976) to study the mechanical properties of Carrara Marble. Aubertin et al. (1991, 1991) have also used an internal state variable model to analyze rock salt and other alkali halides.

Another shortcoming of the power law approach is the inability for one set of equations to model different deformation mechanisms. A different set of flow law equations and constants are needed to model power law creep (high temperature, low stress) and exponential creep (low temperature, high stress) for the same material. The Bammann inelasticity internal state variable (BIISV) model is a unified creep-plasticity model that can accurately model the power law creep, exponential creep, and plasticity regimes for a polycrystalline material. One other important distinction between the BIISV model and the power law approach is that the power law approach is purely empirical/ phenomenological while the BIISV is physically motivated from dislocation mechanics.

To begin, we outline the basics of internal state variable theory and describe the specific features of the BIISV. In the first section we review the fundamentals of kinematics of large deformations. In the next section, we discuss continuum field theory. The following section details the constitutive equations where we offer a brief summary of different modeling frameworks. We then present the BIISV theory (Bammann et al. 1988, 1990, 1993, 1996). We then describe a set of experiments to determine uniquely all the required material constants. Because such experiments have not yet been performed, we provide a non-unique set of material constants from existing olivine, lherzolite, marble, and rock salt experimental data.

Our longer range objective is to produce a robust internal state variable model that can capture the following attributes for a variety of mantle rocks: (1) temperature dependence, (2) strain rate dependence, (3) isotropic and anisotropic hardening and recovery from thermal and athermal dislocation interactions, (4) damage, (5) recrystallization effects, and (6) texture. The BIISV model currently treats items (1)-(3). It has been only used for metals, so this is the first effort to address geomaterials based on the paradigm of Ashby (1970) and Frost and Ashby (1982), who showed for crystalline materials, whether metals or rocks, that the same deformation mechanisms will occur. Chapter 4 will outline how to extend the BIISV approach to items (4)-(6) for silicates. Once a constitutive model incorporates such attributes, it can then be implemented into a continuum code to accurately capture material geometries and loading paths experienced in geological settings like TERRA (Baumgardner, 1985; Bunge et al., 1996).

Model Description

*Kinematic*s

From continuum theory, the motion of a body can be described in indicial notation by

$$x_i = \hat{x}\left(\underline{X}, t\right) \tag{2.1}$$

where x_i are the Cartesian coordinates (sometimes referred to as spatial or Eulerian coordinates), X are the material coordinates (sometimes referred to as Lagrangian coordinates), and t is time. The particle velocity and acceleration are given as the time

derivatives $\dot{x}_i = \partial \hat{x}_i \left(\underline{X}, t \right) / \partial t$ and $\ddot{x}_i = \partial^2 \hat{x}_i \left(\underline{X}, t \right) / \partial t^2$, respectively. The deformation gradient, $\underline{F}$, can then be expressed in indicial form as

$$F_{iJ} = x_{i,J} = \partial \hat{x}_i \left(\underline{X}, t \right) / \partial X_J . \tag{2.2}$$

As shown in Figure 2.1, the deformation gradient maps an infinitesimal line segment from the reference (Lagrangian) configuration to the current (Eulerian) configuration or State 0 to State 2, respectively.

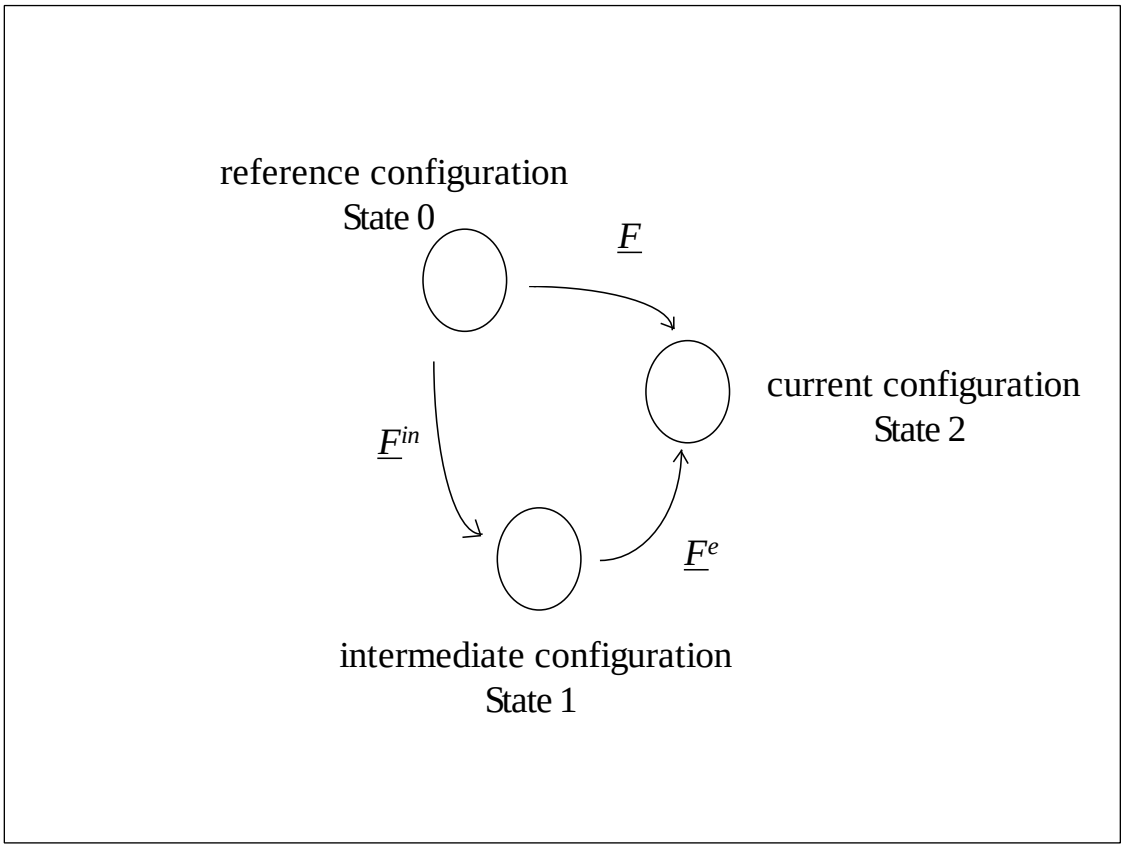

Figure 2.1 Illustration of multiplicative decomposition of the deformation gradient into elastic and inelastic parts.

The formulation of the kinematics development follows closely that of Lee and Liu (1967). The kinematics of motion include elastic straining and inelastic flow as is

illustrated by the multiplicative decomposition of the deformation gradient shown in Figure 2.1. The deformation gradient, $\underline{F}$, is decomposed into the deviatoric inelastic, or plastic, $\underline{F}^{in}$, and elastic parts, $\underline{F}^{e}$, given by

$$\underline{F} = \underline{F}^{e}\underline{F}^{in}. \tag{2.3}$$

The deviatoric inelastic deformation gradient maps the deformation from State 0 to State 1. The elastic deformation gradient maps the deformation from State 1 to State 2.

We note that the term inelasticity is used, because it accounts for strains due to plasticity and creep (or stress relaxation) mechanisms, which can be important in silicates. At the microscale, inelastic deformation can develop from dislocation glide, dislocation climb, diffusive flow of atoms, grain boundary sliding, mechanical twinning, and lattice collapse.

Equation (2.3) assumes that the motion of the body is described by a smooth displacement function. This precludes the initiation of discrete failure surfaces but still allows a continuum description of damage (Bammann and Aifantis, 1989; Horstemeyer et al., 2000), but damage and fracture are not included in this writing. The elastic deformation gradient, $\underline{F}^{e}$, represents lattice displacements from equilibrium. The inelastic deformation gradient, $\underline{F}^{in}$, represents a continuous distribution of dislocations and defects whose volume preserving motion produces permanent shape changes. This can arise from creep at low strain rates or from plasticity at higher strain rates. Although dislocations are by nature discontinuities, a continuum representation is possible to simulate their effects (Kroner, 1964 and Bilby et al., 1955).

The velocity gradient associated with the deformation gradient, $L = \dot{F}F^{-1}$, from Equation (2.2) can be decomposed into

$$L = \underline{L}^{e} + \underline{L}^{in} \tag{2.4}$$

where $\underline{D} = \frac{1}{2}\left(\underline{L} + \underline{L}^{T}\right)$ is the symmetric part and $\underline{W} = \frac{1}{2}\left(\underline{L} - \underline{L}^{T}\right)$ is the antisymmetric part of the velocity gradient tensor with analogous formulas holding for the elastic and inelastic components of the velocity gradients. The elastic rate of deformation relates to the total volumetric rate of deformation by the additive decomposition of the deformation rates similar to Equation (2.4),

$$\underline{D}^{e} = \underline{D} - \underline{D}^{in}. \tag{2.5}$$

Hence, the elastic velocity gradient can be determined from the velocity gradient.

Continuum Balance Equations

In describing the material response of polycrystalline solids, one must consider the following variables related to the continuum field equations: the Cauchy stress tensor, σ, the extrinsic body force per unit mass b, the internal energy per unit mass U, the extrinsic heat supply per unit mass and time Z, the entropy per unit mass η, the absolute temperature T, the density ρ, and the heat flux q. The balance laws can be written as differential equations relating these various variables. The balance of linear momentum is given as

$$\underline{\nabla} \cdot \underline{\sigma} + \rho \underline{b} = \rho \underline{\ddot{x}}. \tag{2.6}$$

The balance of angular momentum is represented by the symmetry of the Cauchy stress tensor,

($\sigma_{ij} = \sigma_{ji}$). The balance of energy is given by

$$\rho Z + \underline{\sigma} : \underline{\nabla} \dot{\underline{x}} - \underline{\nabla} \cdot \underline{q} = \rho \dot{U} . \tag{2.7}$$

In addition, these equations require that the entropy production inequality be satisfied. This is given by

$$\rho \dot{\eta} - \left(\frac{\rho Q}{T} \right) + \underline{\nabla} \cdot \left(\frac{\underline{q}}{T} \right) \geq 0 . \tag{2.8}$$

The Helmholtz free energy per unit mass is often introduced, $\psi = U - \eta T$, to rewrite the entropy inequality as

$$-\rho \left(\dot{\psi} + \eta \dot{T} \right) + \underline{\sigma} : \underline{\nabla} \dot{\underline{x}} - \left(\frac{1}{T} \right) \underline{q} \cdot \underline{\nabla} T \geq 0 . \tag{2.9}$$

Equation (2.9) in which $\underline{x} = \hat{\underline{x}} \left(\underline{E}^e, \underline{E}^{in} \right)$ suggests that the set $\left\{ \underline{E}^e, \underline{E}^{in}, T, \nabla_i T \right\}$ should be the set of independent state variables, where $\underline{E}^e$ and $\underline{E}^{in}$ are elastic strain and inelastic strain, respectively. However, physical evidence dictates that inelastic strain $\underline{E}^{in}$ (and inelastic strain rate, or creep rate, $\underline{D}^{in}$) is/are not admissible as independent state variables because of history effects and the inelastic strain does not affect the Helmholtz free energy (Onat and Fardshisheh, 1972). Hence, a set of internal state variables, $\underline{V}_i$, are necessary to complete the set of independent variables, which leads to the formulation of internal state variable theory.

One last comment is needed before we discuss the constitutive equations. We focus on the constitutive model formulation in this paper and allow the finite element or finite volume method to account for the continuum balance equations.

Constitutive Equations

Because the most commonly used constitutive equation for mantle materials has been power law creep with temperature dependence, it is worthwhile discussing the difference between the power law equation and ISV equations. The power law material constants are generally determined by creep tests and describe microstructural behavior in a somewhat heuristic manner. Although not usually shown in tensorial form, we express the power law creep rate as a second rank tensor for consistency with the kinematic development,

$$\underline{D}^{in} = A\sigma^{n} \exp\left(\frac{-Q}{RT}\right)\underline{e}, \tag{2.10}$$

where A is the power law coefficient, n is the power law exponent, σ is the second deviatoric invariant of stress, $\underline{e}$ is the unit stress direction tensor , Q is the activation energy, R is the gas constant, T is temperature, and $\underline{D}^{in}$ is the inelastic rate of deformation (creep rate). Garofalo (1963) developed a form of the inelastic rate of deformation to capture a broader range of inelastic behavior (power law and power law breakdown regimes) by using a hyperbolic sine,

$$\underline{D}^{in} = A\sinh\left(\frac{\sigma}{B}\right)\exp\left(\frac{-Q}{RT}\right)\underline{e}, \tag{2.11}$$

where B is a drag stress constant. For the exponential creep regime others (Tsenn and Carter, 1987; Kohlstedt and Goetze, 1974) have proposed for the high stress, low temperature applications

$$\underline{D}^{in} = A\sigma^{2} \exp\left(\frac{-Q(\sigma)}{RT}\right)\underline{e}, \tag{2.12}$$

where Q is a function of the stress.

The power law, Garofalo, and exponential creep models inherently assume an isotropic material response. Therefore, no texture or kinematic (anisotropic) hardening arising from directional dislocation substructures is considered, although anisotropy is clearly apparent in mantle rocks under finite deformations at small and large size scales (Kirby and Kronenberg, 1987; Egydio-Silva and Mainprice, 1999). Another shortcoming of previous models is that they include no elasticity. Fundamentally, elastic-plastic couplings can dictate the mechanical stress state and are important especially when nonmonotonic loading sequences arise. Covey-Crump (1994) insightfully argues that the physical interpretation of the material constants for the power law and Garofalo equations is lacking and therefore can lead to unreliable extrapolations outside of those cases tested. Finally and most importantly, these models do not include history effects from temperature, pressure, or deformation, even though mechanical properties of all real materials are functions of their history.

Internal State Variable Formulation

Thermodynamically-based constitutive equations that are used to capture history effects are generally cast into two classes. In the first class using hereditary integrals, the present state of the material is described by the present values and past history of observable variables. The second class is based on the concept that the present state of the material depends only on the present values of observable variables and a set of internal state variables (ISVs). The second approach is more appropriate to solve a wide range of boundary value problems, and it is this form that we discuss in this paper.

The notion of internal state was introduced into thermodynamics by Onsager (1931) and was applied to continuum mechanics by Eckart (1940, 1948). The ISV formulation is a means to capture the effects of a representative volume element and not all of the complex phenomena at the local level; hence, an ISV will macroscopically average in some fashion the details of the microscopic arrangement. In essence, the complete microstructure arrangement is unnecessary as long as the macroscale ISV representation is complete (Kroner, 1964). As a result, the ISV must be based on physically observed behavior and constrained by the laws of thermodynamics (Coleman and Gurtin, 1967). From the viewpoint of rational thermodynamics, the ISVs provide the additional information necessary for a rational description of the thermodynamic state of the material. From the viewpoint of thermodynamics of irreversible processes (Rice, 1971), the ISVs provide the information required to describe neighboring constrained equilibrium states.

To describe our ISV formulation we first decompose the Helmholtz free energy ψ into the free energy associated with thermoelastic strain, ψ^e, and the free energy associated with inelasticity, ψ^e, according to

$$\psi = \psi^e\left(\underline{E}^e, T, \underline{V}_1, \underline{V}_2, ...\underline{V}_n\right) + \psi^{in}\left(T, \underline{V}_1, \underline{V}_2, ...\underline{V}_n\right), \tag{2.13}$$

where the thermoelastic Green strain $\underline{E}^e$ and the absolute temperature, T, are termed observable state variables. The $\underline{V}_i$ are the internal state variables representing the effects of microstructural rearrangement at lower length scales. The n is the total number of ISVs. The ISVs are sometimes referred to as generalized displacements. Each of the ISVs can be represented by any order of tensor. Consequently, its thermodynamic

conjugate must be the identical order. By defining the Helmholtz free energy in this manner, thermodynamic conjugate forces arise (Chaboche, 1972; Germain et al., 1983; and Krajcinovic, 1983) with respect to their generalized displacements in the BIISV model as

$$\underline{\hat{\sigma}} = \rho \frac{\partial \psi}{\partial \underline{E}}, \ \eta = -\rho \frac{\partial \psi}{\partial T}, \ \underline{b} = -\rho \frac{\partial \psi}{\partial \underline{\alpha}}, \ \kappa = -\frac{\partial \psi}{\partial R}, \frac{\partial \psi}{\partial \underline{\nabla} T} = 0 \tag{2.14}$$

where $\underline{\hat{\sigma}}$ is the second Piola-Kirchhoff stress defined with respect to the stress-free configuration, η is the specific entropy, $\underline{b}$ is the backstress tensor corresponding to kinematic hardening $\underline{\alpha}$, κ is the scalar isotropic stress corresponding to isotropic hardening R. The density ρ corresponds to the stress-free configuration in which these relations are written. For clarity, we might add that the relationship between the thermodynamic driving force and generalized displacement is analogous to the well-known Newtonian force and displacement relationship characteristic of mechanical systems.

The rate equations are generally written as objective rates ($\overset{\circ}{\underline{\sigma}}, \overset{\circ}{\underline{\alpha}}$) with indifference to the continuum frame of reference assuming a Jaumann rate in which the continuum spin is assumed to equal the elastic spin ($\underline{W} = \underline{W}^e$). The ISVs are functions of the observable variables (temperature, stress state, and rate of deformation). In general, the rate equations of generalized displacements, or thermodynamics fluxes, describing the rate of change may be written as independent equations for each ISV or as derivatives of a suitably chosen potential function arising from the hypothesis of generalized normality (Rice, 1971). An advantage of assuming generalized normality, although somewhat

restrictive, is unconditional satisfaction of the Kelvin inequality of the second law of thermodynamics (nonnegative intrinsic dissipation), i.e.,

$$\underline{\sigma} : \underline{D}^{in} - \underline{b} : \overset{\circ}{\underline{\alpha}} - \kappa \cdot \dot{R} \geq 0 . \tag{2.15}$$

Although generalized normality is not an appropriate assumption for surface rocks, it is appropriate for mantle rocks since dilatational effects on nonnormality assumptions are negligible because of high confining pressures. The laboratory experimental data examined within this paper considers only the deviatoric response of a material. Clearly, compressibility effects arise in the presence of extreme pressures, and the constitutive framework described in this paper can capture some of these effects; however, further research is needed to evaluate the pressure dependence on the inelastic flow stress.

The selection of the ISVs may, in principle, be somewhat arbitrary, but the kinematic hardening and isotropic hardening are physically motivated and strongly influence the history of the material model. The BIISV model accounts for deviatoric inelastic deformation resulting from the presence of dislocations in crystallographic material.

The following set of equations can be used within finite volume or finite element codes. We express each set of equations in terms of the observable state variables and internal state variables. The pertinent observable state variables are the following,

$$\overset{\circ}{\underline{\sigma}} = \dot{\underline{\sigma}} - \underline{W}^e \underline{\sigma} + \underline{W}^e \underline{\sigma} = \lambda tr\left(\underline{D}^e\right)\underline{I} + 2\mu \underline{D}^e \tag{2.16}$$

$$\underline{D}^e = \underline{D} - \underline{D}^{in} \tag{2.17}$$

$$\underline{D}^{in} = f(T)\sinh\left[\frac{\left\|\underline{\sigma}' - \underline{\alpha}\right\| - R - Y(T)}{V(T)}\right]\frac{\underline{\sigma}' - \underline{\alpha}}{\left\|\underline{\sigma}' - \underline{\alpha}\right\|} \tag{2.18}$$

where the elastic Lame constants are denoted by λ and μ. We express the deviatoric stress $\underline{\sigma}'$ in indicial notation as

$$\sigma_{ij}' = \sigma_{ij} - \frac{1}{3}\sigma_{kk}\,. \tag{2.19}$$

The elastic rate of deformation $\underline{D}^{e}$ results when the total deformation $\underline{D}$, which is determined from the boundary conditions, is subtracted from the flow rule as shown in Equation (2.17).

The independent variables for the inelastic rate of deformation are given in Equation (2.18) as the stress, temperature, and internal state variables. Equation (2.18) is similar to power law and Garofalo equations for creep except that the ISVs are now included. The deviatoric inelastic flow rule $\underline{D}^{in}$ is in a unified creep-plasticity form. The flow rule is a function of the temperature, the kinematic hardening internal state variable $\underline{\alpha}$, the isotropic hardening internal state variable R, and the functions $f(T)$, $V(T)$, and $Y(T)$, which are related to yielding with Arrhenius-type temperature dependence. The function $Y(T)$ is the rate-independent yield stress. The function $f(T)$ determines when the rate-dependence affects initial yielding. The function $V(T)$ determines the magnitude of rate-dependence on yielding. These functions are determined from simple isothermal compression tests with different strain rates and temperatures,

$$V(T)=C_1\exp\left(\frac{-C_2}{T}\right),\ Y(T)=\frac{1}{2}C_3\exp\left(\frac{C_4}{T}\right)\left(1+\tanh\left[C_{19}\left\{C_{20}-T\right\}\right]\right),$$

$$f(T)=C_5\exp\left(\frac{-C_6}{T}\right). \tag{2.20}$$

Hardening-Recovery ISV Equations

The hardening-recovery equations (Armstrong and Frederick, 1966) can be thought of as the responses from thermodynamic forces arising from kinematic constraints of dislocation nucleation, motion, and trapping. As such, kinematic and isotropic hardening equations are introduced in the BIISV model and have shown to cover a broad range of crystallographic materials in terms of hardening and recovery related to dislocation glide and climb. The kinematic hardening internal state variable $\underline{\alpha}$ reflects the effect of dislocation populations that induce anisotropic work hardening, and the isotropic hardening internal state variable R reflects the effect of the mean global dislocation density. Note that the inelastic rate of deformation $\underline{D}^{in}$ in Equation (2.20) is directly influenced by these dislocation ISV equations. Because $\underline{D}^{in}$ has an anisotropic component and an isotropic component, various deformation path histories can be captured such as the Bauschinger effect. As such, the hardening equations (2.21)-(2.22) are cast in a hardening-recovery format that includes dynamic and static recovery,

$$\underline{\dot{\alpha}}=h(T)\underline{D}^{in}-\left[\sqrt{\frac{2}{3}}r_d(T)\left\|\underline{D}^{in}\right\|+r_s(T)\right]\|\underline{\alpha}\|\underline{\alpha} \tag{2.21}$$

$$\dot{R}=\sqrt{\frac{2}{3}}H(T)\left\|\underline{D}^{in}\right\|-\left[\sqrt{\frac{2}{3}}R_d(T)\left\|\underline{D}^{in}\right\|+R_s(T)\right]R^2 \tag{2.22}$$

The functions $r_s(T)$ and $R_s(T)$ are scalar in nature and describe the diffusion-controlled static or thermal recovery, while $r_d(T)$ and $R_d(T)$ are scalar functions describing dynamic recovery. Hence, the two main types of recovery that are exhibited by populations of dislocations within rocks (Kirby, 1983) are captured in the ISVs. The anisotropic hardening modulus is $h(T)$, and the isotropic hardening modulus is $H(T)$. The BIISV parameters are given by

$$r_d(T) = C_7 \exp\left(\frac{-C_8}{T}\right) \tag{2.23}$$

$$h(T) = C_9 - C_{10}T \tag{2.24}$$

$$r_s(T) = C_{11} \exp\left(\frac{-C_{12}}{T}\right) \tag{2.25}$$

$$R_d(T) = C_{13} \exp\left(\frac{-C_{14}}{T}\right) \tag{2.26}$$

$$H(T) = C_{15} - C_{16}T \tag{2.27}$$

$$R_s(T) = C_{17} \exp\left(\frac{-C_{18}}{T}\right). \tag{2.28}$$

Experiments

Experiments can be performed to uniquely determine the parameters for the BIISV model. To separate the kinematic and isotropic variables, nonmonotonic testing is required to extract history effects from the evolving microstructure. Furthermore, nonmonotonic and jump temperature and strain rate tests are needed to separate the effects of dynamic (strain-induced) and static (time-induced) recovery as functions of

temperature. Microstructural features such as grain size, amount of water, amount of porosity/microcracking, chemistry, texture, and melt fraction must be quantified on virgin polycrystalline material.

To determine the temperature and strain rate dependent functions for yield, Equation (2.20), the material should be tested at least for three different temperatures and three different strain rates under uniaxial compression. Hence, nine tests are desired. This would determine constants C_1-C_6 and C_{19}-C_{20}. If finite deformations are achieved, these nine tests can be used to determine the overall hardening and recovery constants at different strain rates and temperatures. In the absence of nonmonotonic test data, one would have to assume no kinematic hardening and hence constants C_7-C_{12} would be zero unless the Bauschinger effect was known by some other means. With no kinematic hardening assumed, the isotropic hardening moduli and dynamic recovery constants (C_{13}-C_{16}) can be determined. If monotonic and nonmonotonic tests are conducted, then C_7-C_{10} (kinematic hardening) and C_{13}-C_{16} (isotropic hardening) can be uniquely quantified.

To determine the static recovery constants for the kinematic, C_{10}-C_{12}, and isotropic, C_{17}-C_{18}, variables, either creep or stress relaxation tests must be conducted under both monotonic and nonmonotonic loading conditions for three different temperatures and three different creep rates.

Validation of the model constants can be performed by conducting jump-type tests. Once the model constants have been determined, then the model should be able to predict complex history tests, such as jump rate tests or jump temperature tests that include variations of stress states and stress state sequences.

Results

Because the test data described above are all not currently available to uniquely determine the BIISV model constants, non-unique constants will be determined using literature data for wet and dry polycrystalline olivine, polycrystalline lherzolite, polycrystalline Carrara Marble, and rock salt. The temperature dependent elastic moduli that were used in determining the model constants were obtained from the Simmons and Wang (1971).

For the olivine, the range of temperatures analyzed ranged from 1273K<T<1573K for wet and dry Anita Bay Dunite (Chopra and Paterson, 1981,1984). Creep data from the Chopra and Paterson (1981, 1984) to 3000K were used to determine the static recovery constants. Finally, strain rate jump tests from Chopra and Paterson (1984) and Karato et al. (1986) for wet and dry conditions were then used to validate the resulting model constants.

Experimental data for high confining pressure tests for initially isotropic wet and dry polycrystalline olivine were used to determine the BIISV model constants. The temperature dependent elastic moduli are from Simmons and Wang (1971). Below about 400 km olivine changes to other crystallographic phases; our constants are appropriate only for olivine. Experimental stress-strain data for a range of temperatures from 1273K<T<1573K were analyzed to determine the yield functions, hardening moduli, and dynamic recovery functions for wet and dry Anita Bay and Aheim Bay Dunite (Chopra and Paterson, 1981, 1984) as shown in Figures 2.2 and 2.3. Dry Anita Bay and Aheim Bay Dunite give the same results, so Figure 2.3 shows the Aheim Bay experimental

curves. Creep data from Chopra and Paterson (1981, 1984) up to 1573K was used to determine the static recovery constants.

Figure 2.2 shows the comparison of the model results to the experimental data for wet monolithic polycrystalline dunite from Aheim Bay (900 μm grain size) and Anita Bay (100 μm grain size). Due to the lack of nonmonotonic test data for all materials considered in this study constants C_7-C_{12} are set to zero, which implies anisotropic hardening is not be included. Anisotropic hardening can be added, of course, when the appropriate experimental measurements are performed. The data that are available reveal strong temperature dependence. The experimental stress-strain data available in Chopra and Paterson (1981, 1984) does not show different strain rates so only the temperature dependence is considered for comparison purposes. Table 2.1 shows the proposed material constants for wet and dry olivine. Constants C_2, C_6, C_{12}, C_{18}, and C_{20} are assumed to be zero for this parameter determination.

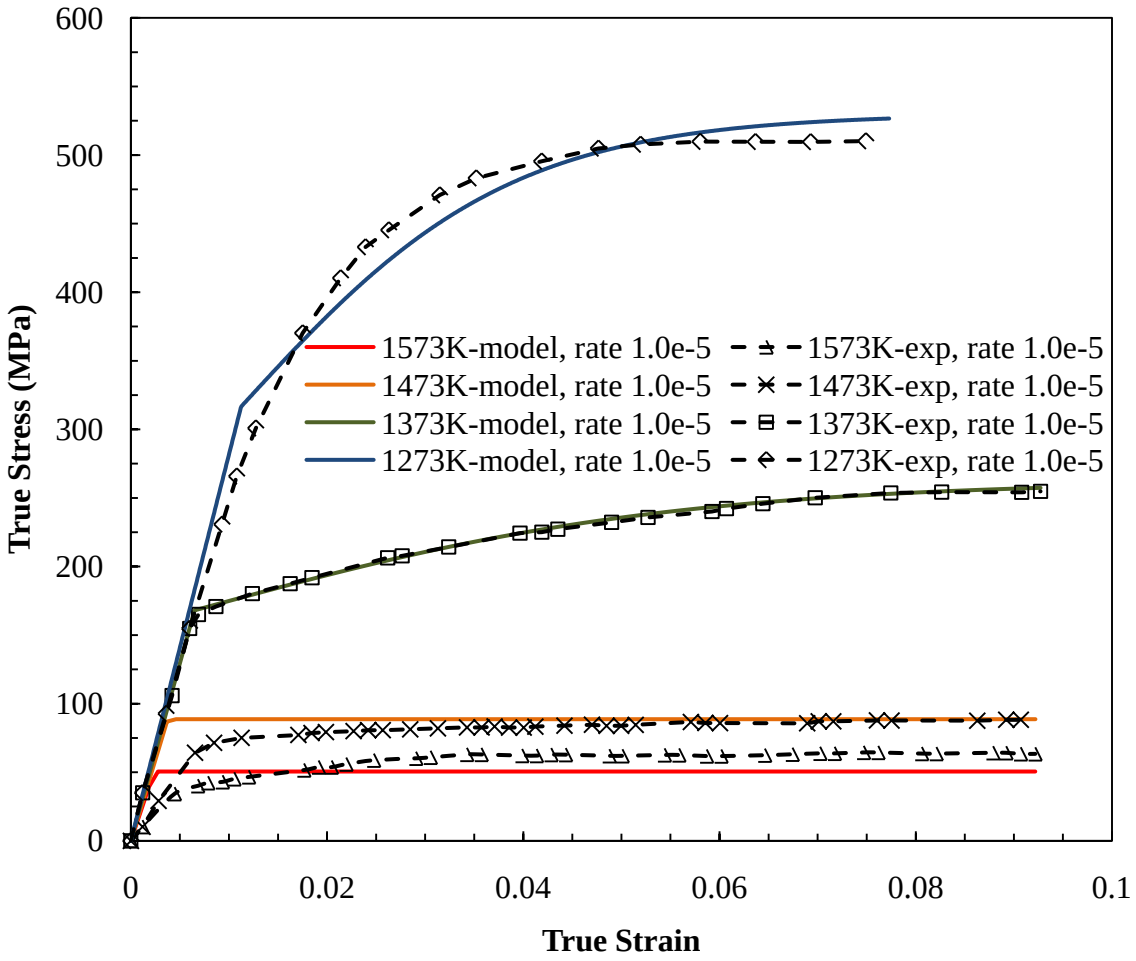

Figure 2.2 Comparison of model to experimental data for wet polycrystalline olivine.

Figure 2.3 shows the comparison of the model results to the experimental data for dry monolithic polycrystalline dunite. From the Chopra and Paterson (1981, 1984) data, two different temperatures and two different strain rates were used for the comparison. Chopra and Paterson (1981, 1984) noted that no grain size effect was evident in material without water, so the Aheim Bay and Anita Bay Dunite yielded essentially the same stress-strain behavior.

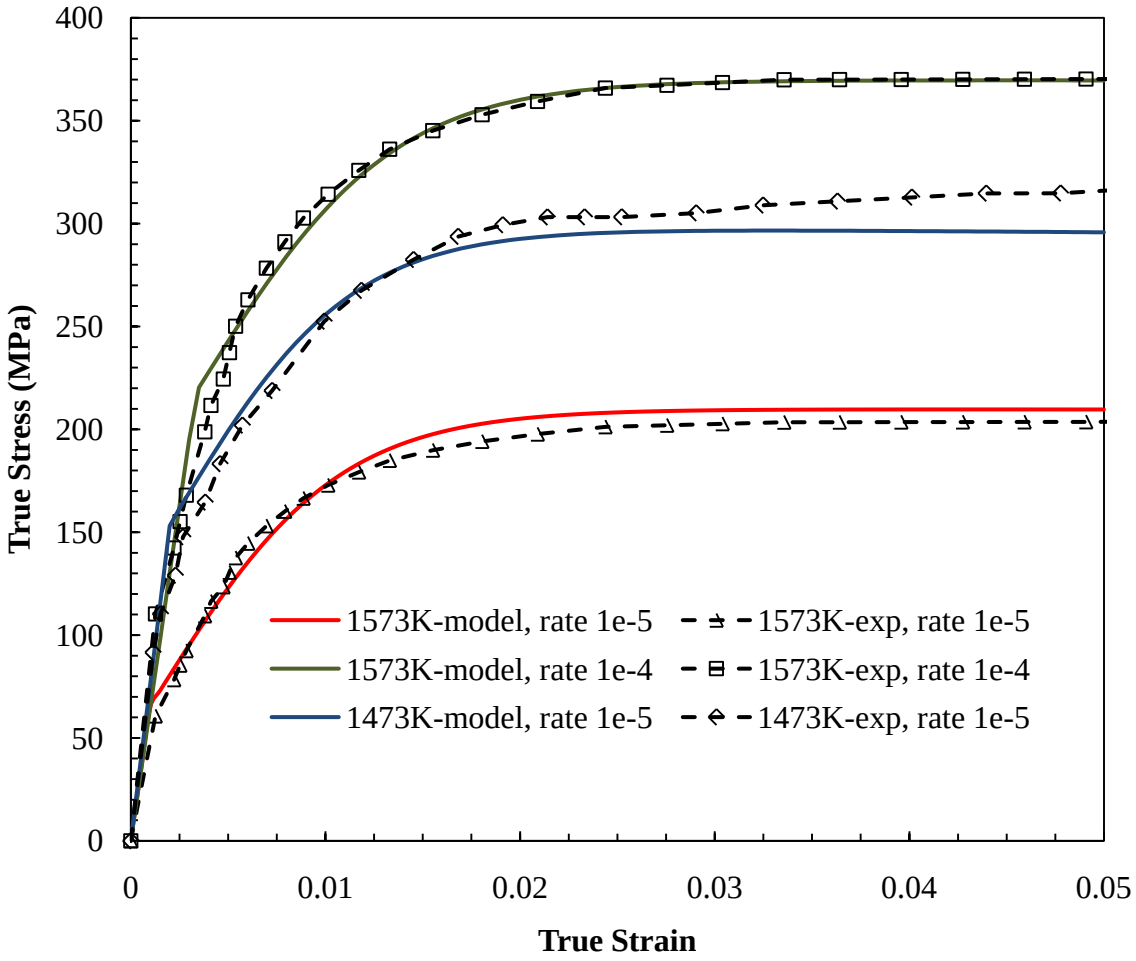

Figure 2.3 Comparison of model to experimental data for dry polycrystalline olivine.

Figure 2.4 shows a comparison of the ISV model to three different temperatures and three different strain rates for lherzolite data (Carter and Ave'Lallemant, 1970). Lherzolite is a fine-grained nearly equiaxed granular rock comprising 60%-70% olivine, 20%-30% enstatite, 5%-10% diopside, and less than 1% spinel. The temperatures ranged between 1123K and 1333K, and the strain rates ranged between 7.8e-6 s^{-1} and 7.8e-4 s^{-1}. Although the experimental data in Figure 2.4 goes from nearly perfect plasticity at the higher temperatures to almost bilinear hardening in the lower temperatures, note that the

model is robust enough to capture such behavior. Table 2.1 displays the constants used for lherzolite.

Table 2.1 BIISV material constants for wet and dry polycrystalline olivine aggregates, lherzolite, Carrara Marble, and rock salt. Constants C_6-C_{12} are omitted because they are zero.

Material Constants	Wet Olivine Aggregate	Dry Olivine Aggregate	Lherzolite	Carrera Marble	Rock Salt
C_1 (MPa)	2.20E+01	7.21E+01	1.00E-05	3.16E+00	1.56E+01
C_2 (K)	0.00E+00	0.00E+00	0.00E+00	0.00E+00	0.00E+00
C_3 (MPa)	2.00E+02	5.00E+01	1.00E-05	1.53E+02	1.21E+00
C_4 (K)	1.97E+03	1.00E+03	0.00E+00	0.00E+00	0.00E+00
C_5 (1/s)	1.00E-05	1.00E-05	1.00E-05	1.00E-05	1.00E-05
C_{13} (1/MPa)	0.00E+00	8.33E-01	0.00E+00	5.25E-02	1.29E+02
C_{14} (K)	0.00E+00	0.00E+00	0.00E+00	3.23E+02	8.73E+02
C_{15} (MPa)	1.20E+05	1.94E+04	1.03E+05	4.10E+03	5.42E+03
C_{16} (K)	8.69E+01	0.00E+00	6.58E+01	3.84E+00	1.04E+01
C_{17} (s/MPa)	2.36E-06	1.00E-06	4.15E+00	1.84E-04	0.00E+00
C_{18} (K)	0.00E+00	0.00E+00	1.63E+04	5.87E+03	0.00E+00
C_{19} (1/K)	3.83E-03	3.86E-02	0.00E+00	0.00E+00	0.00E+00
C_{20} (K)	1.17E+03	1.51E+03	0.00E+00	0.00E+00	0.00E+00

Figure 2.5 shows a comparison of the ISV model to three different temperatures and two different strain rates for Carrara Marble (Covey-Crump, 1994). Again, the BIISV model captures the stress-strain behavior fairly well for these ranges of temperatures and strain rates. The constants for Carrara Marble are listed in Table 2.1.

Figure 2.6 shows the correlation of the model results to the experimental data for rock salt(Aubertin et. al, 1991). Rock salt (halite) was included among the materials we considered to show that even non-silicate geomaterials can be treated successfully using the BIISV model. Only two strain rates and temperatures were included in the

comparison, and clearly more data would be desirable to capture a larger range temperatures and strain rates. The constants for rock salt are listed in Table 2.1.

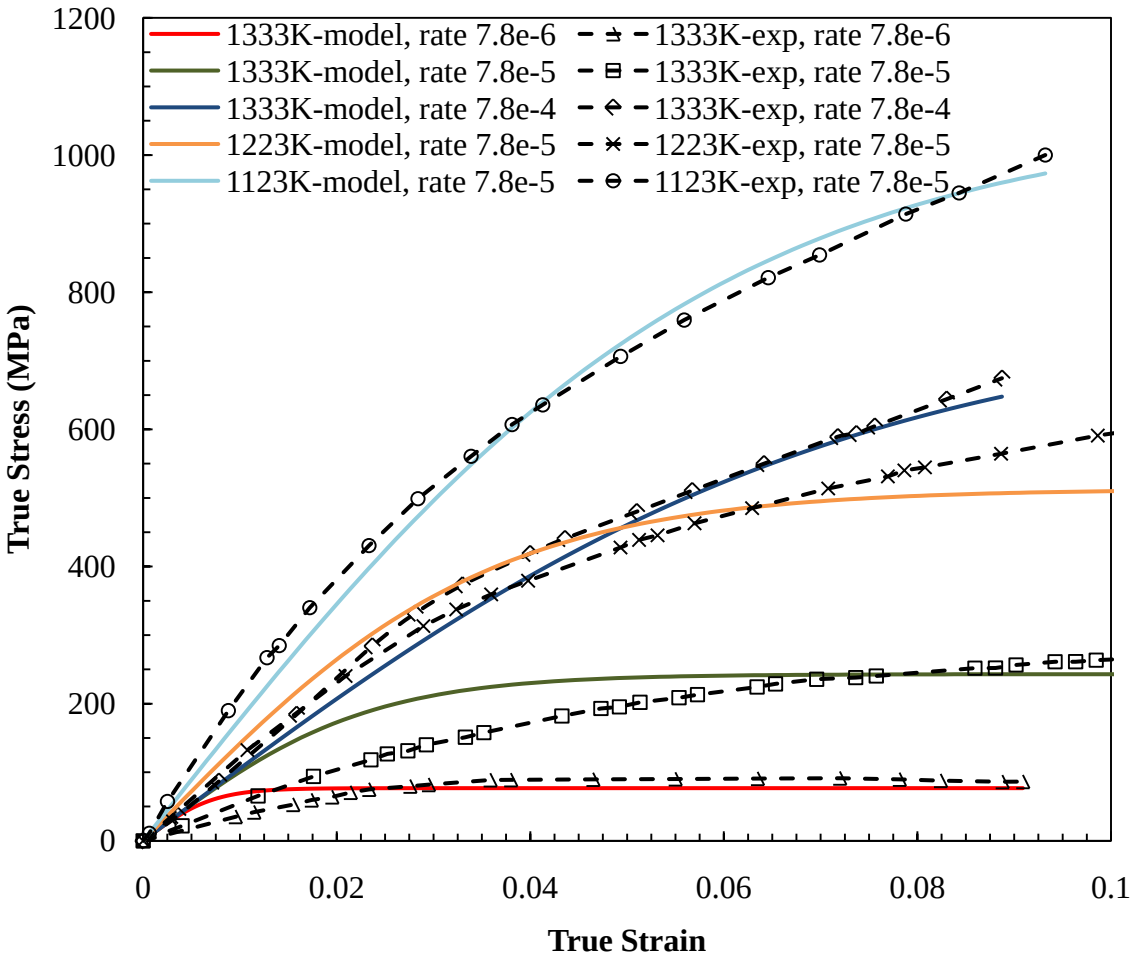

Figure 2.4 Comparison of model results to experimental data for lherzolite.

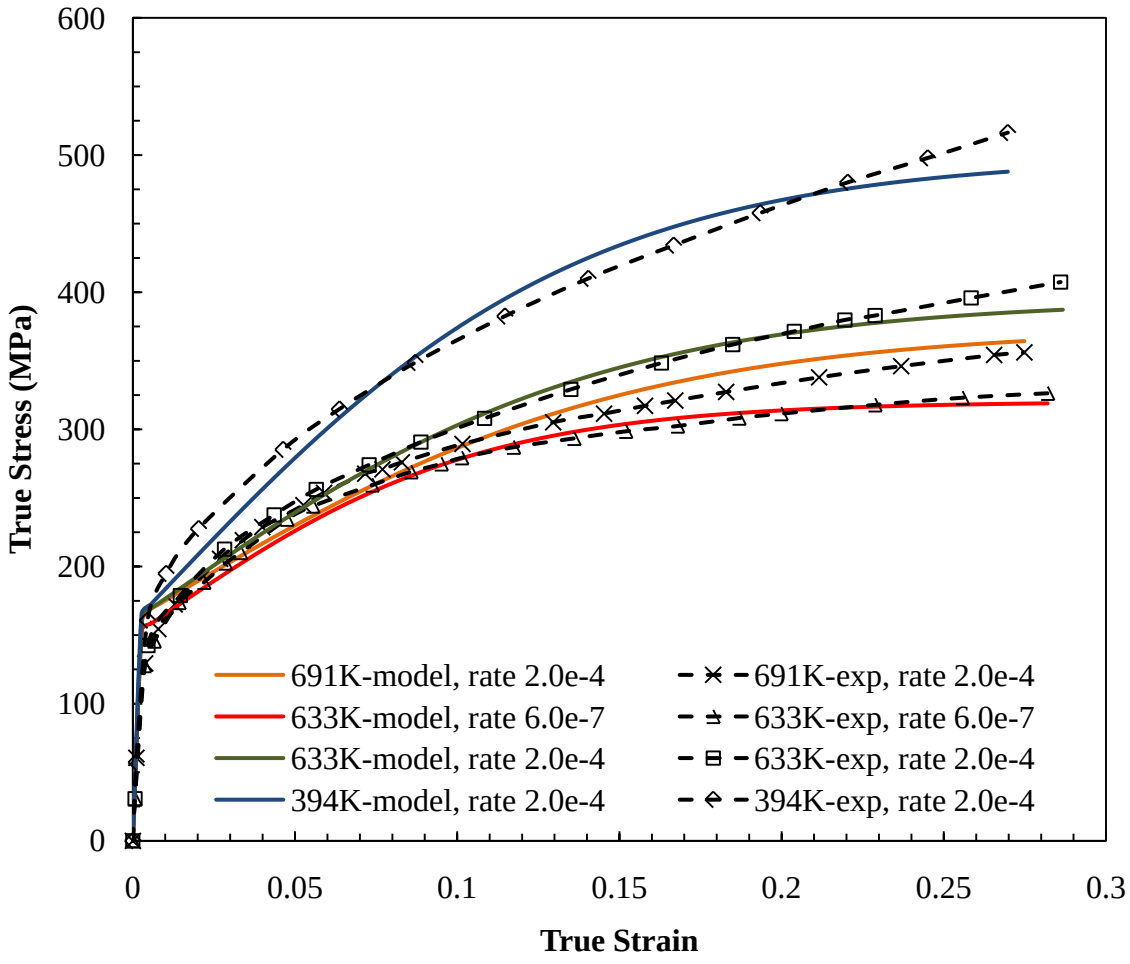

Figure 2.5 Comparison of model results to experimental data for Carrara Marble for varying temperatures and strain rate.

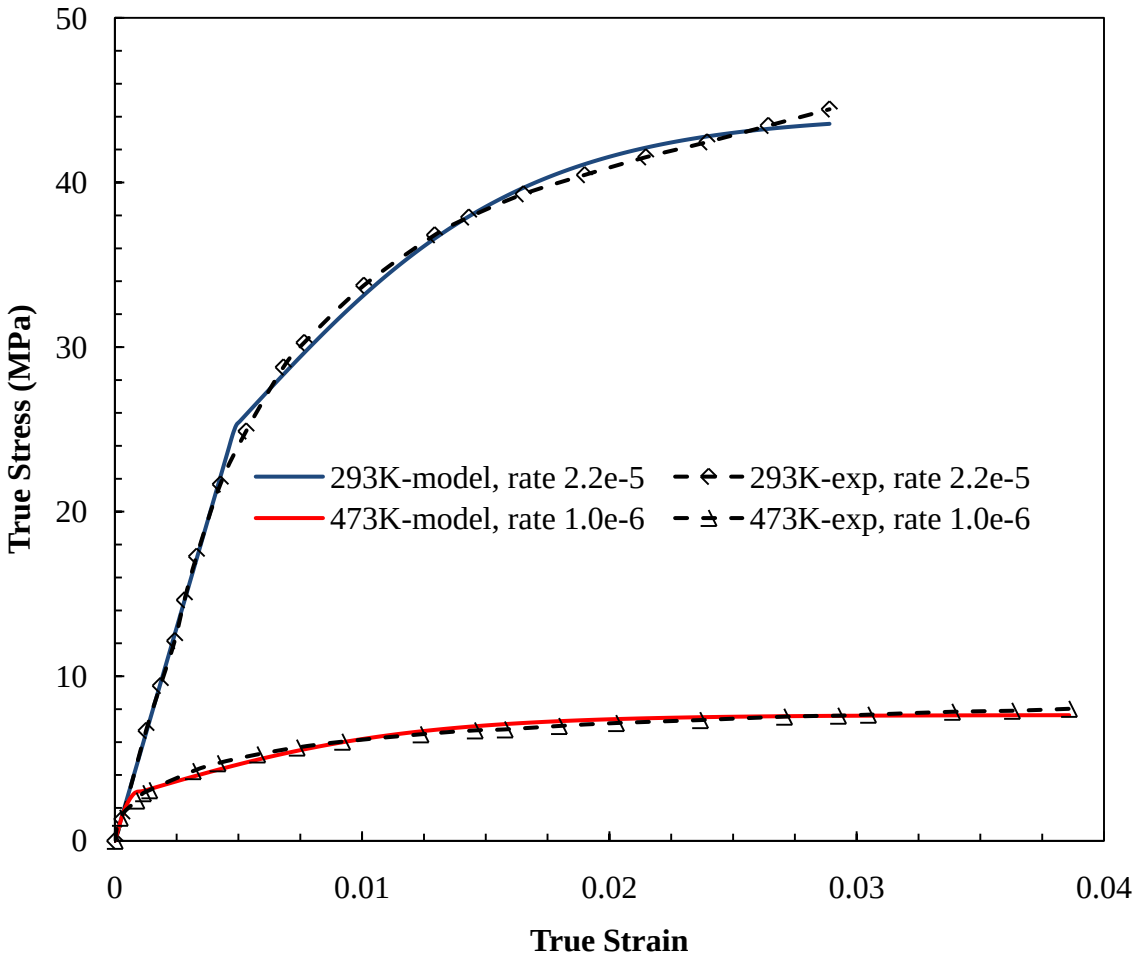

Figure 2.6 Comparison of model results to experimental data for rock salt.

Discussion

The previous section documents the BIISV model's ability to reproduce the experimental stress strain data for high temperature geomaterials. One way to validate the constants determined in the previous section is to run experimental jump-type tests and compare the model with the experiment. The jump tests give a better indication of the models ability to capture the material's response, because the constants are not determined from them. The power law model will also be plotted with the experimental

data and BIISV model. Both strain rate and temperature jump tests can be performed for comparison.

For the dry dunite, strain rate jump tests were included in the experiments performed by Chopra and Paterson (1984). Figure 2.7 shows a direct comparison of the BIISV Model and the power law model with the Chopra and Paterson (1984) experiments. Chopra and Paterson (1984) determined the power law parameters, A, Q, and n, based on their experiments for dry olivine, which are shown in Table 2.2. The power law model does not consider the elastic portion of the stress-strain curve, so the stress is constant for each of the given strain rates. A given strain rate simply yields the unique steady state stress. The non-steady state or transient portion of the stress-strain behavior is completely neglected. With good constants the power law model can represent the steady state portion of the stress-strain curve for various strain rates and temperatures. Figure 2.7 shows that the constants for dry olivine do an adequate job of capturing the steady state stresses for the given strain rates. However, the BIISV model constants for dry olivine do a better job of capturing the steady state stress while accurately modeling the transient portion of the stress-strain behavior.

Table 2.2 Power law hardening parameters for dry olivine and lherzolite.

Material Constants	**Dry Olivine**	**Lherzolite**
A (s^{-1} MPa^{-n})	22840	803.8
Q (kJ mol^{-1})	535	334.1
n	3.6	2.3

The BIISV model also has the added benefit of remembering its deformational history through its internal state variables. For dry olivine, only the isotropic hardening

state variable is being used as a history tracker. Physically speaking, isotropic hardening in the BIISV is used to represent statistically the number of stored dislocations that cause a yield surface to expand in a uniform manner. When the stress reaches steady state at a constant strain rate and temperature, the statistical production (hardening) and destruction (recovery) of stored dislocations balance out and the isotropic hardening variable achieves a steady state. The value of the isotropic hardening variable is remembered when the strain rate changes. For the case shown in Figure 2.7, the isotropic hardening variable eventually reaches a lower steady state value based on the lower strain rate, and the change in isotropic hardening decreases the stress.

Carter and Ave'Lallemant (1970) performed both strain rate and temperature jump tests that can also be used to validate the model. Figure 2.8 shows the comparison of the BIISV model and the power law model to a strain rate jump test from Carter and Ave'Lallemant (1970) at a constant temperature of 1333K. Lherzolite is a different test of a model's robustness, because much of the experimental data done by Carter and Ave'Lallemant (1970) does not reach steady state especially at lower temperatures, T < 1123K, and the higher tested strain rates, rate > 7.8e-5 s^{-1}. Carter and Ave'Lallemant (1970) use the steady state values of stress for the higher temperatures to determine power law constants over the range of strain rates. The power law constants for lherzolite are shown in Table 2.2. Applying the power law constants to the strain rate test shown in Figure 2.8 produces large overestimations of stress on all of the strain rates. The BI ISV model, however, does not have to assume steady state has occurred and as shown in Figure 2.8 the BIISV model is far superior in this case even with the non-unique constants discussed earlier. The BIISV model again captures the transient response of the

stress-strain behavior as well as carrying the history from one strain rate to another as displayed in Figure 2.8.

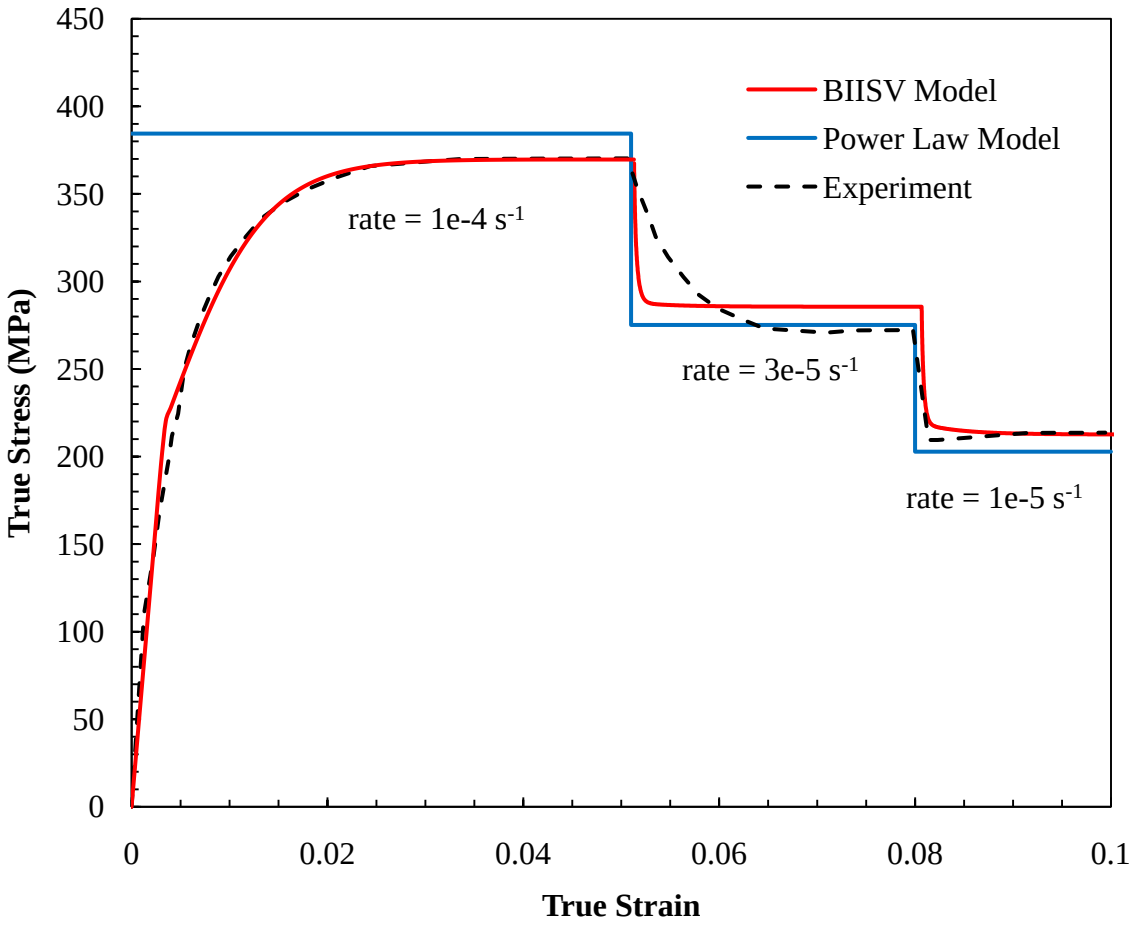

Figure 2.7 Comparison of BIISV model and power law model to experimental data for dry polycrystalline olivine for a varying strain rate history at 1573K.

Figure 2.9 compares the BIISV model and the power law model to the experimental temperature jump test by Carter and Ave'Lallemant (1970) at a constant strain rate of 7.8e-5 s^{-1}. The same power law constants for lherzolite are used as shown in Table 2.2. The strain rate used for the temperature jump test is right on the border line in terms of the usefulness of the power law constants. The lower temperatures, 1123K and

1223K, are extremely overestimated as shown in Figure 2.9. Because the values for the power law stresses are so high, 5.1 GPa and 1.43 GPa at 1123K and 1223K, respectively, that we do not show them in the plot because they are so far off the chart. The steady state values for stress are closer for the 1333K and 1443K case but still are overestimated. Again the BIISV model constants prove to be far superior for this temperature jump test.

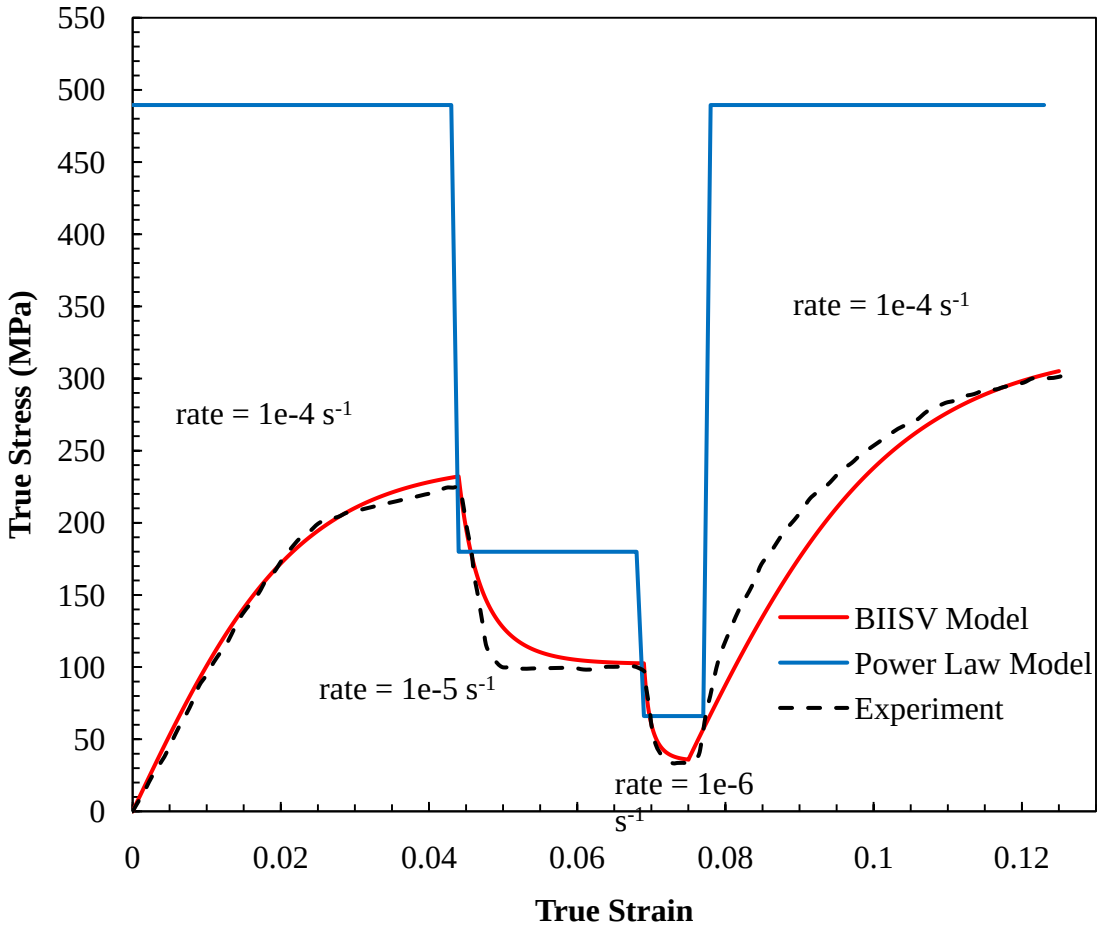

Figure 2.8 Comparison of BIISV model and power law model to the experimental data for lherzolite for a varying strain rate history at 1333K.

Figures 2.7 and 2.8 show that for the given temperatures and strain rates the BIISV model can accurately capture the transient effects that the power law could never

capture. The BIISV model even does a good job of extrapolating past the fitted range as shown by the 1443K temperature in Figure 2.9. The 1443K temperature stress-strain behavior was not originally fit as observed in Figure 2.4. Care must be taken to not use too much extrapolation beyond the experimental data, because different physical mechanisms could be involved, which the model may not capture with a given set of constants. The larger the range of temperatures and strain rates for which the BIISV model constants are fit, the greater is range over which the model can usefully be applied.

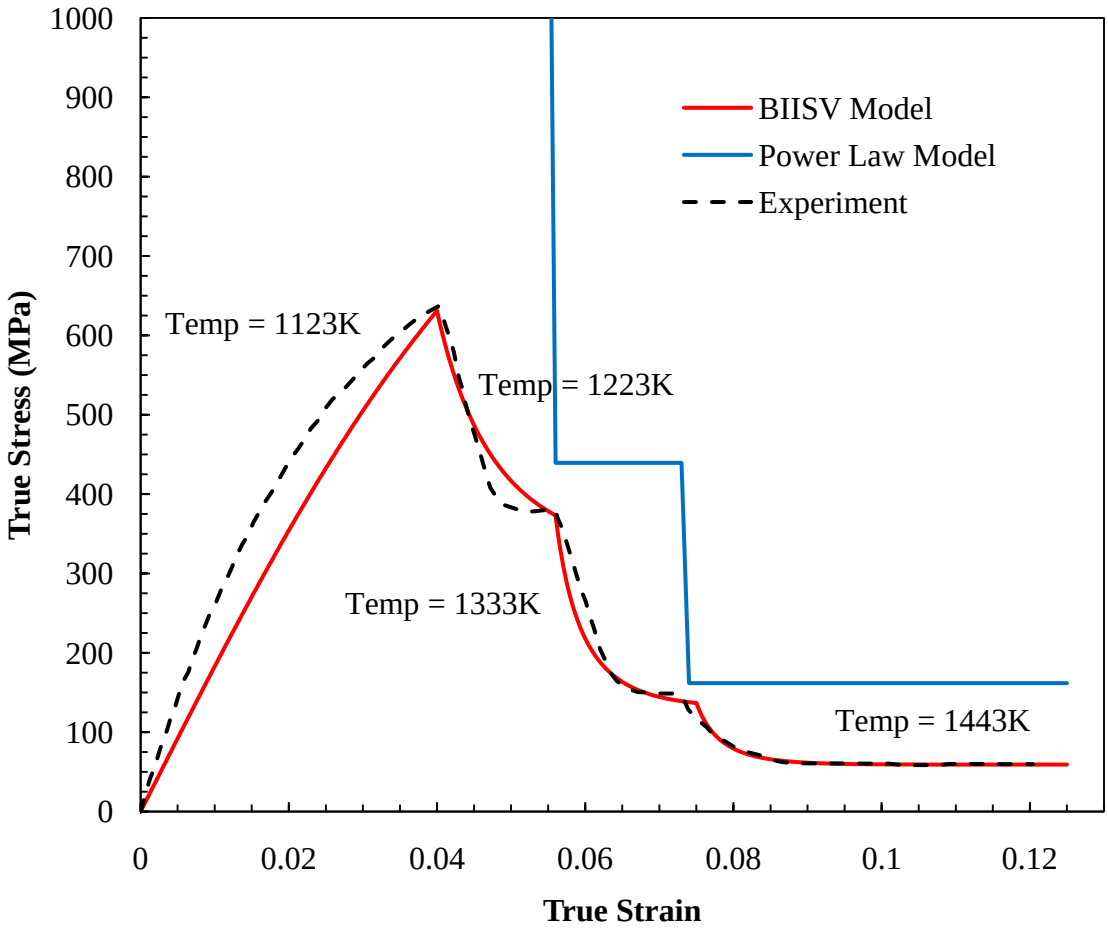

Figure 2.9 Comparison of BIISV model and power law model to experimental data for lherzolite for a varying temperature history at a constant strain rate of 7.8e-5 s^{-1}.

Conclusions

The BIISV elastic-viscoplastic model appears to offer important advantages for treating the time-dependent phenomenological behavior of upper mantle silicates. This model includes temperature dependence, strain rate dependence, isotropic hardening, and anisotropic hardening effects for polycrystalline silicates such as olivine. It also captures history dependence arising from strain rate and/or temperature changes, a feature that power law models cannot achieve. We obtain the required model constants for several olivine aggregates from experimental data available in the current literature. The constants reported in this paper include those for wet olivine, dry olivine, lherzolite, and marble. Finally, although the material constants determined in this initial survey were non-unique relative to the experimental data currently available, we present an experimental matrix by which unique constants can be obtained.

References

Armstrong, P.J. & Frederick, C.O., 1996. A Mathematical representation of the multiaxial bauschinger effect, CEGB Report RD/B/N, pp. 731.

Ashby, M.F., 1970. The deformation of plastically non-homogeneous materials, *Philos. Mag.*, **21**, 399-424.

Aubertin, M., Gill, D.E. & Ladanyi B., 1991. An internal variable model for the creep of rocksalt, *Rock Mechanics and Rock Engineering*, **24**, 81-97.

Aubertin, M., Gill, D.E. & Ladanyi, B., 1991. A unified viscoplastic model for the inelastic flow of alkali Halides, *Mech. of Matls.*, **11**, 63-82.

Bammann, D.J., 1998. Modelling the large strain-high temperature response of metals, in *Modelling and Control of Casting and Welding Processes IV*, pp. 329-338, eds. Giamei, A.F. & Abbaschian, G.J. TMS Publications, Warrendale, PA.

Bammann, D.J. & Aifantis, E.C., 1989. A damage model for ductile metals, *Nuclear Engineering and Design*, **116**, 355-362.

Bammann, D.J., 1990. Modelling temperature and strain rate dependent large deformations of metals. *Appl. Mech. Rev.*, **1**, 312-318.

Bammann, D.J., Chiesa, M.L., Horstemeyer, M.F. & Weingarten, L.I., 1993. Failure in ductile materials using finite element methods, in *Structural Crashworthiness and Failure*, eds. Jones, N. & Weirzbicki, T., Elsevier Applied Science.

Bammann, D.J., Chiesa, M.L. & Johnson, G.C., 1995. Modelling large deformation anisotropy in sheet metal forming, in *Simulation of Materials Processing: Theory, Methods, and Applications*, eds. Shen and Dawson, Balkema, Rotterdam.

Baumgardner, J.R., 1985. Three-dimensional treatment of convective flow in the earth's mantle, *J. Stat. Phys.*, **39**, 501-511.

Bilby, B. A., Bullough R., & Smith, E., 1955. Continuous Distributions of Dislocations: A New Application of the Methods of Non-Riemannian Geometry, *Proc. R. Soc.*, London, Ser. A, **231**, 263-273.

Bunge, H.P., Richards, M.A. & Baumgardner, J.R., 1996. The effect of depth-dependent viscosity on the planform of mantle convection, *Nature*, **379**, 436-438.

Carter, N.L., 1976. Steady state flow of rocks, *Rev. Geophys. Space Phys.*, **14**, 301-360.

Carter, N.L. & Ave Lallemant, H.G., 1970. High temperature flow of dunite and perodidite, *Geol. Soc. Am. Bull.*, **81**, 2181-2202.

Chaboche, J.L., 1972. Description thermodynamique et phenomenologique de la viscoplasticite cyclique avec endommagement, These Univ. Paris VI, publication ONERA, N 1978-3.

Chopra, P.N. & Paterson, M.S., 1981. The experimental deformation of dunite, *Tectonophysics*, **78**, 453-473.

Chopra, P.N. & Paterson, M.S., 1984. The role of water in the deformation of dunite, *J. Geophy. Res.*, **89**, No. B9, 7861-7876.

Coleman, B.D. & Gurtin, M.E., 1967. Thermodynamics with internal state variables, *J. Chem.Phys.*, **47**, 597.

Covey-Crump, S.J., 1994. The Application of Hart's state variable description of inelastic deformation to Carrara Marble at T<450C, *J. Geophys. Res.*, **99**, No. B10, 19793-19808.

Eckart, C., 1940. Thermodynamics of irreversible processes, I. the simple fluid, *Phys. Rev.*, **58**, 267.

Eckart, C., 1948. Theory of elasticity and anelasticity, *Phys. Rev.*, **73**, 373.

Egydio-Silva, M. & Mainprice, D., 1999. Determination of stress directions from Plagioclase fabrics in high grade deformed rocks (Alem Paraiba Shear Zone, Ribeira Fold Belt, Southeastern Brazil), *J. Struct. Geology*, **21**, No.12, 1751-1771.

Frost, H. J. & Ashby, M. F. 1982. *Deformation-mechanisms Maps: The Plasticity and Creep of Metals and Ceramics*. Pergamon Press, pp. 166.

Garofalo, F., 1963. An empirical relation defining the stress dependence of minimum creep rate of metals, *Trans. Metall. Soc. AIME*, **227**, 351-356.

Germain, P., Nguyen, Q.S. & Suquet, P., 1983. Continuum thermodynamics, *J. Appl. Mech.*, **50**, 1010-1020.

Goetze, C., 1978. The mechanisms of creep in olivine, *Phil. Trans. R. Soc. Lond.*, **288 A**, 99-119.

Hart, E.W., 1970. A phenomenological theory for plastic deformation of polycrystalline metals, *Acta Metall.*, **18**, 599-610.

Hart, E.W., 1976. Constitutive relations for the nonelastic deformation of metals, *J. Enger. Mater. Tech.*, **98**, 193-202.

Horstemeyer, M.F., Lathrop, J., Gokhale, A.M. & Dighe, M., 2000. Modeling Stress State Dependent Damage Evolution in a Cast Al-Si-Mg Aluminum Alloy, *Theoretical and Applied Fracture Mechanics*, **33**, 31-47.

Karato, S.I., Paterson, M.S. & Fitzgerald, J.D., 1986. Rheology of synthetic olivine aggregates: influence of grain size and water, *J. Geophys. Res.*, **91**, B8, 8151-8176.

Karato, S.I. & Toriumi, M., 1989. *Rheology of Solids and of the Earth*, Oxford Science Publications, Oxford.

Kirby, S.H., 1983. Rheology of the lithosphere, *Reviews Geophys. Space Phys.*, **21**, pp. 1458-1487.

Kirby, S.H. & Kronenberg, A.K., 1987. Rheology of the lithosphere: selected topics, *Reviews of Geophysics*, **25**, No. 6, 1219-1244.

Kohlstedt, D.L. & Goetze, C., 1974. Low-stress high-temperature creep in olivine single crystals. *J. Geophys. Res.*, **79**, 2045-2051.

Krajcinovic, D., 1983. Constitutive equations for damaging materials, *J. Appl. Mech.*, **50**, 355-360.

Kroner, E., 1964. *Course 3: Continuum Theory of Defects*, Institute fur Theoretische und Angewandte Physik der Universitat Stuttgart und Max Planck Institut fur Metallforschung, Stuttgart, Germany.

Lee, E. H. & Liu, D. T., 1967. Finite Strain Elastic-plastic Theory with Application to Plane-Wave Analysis, *J. Appl. Physics*, **38**, 391-408.

Nicolas, A. & Poirer, J.P., 1976. *Crystalline Plasticity and Solid State Flow in Metamorphic Rocks*, Wiley, New York.

Onat, E.T. & Fardshisheh, F., 1972. Representation of creep of metals, ORNL Report 4783.

Onsager, L., 1931a. Reciprocal relations in irreversible processes, *Phys. Rev.*, **37**, 405.

Onsager, L., 1931b. Reciprocal relations in irreversible processes, *Phys. Rev.*, **38**, 2265.

Rice, J. R., 1971. Inelastic constitutive relations for solids: an internal-variable theory and its application to metal plasticity, *J. Mech. Phys. Solids*, **9**, 433-455.

Simmons, G. & Wang, H. 1971. *Single Crystal Elastic Constants and Calculated Aggregate Properties: A Handbook*, M.I.T. Press, Cambridge, MA.

Tsenn, M. C. & Carter, N. L., 1987. Upper limits of power law creep of rocks. *Tectonophysics*, **136**, 1-26.

CHAPTER III

TWO DIMENSIONAL MANTLE CONVECTION SIMULATIONS USING THE BAMMANN INELASTICTY INTERNAL STATE VARIABLE MODEL

Introduction

Mantle convection is currently understood to be a driving force behind plate tectonics. Mantle convection has been modeled by many researchers to understand how this convection interacts with the cold strong lithosphere. The predominant method used to model mantle convection is to solve the equations of fluid dynamics for a highly viscous fluid. This has proven useful in determining the convective flow patterns and structures that can arise from various types of boundary conditions. One aspect that has not been addressed in the community is to model mantle materials using a robust solid mechanics model that has the capability of capturing a materials deformational history.

The geologic community has used power-law type equations and exponential type equations for their material models over the years (Karato, 2008). Two kinds of power-law equations regularly used are power-law plastic flow rule and the power-law creep. (cf. Kirby, 1983; Goetze, 1977; Karato and Toriumi, 1989; Chopra and Paterson, 1981, 1984). These models have the ability to include time dependent temperature, strain rate, pressure, and in some cases grain size effects (Karato, 2008). The one limitation that the geologic community has lacked is the inclusion of a materials history in determining a material's strength. To address some of these limitations, Covey-Crump (1994) employed

the Hart internal state variable model (1970, 1976) to study the mechanical properties of Carrara Marble. Aubertin *et al.* (1991, 1992) also applied an internal state variable model to analyze rock salt and other alkali halides.

Some other recent works that have deviated from the traditional non-history dependent models are the works of Tackley (1998) and Auth *et al.* (2003). Both of these studies used a sort of history dependence through the use of a damage parameter in the determination of the materials strength. Tackley (1998) used a damage parameter and a strain-rate weakening rheology to produce shear localization that produced faults in a two dimensional convection calculation. In his three dimensional calculations the surface broke into multiple high viscosity plates separated by clearly defined low viscosity weak zones.

The work by Auth *et al.* (2003) uses a simple damage rheology to show the emergence of self lubricating behavior and low viscosity zones that can be thought of as faults. The advantage of the Auth *et al.* (2003) over the Tackley (1998) method is the time dependent damage parameter inherently has history dependence where the material remembers its previous deformation. The deformational history is important, because Gurnis *et al.* (2000) showed the long lived weak zones are thought to influence plate tectonics.

Mantle convection inherently is a three dimensional problem, but due to computational limitations many two dimensional codes have been developed to gain an understanding of the fundamental mechanisms. The other beneficial aspect of modeling in two dimensions is the ability to achieve extremely high resolutions on the order of 1 km or less. The two dimensional work started with calculations of steady convection at

large Raleigh number (McKenzie *et al.*, 1973, 1974; Hewitt *et al.*, 1980; Jarvis, 1984; Schubert and Anderson, 1985; Olson, 1987; Christensen, 1989). Internal heating was also included, which Schubert *et al.* (2001) argues this and some basal heating more accurately models whole mantle convection. The work conducted by Jarvis (1984), Hansen *et al.* (1990), and Yuen *et al.* (1993) on an isoviscous fluid determined that the inclusion of internal heating produces time-dependent behavior in the convection process. Thermal boundary layer instabilities are the main time-dependent source in these calculations. Hansen *et al.* (1990) and Yuen *et al.* (1993) have labeled this as soft turbulence.

An important addition regarding two dimensional mantle convection calculations is the inclusion of temperature dependent viscosity. The calculations done by Houston and De Bremaecker (1975), Parmentier *et al.* (1976), Daly (1980), Jacoby and Schmeling (1982), Tackley (1993), Christensen (1984), Moresi and Solomatov (1995), and Ratcliff *et al.* (1997) all included temperature dependent viscosity. Moresi and Solomatov (1995) reveal three different convection regimes in fluids with variations in viscosity. These three regimes are based on the temperature dependent material models. The first regime involves viscosity ratios under 100 and nearly equivalent to isoviscous simulations. The second regime, called episodic involves viscosity ratios over 100 but less than 1000. The third regime is for viscosity ratios greater than 3000 in which a cold rigid thermal boundary layer develops on the upper surface. This form is called rigid lid convection.

The purpose of this work is to incorporate a material model that more accurately captures the deformation of the mantle materials into a mantle convection code. In the engineering community many have shown that a materials history is crucial to predicting

its stress state at any given time. In order to capture the history effects the community began developing models using internal state variables. The internal state variables allow for a materials history to be carried along and used to determine the stress state under particular loading conditions.

In this study we have chosen to use the Bammann inelasticity internal state variable model (BIISV) (Bammann, 1990). This model has the capability to capture the finite inelastic deformation of any polycrystalline material. Since the geomaterials applicable to mantle convection are polycrystalline and the materials deform by dislocation creation, motion, and annihilation, the BIISV is ideal for this purpose.

Model Description

For this study we have chosen to implement the BIISV into the code TERRA2D developed by Yang and Baumgardner (2000). TERRA2D treats the Earth's mantle as a viscous fluid. Because the viscosity of the silicate materials is on the order of 10^{21}, the corresponding Prandtl number is on the order of 10^{24}. Following the argument of Turcotte *et al.*, 1973, the viscous terms in the momentum equations so large compared to the inertial terms that the latter may be dropped altogether in the momentum equation. We also make the Boussinesq approximation and assume density is constant everywhere except in the buoyancy term of the momentum equation. In the buoyancy term the density depends linearly on the temperature variations. Using these approximations, the following simplified conservation of mass, momentum, and energy equations for a two dimensional rectangular domain are used to describe thermal convection in the Earth's mantle (Baumgardner, 1983, 1985):

$$\frac{\partial u_m}{\partial x_m} = 0\,, \tag{3.1}$$

$$\frac{\partial \tau_{lm}}{\partial x_m} - \frac{\partial p}{\partial x_l} + \rho_0 g\alpha\left(T - T_0\right)\delta_{l2} = 0 \quad \left(l = 1,2\right), \tag{3.2}$$

$$\rho_0 c_p\left(\frac{\partial T}{\partial t} + u_l\frac{\partial T}{\partial x_l}\right) = \frac{\partial}{\partial x_l}\left(k\frac{\partial T}{\partial x_l}\right) + \rho_0 H\,, \tag{3.3}$$

where u, τ, p, ρ_0, g, α, T, T_0, c_p, k and H are the velocity, deviatoric stress, dynamic pressure, reference density, gravitational acceleration, thermal expansion coefficient, temperature, reference temperature, specific heat at constant pressure, thermal conductivity and radiogenic heat generation rate per unit mass, respectively. The constitutive relation is needed to relate the deviatoric stress to velocity, which is given by

$$\tau_{lm} = \mu\left(\frac{\partial u_l}{\partial x_m} + \frac{\partial u_m}{\partial x_l}\right), \tag{3.4}$$

where μ is the effective dynamic viscosity. The effective dynamic viscosity is where the BIISV model will be implemented. This implementation will allow for a high fidelity solid mechanics inelasticity continuum model to work with a fluid dynamics type problem.

The numerical solution to Equations (3.1)-(3.4) is found in Yang and Baumgardner, 2000, which will briefly be described here. The physical domain is a rectangular box with a domain range of $0 < x < w$ and $0 < y < h$. The mesh is a structured rectangular mesh with $(n_1 + 1) \times (n_2 + 1)$ number of nodes. Two layers of ghost nodes are included to accommodate various boundary conditions. The finite element method is used to discretize Equations (3.1) and (3.2). Velocity is naturally located at the nodes while other dependent variable values are located at the cell centers. The process of solving

Equations (3.1)-(3.4) first involves simultaneously solving Equations (3.1), (3.2), and (3.4) for velocity and pressure and then solving Equation (3.3) for temperature. The method chosen to solve for velocity and pressure simultaneously combines the conjugate gradient algorithm in an outer loop and a matrix dependent transfer multigrid method inside this loop. The matrix dependent transfer multigrid scheme described in Yang and Baumgardner (2000) allows for extremely large viscosity variations. Once the velocity and pressure fields are determined, the temperature and viscosity are updated. Equation (3.3) is solved for temperature using a monotone upwind advection method detailed in Yang and Baumgardner (2000) together with 2nd order Runge-Kutta time integration scheme. The velocity-pressure solver has an extremely high convergence rate. Details can be found in Yang and Baumgardner (2000).

The boundary conditions used in this study will now be described. On the top and bottom of the domain the conditions are that of zero normal velocity and zero shear stress, corresponding to free slip boundaries. The side boundary conditions are chosen to be periodic by imposing appropriate velocities on the ghost nodes. Unless otherwise stated, the thermal boundary conditions are a constant temperature of 300 K on the upper boundary and a constant 3000 K on the bottom boundary, except when the bottom heat flux is specified to be zero. The initial vertical temperature profile is given by:

$$T_i(y) = \begin{cases} T_{lower} + \dfrac{T_{ref} - T_{lower}}{5} y, & 0 < y < 5 \\ T_{ref}, & 5 < y < n_2 - 5 \\ T_{upper} + \dfrac{T_{ref} - T_{upper}}{5}(n_2 - y), & n_2 - 5 < y < n_2 \end{cases} \quad (3.5)$$

.

This represents an initial upper and lower thermal boundary layer that is 5 elements thick. When base heating is not included, the bottom five layers are loaded with the reference temperature.. The initial horizontal temperature profile is given by

$$T(x,y) = T_i(y) + 0.03T_i(y)(h/2)\cos\frac{2\pi x}{w}, \tag{3.6}$$

which represents a temperature field with two convecting cells.

The previous work (Yang and Baumgardner, 2000) used two different rheological models to evaluate the matrix-dependent transfer multigrid method. The first model for effective viscosity was a simple temperature dependent Newtonian material given by

$$\mu_N = \mu_0 \exp\left[\frac{E}{R}\left(\frac{1}{T} - \frac{1}{T_0}\right)\right] \tag{3.7}$$

where μ_0, E, R, and T_0 are the reference viscosity, activation energy, gas constant, and reference temperature, respectively. The second model for effective viscosity was a non-Newtonian expression that used a power-law rheology that included strain rate effects given by the following,

$$\mu_P = \mu_0 \left(\frac{\dot{\varepsilon}}{\dot{\varepsilon}_0}\right)^{(1/n)-1} \exp\left[\frac{E}{nR}\left(\frac{1}{T} - \frac{1}{T_0}\right)\right] \tag{3.8}$$

where $\dot{\varepsilon}$ is the second invariant of the strain rate tensor, $\dot{\varepsilon}_0$ is a transition strain rate that marks the onset of power-law behavior, and n is the power-law exponent. This was then worked into a non-Newtonian rheology by computing a composite effective viscosity given by the following,

$$\mu_C = \frac{\mu_N \mu_P}{\mu_N + \mu_P} \tag{3.9}$$

The composite model was introduced with the purpose of representing the fact that Newtonian or diffusional creep dominates at very low strain rates and power law dominates at higher strain rates. The input parameter $\dot{\varepsilon}_0$ determines the transition strain rate at which this change occurs.

In order to accommodate brittle failure in the cold thermal boundary layer an artificial maximum viscosity is imposed when a user specified yield stress is exceeded by the following,

$$\mu_{\max} = \frac{\tau_Y}{2\dot{\varepsilon}} \tag{3.10}$$

Using TERRA2D, Yang and Baumgardner (2000) found that the type of convection flow is highly sensitive on the choice of yield stress when used in conjunction with either the Newtonian or non-Newtonian rheology.

A full explanation of the BIISV model is explained previously in chapter 2 so the model equations based on Bammann (1990) will be briefly described here. The kinematics is discussed thoroughly by Bammann and Alfantis (1987) and Bammann and Johnson (1987). The model is based on the multiplicative decomposition of the deformation gradient into elastic and plastic parts and assumes isotropic linear elasticity with respect to the natural configuration. The linear elasticity assumption can be written,

$$\overset{\circ}{\underline{\sigma}} = \lambda \operatorname{tr}\left(\underline{D}^e\right) + 2\mu \underline{D}^e , \tag{3.11}$$

where, λ and μ are the Lamé elastic constants. The Cauchy stress $\underline{\sigma}$ is advected with the elastic spin $\underline{W}^e$ as,

$$\overset{\circ}{\underline{\sigma}} = \dot{\underline{\sigma}} - \underline{W}^e \underline{\sigma} + \underline{\sigma} \underline{W}^e , \tag{3.12}$$

which is done in order to keep the rate objective. The velocity gradient can be broken into both symmetric and skew symmetric parts with each being decomposed into elastic and plastic parts. The elastic stretching $\underline{D}^e$ and elastic spin $\underline{W}^e$ can be written,

$$\underline{D}^e = \underline{D} - \underline{D}^{in} \tag{3.13}$$

$$\underline{W}^e = \underline{W} - \underline{W}^{in} \tag{3.14}$$

Due to this decomposition, it is now appropriate to prescribe an equation for both the inelastic spin $\underline{W}^{in}$ and the flow rule $\underline{D}^{in}$. In this paper we will make the assumption that the elastic spin equals the total spin (i.e., $\underline{W}^e = \underline{W}$). The flow rule of the form

$$\underline{D}^{in} = f(T)\sinh\left[\frac{\left\|\underline{\sigma}' - \underline{\alpha}\right\| - \kappa - Y(T)}{V(T)}\right]\frac{\underline{\sigma}' - \underline{\alpha}}{\left\|\underline{\sigma}' - \underline{\alpha}\right\|} \tag{3.15}$$

where T is the temperature, κ is a scalar hardening variable, $\underline{\alpha}$ is a tensor variable, $\underline{\sigma}'$ is the deviatoric Cauchy stress, and $V(T)$, $Y(T)$, $f(T)$ are the temperature dependent scalar functions,

$$V(T) = C_1 \exp\left(\frac{-C_2}{T}\right) \tag{3.16}$$

$$Y(T) = \frac{1}{2}C_3 \exp\left(\frac{C_4}{T}\right)\left(1 + \tanh\left[C_{19}\left\{C_{20} - T\right\}\right]\right) \tag{3.17}$$

$$f(T) = C_5 \exp\left(\frac{-C_6}{T}\right). \tag{3.18}$$

The evolution of the internal state variables $\underline{\alpha}$ and κ are prescribed in a hardening minus recovery format, which is motivated from the dislocation mechanics

concept of dislocation creation, motion, and annihilation. The evolution equations are given by

$$\overset{\circ}{\underline{\alpha}} = h(T)\underline{D}^{in} - \left[\sqrt{\frac{2}{3}} r_d(T)\left\|\underline{D}^{in}\right\| + r_s(T)\right]\|\underline{\alpha}\|\underline{\alpha} \tag{3.19}$$

$$\dot{\kappa} = \sqrt{\frac{2}{3}} H(T)\left\|\underline{D}^{in}\right\| - \left[\sqrt{\frac{2}{3}} R_d(T)\left\|\underline{D}^{in}\right\| + R_s(T)\right]\kappa^2 . \tag{3.20}$$

The internal state variable $\underline{\alpha}$ is also advected with the elastic spin $\underline{W}^e$ exactly the same way the Cauchy stress is by Equation (3.12). The temperature dependent functions $r_d(T)$ $h(T)$, $r_s(T)$, $R_d(T)$, $H(T)$, $R_s(T)$ are the following:

$$r_d(T) = C_7 \exp\left(\frac{-C_8}{T}\right) \tag{3.21}$$

$$h(T) = C_9 - C_{10}T \tag{3.22}$$

$$r_s(T) = C_{11} \exp\left(\frac{-C_{12}}{T}\right) \tag{3.23}$$

$$R_d(T) = C_{13} \exp\left(\frac{-C_{14}}{T}\right) \tag{3.24}$$

$$H(T) = C_{15} - C_{16}T \tag{3.25}$$

$$R_s(T) = C_{17} \exp\left(\frac{-C_{18}}{T}\right). \tag{3.26}$$

Hence the BIISV model involves a total of 20 constants for each material. The experiments necessary to find these constants were described in chapter 2. The BIISV model has the added benefit of being able to reproduce the behavior of other simpler models simply by setting certain constants to zero. This feature will be useful when

comparing the implementation of this model to the non-Newtonian model described earlier.

Implementation

The implementation of the BIISV into TERRA2D follows the approach of Bammann *et al.* (1993) with some modifications to accommodate TERRA2D's structure. The overall set of equations including Equations (3.11) through (3.26) can be integrated numerically using an explicit method such as a forward Euler or an implicit method such as the Newton-Raphson method. However, a considerable smaller time step is usually needed compared to the finite element time step limit imposed by the conservation equations. For this reason, Bammann *et al.* (1993) implemented the BIISV scheme using the radial return method as proposed by Krieg & Krieg (1977). This allows for a much higher overall efficiency. The procedure for implementing BIISV within TERRA2D and calculating the effective viscosity is as follows and is accomplished in eight steps.

Step 1

Before the steps begin TERRA2D advances the velocity field to the next time level N+1 where N is the time step index. The temperature dependent functions given by Equations (3.16) through (3.18) and Equations (3.21) through (3.26) are then evaluated at time t_N.

Step 2

The values for stress and the tensor internal state variable from time step N are rotated to maintain objectivity, which will be later used. The symmetric part of the velocity gradient $\underline{D}_{N+1}$ and the antisymmetric part of the velocity gradient, also known as the total spin,

$\underline{W}_{N+1}$ at the current time step is calculated from the new velocity field. The rotated values are calculated by

$$\underline{\sigma}'^{R}_{N} = \underline{\sigma}'_{N} + \underline{W}_{N+1}\underline{\sigma}'_{N}\Delta t - \underline{\sigma}'_{N}\underline{W}_{N+1}\Delta t \tag{3.27}$$

$$\underline{\alpha}^{R}_{N} = \underline{\alpha}_{N} + \underline{W}_{N+1}\underline{\alpha}_{N}\Delta t - \underline{\alpha}_{N}\underline{W}_{N+1}\Delta t \tag{3.28}$$

Note that only the deviatoric Cauchy stress is required for this implementation. In the current implementation only the deviatoric stresses are needed to calculate the effective viscosity. Therefore, the model equations can be reduced by considering only the deviatoric part of the current total symmetric velocity gradient, $\underline{D}_{N+1}$. The deviatoric symmetric velocity gradient is calculated by

$$\underline{d}_{N+1} = \underline{D}_{N+1} - \frac{1}{3}\mathrm{tr}\left(\underline{D}_{N+1}\right)\underline{I} \tag{3.29}$$

Step 3

Trial deviatoric stresses and internal state variables are then calculated assuming the deformation is purely elastic using Equations (3.11), (3.19), and (3.20):

$$\underline{\sigma}'^{TR} = \underline{\sigma}'^{R}_{N} + 2\mu\underline{d}_{N+1}\Delta t \tag{3.30}$$

$$\underline{\alpha}^{TR} = \underline{\alpha}^{R}_{N} - \left(r_s - r_d\left\|\tilde{\underline{d}}_{N+1}\right\|\right)\left\|\tilde{\underline{\alpha}}^{R}_{N}\right\|\underline{\alpha}^{R}_{N}\Delta t \tag{3.31}$$

$$\kappa^{TR} = \kappa_N - \left(R_s - R_d\left\|\tilde{\underline{d}}_{N+1}\right\|\right)\kappa_N^2\Delta t \tag{3.32}$$

where the current time step Δt is used and the magnitudes of the deviatoric symmetric velocity gradient and the tensor internal state variable are defined as:

$$\left\|\tilde{\underline{d}}_{N+1}\right\| = \sqrt{\frac{2}{3}}\left\|\underline{d}_{N+1}\right\| \tag{3.33}$$

$$\left\|\underline{\tilde{\alpha}}^{R}_{N+1}\right\| = \sqrt{\frac{2}{3}}\left\|\underline{\alpha}^{R}_{N+1}\right\|. \tag{3.34}$$

Step 4

The elastic assumption is now checked. The flow rule is inverted and rearranged into a yield condition form typical of classical plasticity (Khan and Huang, 1995).

$$\phi^{TR} = \left\|\underline{\sigma}'^{TR} - \frac{2}{3}\underline{\alpha}^{TR}\right\| - \sqrt{\frac{2}{3}}\left(\kappa^{TR} + Y\left(T_N\right) + V\left(T_N\right)\sinh^{-1}\left(\frac{\left\|\underline{\tilde{d}}_{N+1}\right\|}{f\left(T_N\right)}\right)\right) \tag{3.35}$$

Step 5

If $\phi^{TR} \le 0$ then the step is elastic and the deviatoric stresses and internal state variables are set to their respective trial values. However, if $\phi^{TR} > 0$ then inelastic deformation has occurred, and the trial deviatoric stresses must be returned to the new yield surface by the following:

$$\underline{\sigma}'_{N+1} = \underline{\sigma}'^{TR} - \int 2\mu \underline{d}^{in}_{N+1} dt \tag{3.36}$$

$$\underline{\alpha}_{N+1} = \underline{\alpha}^{TR} + \int h\underline{d}^{in}_{N+1} dt \tag{3.37}$$

$$\kappa_{N+1} = \kappa^{TR} + \int H\left\|\underline{\tilde{d}}^{in}_{N+1}\right\| dt\,. \tag{3.38}$$

Step 6

Using the radial return method, the assumption is made that the inelastic strain rate is constant over the time step and is in the direction of the effective stress (coaxiality) which is given as:

$$\underline{\xi}^{TR} = \underline{\sigma}'^{TR} - \frac{2}{3}\underline{\alpha}^{TR} \tag{3.39}$$

$$\underline{n} = \frac{\underline{\xi}^{TR}}{\left\| \underline{\xi}^{TR} \right\|} \tag{3.40}$$

$$\int \underline{d}_{N+1}^{in} dt = \Delta\gamma \underline{n} \tag{3.41}$$

where $\underline{n}$ is the direction of the effective stress $\underline{\xi}$ and $\Delta\gamma$ is the inelastic strain increment, which will be used later to update the new values of stress and internal state variables.

Step 7

The inelastic strain increment is then substituted into Equations (3.36) through (3.38) to yield

$$\underline{\sigma}'_{N+1} = \underline{\sigma}'^{TR} - 2\mu\Delta\gamma \underline{n} \tag{3.42}$$

$$\underline{\alpha}_{N+1} = \underline{\alpha}^{TR} + h\Delta\gamma \underline{n} \tag{3.43}$$

$$\kappa_{N+1} = \kappa^{TR} + \sqrt{\frac{2}{3}} H \Delta\gamma \tag{3.44}$$

Step 8

Using Equations (3.42) through (3.44) the consistency condition can be used to solve for $\Delta\gamma$. With the assumptions made earlier the solution of $\Delta\gamma$ is a linear algebraic equation. The inelastic strain increment is found to be

$$\Delta\gamma = \frac{\phi^{TR}}{2\mu + \frac{2}{3}(h + H)} \tag{3.45}$$

The computed value of the inelastic strain increment can then be used to update the stress and internal state variables for the next time step given in Equations (3.42) through

(3.44). The inelastic strain increment can also be used to update the current inelastic strain to keep track of the amount of inelastic deformation. This is given by

$$\varepsilon_{N+1}^{in} = \varepsilon_N^{in} + \sqrt{\frac{2}{3}}\Delta\gamma \,. \tag{3.46}$$

Finally, the effective viscosity is updated by the following relationship,

$$\mu_{ISV} = \frac{\left\|\underline{\tilde{\sigma}}'_{N+1}\right\|}{2\left\|\underline{\tilde{d}}_{N+1}\right\|} \tag{3.47}$$

One last topic needs to be addressed regarding the implementation. Due to the fact that TERRA2D is an Eulerian code the internal state variables need to be advected in order for the material's deformational history to be carried in the flow. We chose to use the same monotone upwind method used to advect the temperature in the energy equation as described by Yang and Baumgardner (2000). This is a first order method and so numerical diffusion is an issue, but at sufficiently high resolution this becomes negligible. A mesh refinement study was conducted to determine the resolution required. The computational cost needed by this method for the 512 elements by 128 elements mesh used in this study required about 9 percent of the overall computational time.

Numerical Simulations Setup

The first step in verifying the implementation described in the previous section was to match a previously run simulation using BIISV model. The BIISV model constants were chosen in order to closely resemble the power law model in TERRA2D. A mesh refinement study showed that a mesh of 512 elements by 128 elements was ideal for running simulations for large scale convection patterns. This was the same size that Yang and Baumgardner (2000) used. With a domain size of 11560 km by 2890 km, the

length of each element was approximately 22.57 km per element. The resolution was not high enough to resolve small scale flow features, but the large scale flow features were realized. The 512 elements by 128 elements grid was used for all the subsequent simulations. The numerical diffusion in the history variables was minimal for all the simulations conducted at this resolution. The other constants relevant to the simulations performed in this study are given in Table 3.1. The constants in Table 3.1 are the same constants used by Yang and Baumgardner (2000). This enabled a direct comparison between the power law model and BIISV model.

Table 3.1 Input parameters used for numerical simulations in this study.

width, w	11560 km
thickness, h	2890 km
horizontal number of cells, n_1	512
vertical number of cells, n_2	128
reference density, ρ_0	3400 kg m^{-3}
Gravitational acceleration, g	10 m s^{-2}
thermal expansion coefficient, α	2.5×10^{-5} K^{-1}
thermal conductivity, k	4 W m^{-1} K^{-1}
specific heat, c_p	10^3 J kg^{-1} K^{-1}
heat generation rate, H	5×10^{-12} W kg^{-1}
reference viscosity, μ_0	4×10^{23} Pa s
minimum viscosity, μ_{min}	0.01 μ_0
viscous yield stress, τ_y	100 MPa
reference temperature, T_0	1500 K

The Yang and Baumgardner (2000) constants for power law are given in Table 3.2. The BIISV model therefore needed to match the power law model given by these constants for a direct comparison. The simplest way to accomplish this with the BIISV was to take the flow rule given in Equation (3.15) and assume only constants C_1, C_2, and C_5 were needed to fit the power law model. Note that using only these constants no

history dependence arises. The BIISV model reduces to a rate and temperature dependent perfectly plastic model. The assumption was also made that the total strain rate was equal to the inelastic strain rate, $\|\underline{D}\| = \|\underline{D}^{in}\|$ for fitting purposes. Equation (3.15) was then inverted and solved for $\|\underline{\sigma}'\|$ as a function of the strain rate, $\|\underline{D}^{in}\|$. Equation (3.8) can also was solved for $\|\underline{\sigma}'\|$ assuming $\|\underline{\sigma}'\| = 2\mu\|\underline{D}^{in}\|$, where $\dot{\varepsilon}$ in Equation (3.8) was equivalent to $\|\underline{D}^{in}\|$ in Equation (3.15). The resulting reduced BIISV model and rearranged power law equation are the following

$$\|\underline{\sigma}'\| = C_1 \sinh^{-1}\left[\frac{\|\underline{D}^{in}\|}{C_5}\right]\exp\left(\frac{-C_2}{T}\right) \tag{3.48}$$

$$\|\underline{\sigma}'\| = 2\mu_0\dot{\varepsilon}_0^{1/n-1}\exp\left(\frac{-E}{nRT_0}\right)\|\underline{D}^{in}\|^{1/n}\exp\left(\frac{E}{nRT}\right). \tag{3.49}$$

Comparing Equation (3.48) to (3.49) the temperature dependence, C_2, was the easiest to fit, by simply looking at the constants inside the exponential in Equation (3.49). The strain rate dependence constants C_1 and C_5 were a bit more difficult to match. One of the difficulties was the mathematical form of the strain rate dependencies of the two equations were fundamentally different. With only two constants this meant that only a range of strain rates were able to correlate together. The strain rate range for the power law simulation was from 10^{-16} s^{-1} to 10^{-14} s^{-1}. The constants were determined by trial and error using the extraneous constants outside Equation (3.49) as C_1 and C_5 equaling 1.0 as the starting point. The constants were then varied until a suitable set adequately fit the strain rate range.

Table 3.2 Power law parameters used in this study.

Constant	Yang and Baumgardner (2000)	Lherzolite Experiment Fit
power-law exponent, n	3	2.3
activation energy, E	106.4 kJ mol^{-1}	334.1 kJ mol^{-1}
transition strain-rate, $\dot{\varepsilon}_0$	10^{-19} s^{-1}	10^{-26} s^{-1}

The final constants for this rate and temperature dependent perfectly plastic material are given in Table 3.3. Figure 3.1 shows the comparison between the power law model and the BIISV model at 1000 K using the constants found in Table 3.3. Notice that the shape of the power law model on a log-log plot is a straight line, and the BIISV has some curvature to it. This again is due to the difference between the mathematical forms of Equations (3.48) and (3.49). Looking at Figure 3.1 the BIISV model would have a softer response than the power law model outside this strain rate range. The parameters for the comparison simulation are given in Table 3.1. The upper boundary temperature is held at a constant 300 K. The case has only internal heating with no heat flux through the lower boundary. The results are described in the results section below.

Table 3.3 BIISV model parameters used in this study.

Constant	Perfectly Plastic	Viscoplastic	Lherzolite Experimental Fit
C1 (MPa)	0.04	1.0×10^{-5}	1.0×10^{-5}
C2 (K)	-4266	0.0	0.0
C3 (MPa)	1.0×10^{-5}	1.0×10^{-5}	1.0×10^{-5}
C4 (K)	0.0	0.0	0.0
C5 (s^{-1})	1.0×10^{-16}	1.0×10^{-5}	1.0×10^{-5}
C6 (K)	0.0	0.0	0.0
C15 (MPa)	0.0	4.99×10^{15}	1.03×10^{5}
C16 (MPa K^{-1})	0.0	4.98×10^{12}	65.8
C17 (s MPa^{-1})	0.0	0.004	4.15
C18 (K)	0.0	2996	1.63×10^{4}

The BIISV model can be made to approximate the Yang and Baumgardner (2000) power law model in a second way, however—one that involves the tracking of material history with an internal state variable. Using only the constants C_{15}, C_{16}, C_{17}, and C_{18} the BIISV model can be reduced to a viscoplastic type material response. Following the procedure of Bammann (1990) with only these constants the model can be reduced in the limit that the strain is very large (i.e. steady state) to the following

$$\left\|\underline{\sigma}'\right\| = \sqrt{\frac{H(T)\left\|\underline{D}^{in}\right\|}{R_s(T)}} \,. \tag{3.50}$$

The constants can be determined by using picking two sets of stress and strain rate data given from Equation (3.49). The temperatures were 1000 K and 1500 K and the strain rate range was over the same range as before, 10^{-16} s^{-1} to 10^{-14} s^{-1}. The resulting constants used to match the Yang and Baumgardner (2000) constants are given in Table 3.3 under the viscoplastic column. Small values for C_1, C_3, and C_5 are needed in order to not divide by zero in the implementation, but have no bearing on the material's stress response. Figure 3.2 shows a comparison between the perfectly plastic case and the viscoplastic case. Note that the stress response for the viscoplastic case is only plotted in the steady state limit. The material must harden and recover over time at the given strain rate to eventually reach these values. Due to the different mathematical form of equation (3.48) and (3.50), it is not surprising that the viscoplastic response has a straight line and cannot match the curve exactly. Notice in Figure 3.2 that the stress response in the lower part of the strain rate range is smaller and closer to 10^{-14} where the viscoplastic material has a stronger stress response. The viscoplastic material stress response is higher relative to a given strain rate. This is due to the square root dependence on the strain rate. The

viscoplastic constants are used to show that history dependence can be important in a mantle convection simulation. The simulation is identical to the previous simulation described using the constants in Table 3.1, and the results are given in the results section.

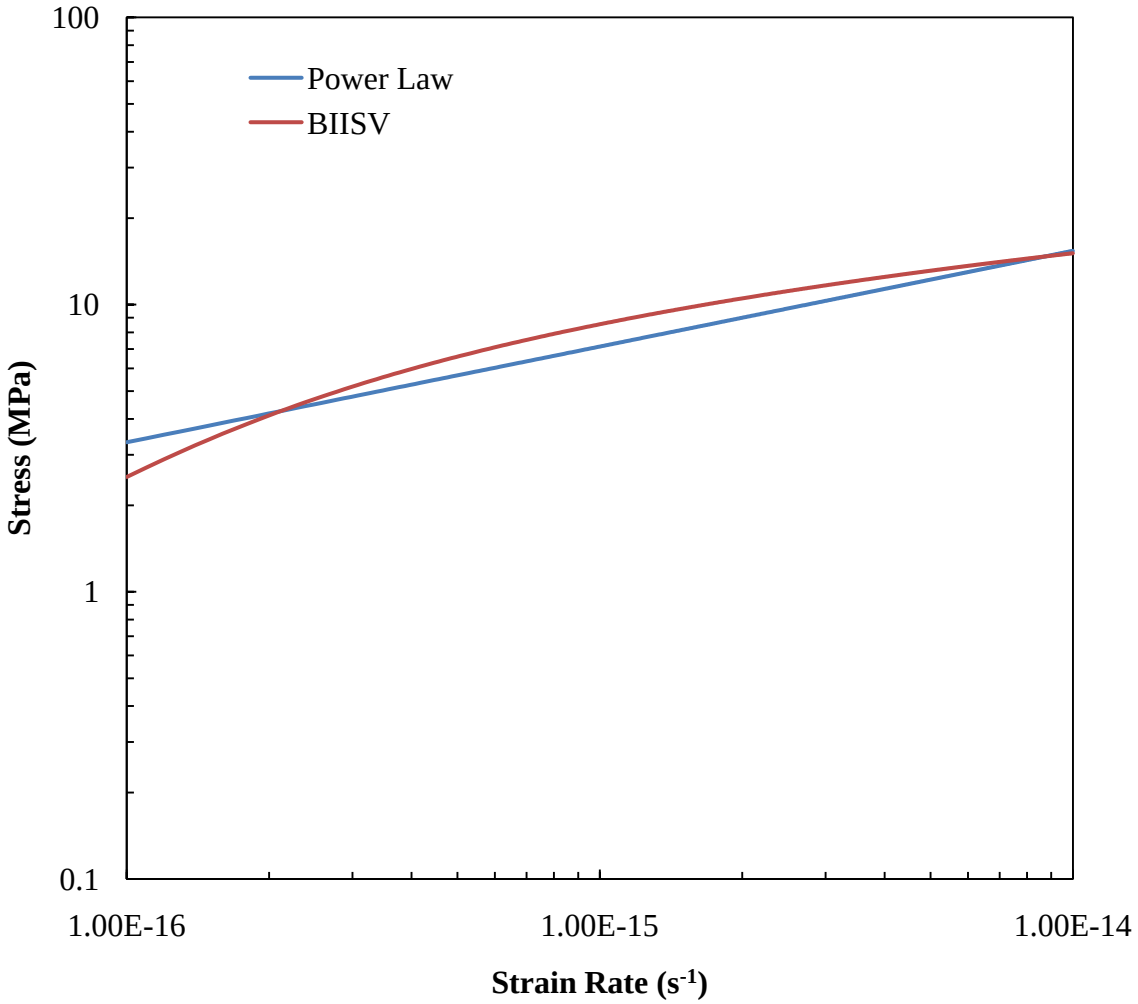

Figure 3.1 Comparison between the power law model used in Yang and Baumgardner, 2000, and BIISV model in the pertinent strain rate range at a temperature of 1000 K.

The final aspect of this study is to use experimental data found in the literature for real rocks as the basis for the BIISV material constants. These are then applied in an identical mantle convection simulation with power law constants in order to highlight the

differences between the two rheological models. The experimental stress-strain data used in this work was generated by Carter and Ave'Lallemant (1970). The BIISV model requires stress-strain data over large strain rates and temperatures in order to fully capture the materials response. Most data found in the literature omits the stress-strain data and is usually scarce. One of the materials that Carter and Ave'Lallemant (1970) tested was lherzolite, which is made up of 60-70 percent olivine. The lherzolite was chosen because the published stress-strain data spanned a broad range of temperatures. Power law constants were also included in the Carter and Ave'Lallemant (1970) work over the range of the experiments tested. These power law constants were used to compare to the BIISV model for the mantle dynamics simulations.

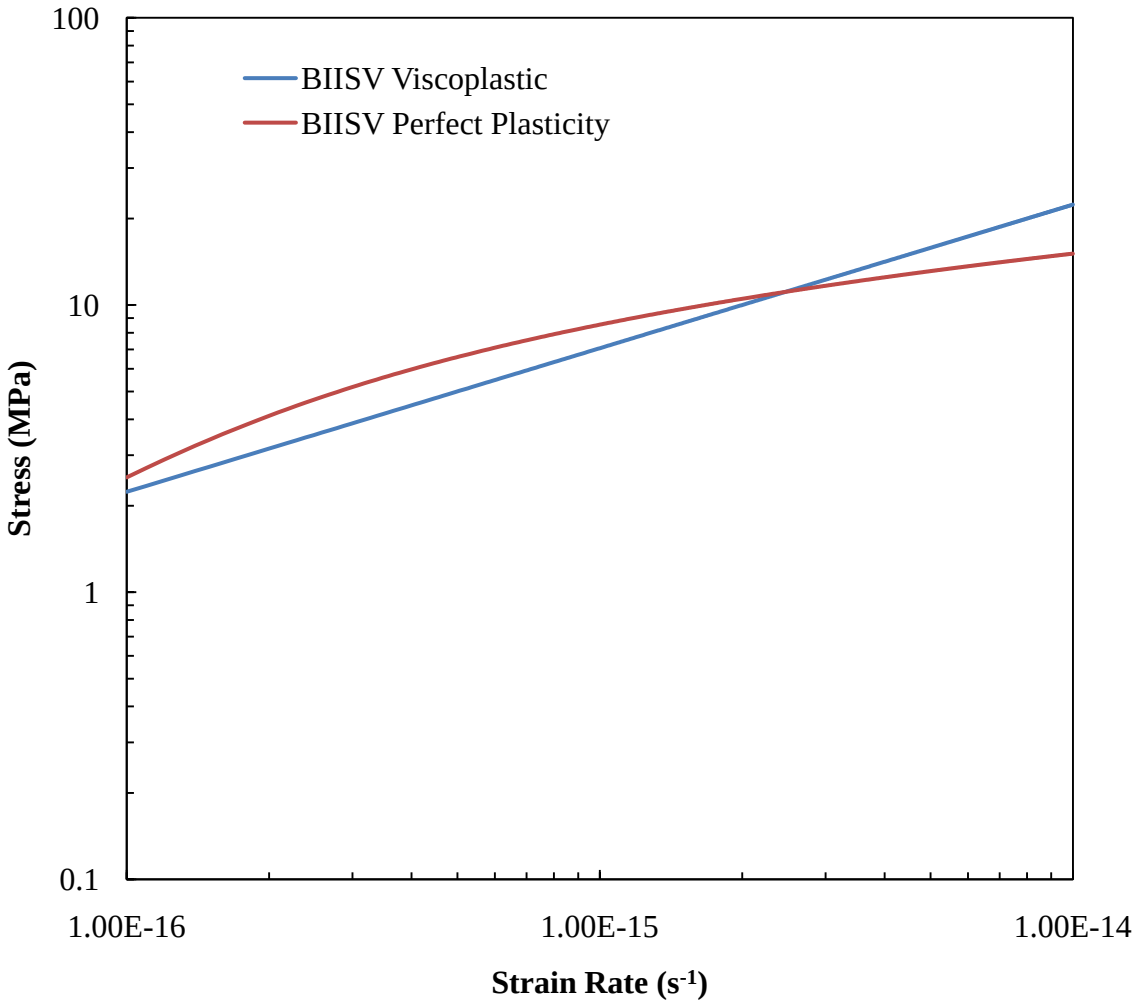

Figure 3.2 Comparison between BIISV perfectly plastic case and BIISV viscoplastic case over the pertinent range of strain rates.

The steps to determine unique constants are outlined in a companion paper and will not be elaborated here. The constants were fit to the experimental data using a nonlinear regression algorithm. The constants for lherzolite are given in Table 3.3 under the experimental lherzolite column. Notice the constants give the material a viscoplastic response much like the previously discussed simulation. Only isotropic hardening can be included due to a lack of reversed loading experimental data. The latter would have allowed determinations for the kinematic hardening constants also. The BIISV fit is

shown in Figure 3.3 for the range of temperatures 1123 K to 1333 K and a range of strain rates. Notice that some extrapolation is required much like the power law model for the extremely low strain rates involved in mantle convection.

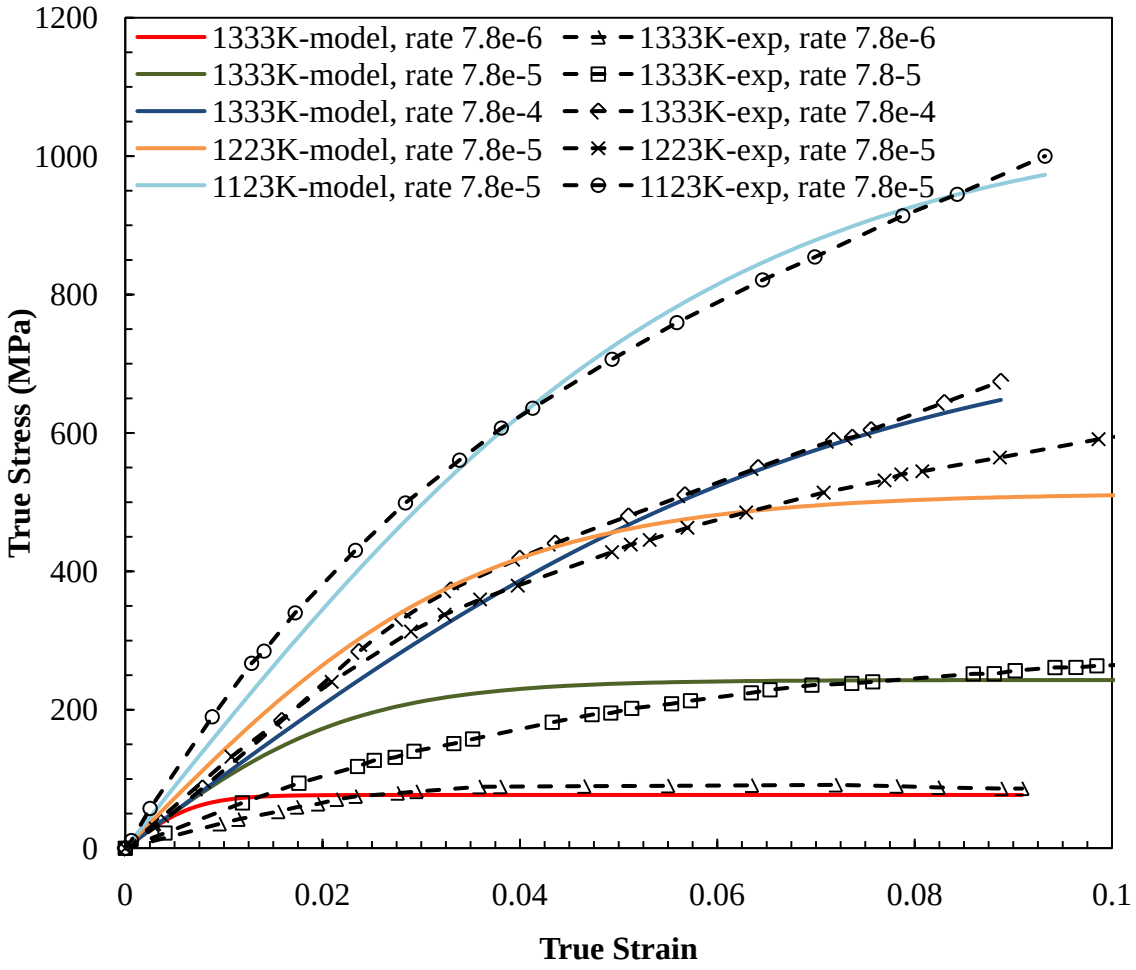

Figure 3.3 Comparison of BIISV model correlation to Lherzolite experimental data (Carter and Ave'Lallemant, 1970).

One of the strengths of the BIISV over the power law model highlighted by Figure 3.3 is the BIISV's ability to capture the transient and history behavior of a material. The BIISV does not assume steady state for a given strain rate. For an example of this point consider strain rate and temperature jump tests that Carter and

Ave'Lallemant (1970) included in their experiments. Using the constants determined for lherzolite the BIISV can be used to produce a strain rate jump test as shown in Figure 3.4. On a stress-strain curve the power law model produces a constant stress for a given strain rate. The power law curve in Figure 3.4 was produced using the power law constants given in Carter and Ave'Lallemant (1970), which are shown in Table 3.2. Notice the BIISV model does a much better job over the range of strain rates of capturing the stress response. For the case of the temperature jump tests, Figure 3.5 shows how the BIISV is far superior for this material correlation. Some of the power law predicted stresses for the higher temperature are not even shown in Figure 3.5 due to them being way off the scale. For reference, the values of stresses calculated from the power law model are 5.1 GPa and 1.43 GPa at 1123K and 1223K, respectively. One of the reasons the power law model has problems is that the experimental data in Carter and Ave'Lallemant (1970) at temperatures at 1123 K and lower do not reach steady state so extrapolations at lower temperatures are extremely inaccurate. The BIISV does not have this limitation.

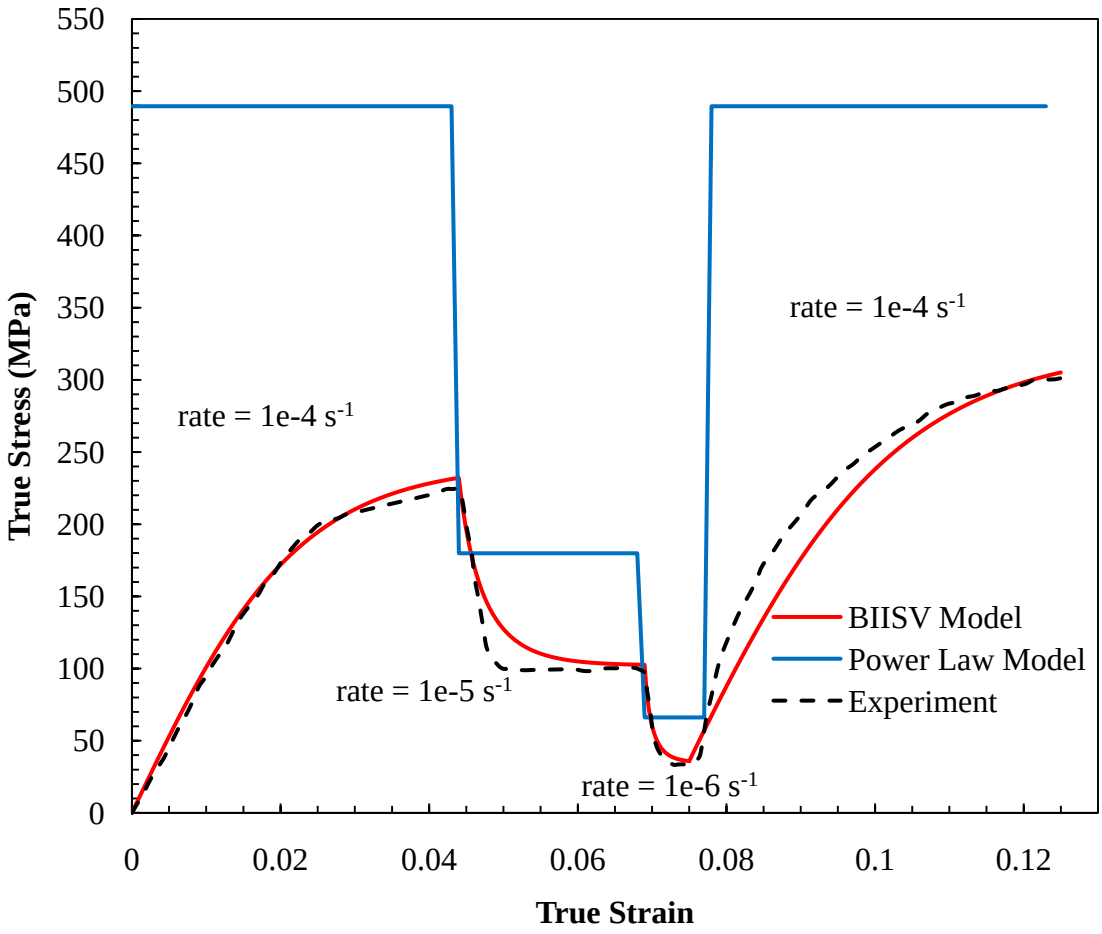

Figure 3.4 Comparison of BIISV model and power law model to Lherzolite experimental data (Carter and Ave'Lallemant, 1970) for a varying strain rate history at 1333K.

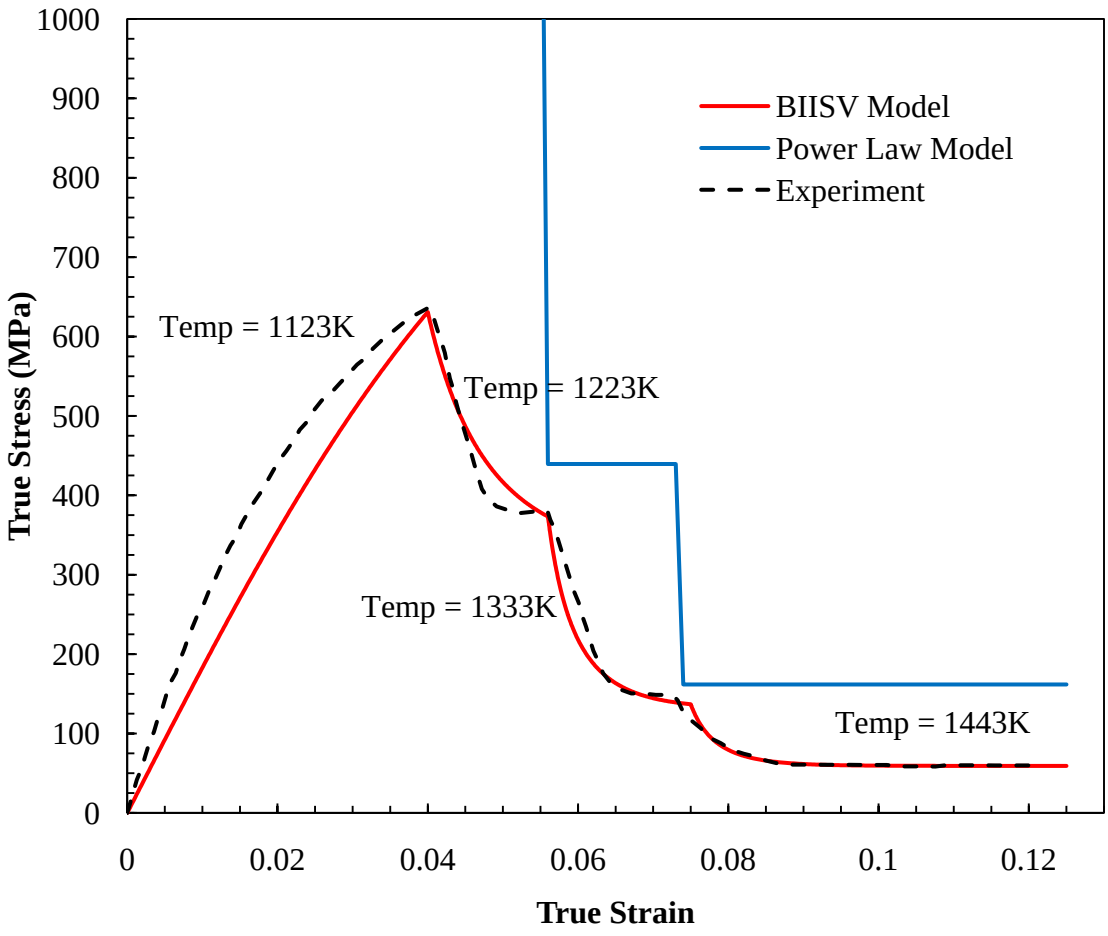

Figure 3.5 Comparison of BIISV model and power law model to Lherzolite experimental data (Carter and Ave'Lallemant, 1970) for a varying temperature history at 7.8e-5 s^{-1}.

Two simulations were performed to highlight the differences between the BIISV model and the power law model. The first was identical to the previous simulations but with the different material constants. The second had a constant temperature of 3000 K at the bottom boundary, which allowed a vertical heat flux. This more closely resembles the Earth's mantle temperature distribution and will serve as another way to compare the BIISV model and the power law model. The initial temperature distributions for these

simulations are shown in Figure 3.6. The results of these simulations will be presented in the following section.

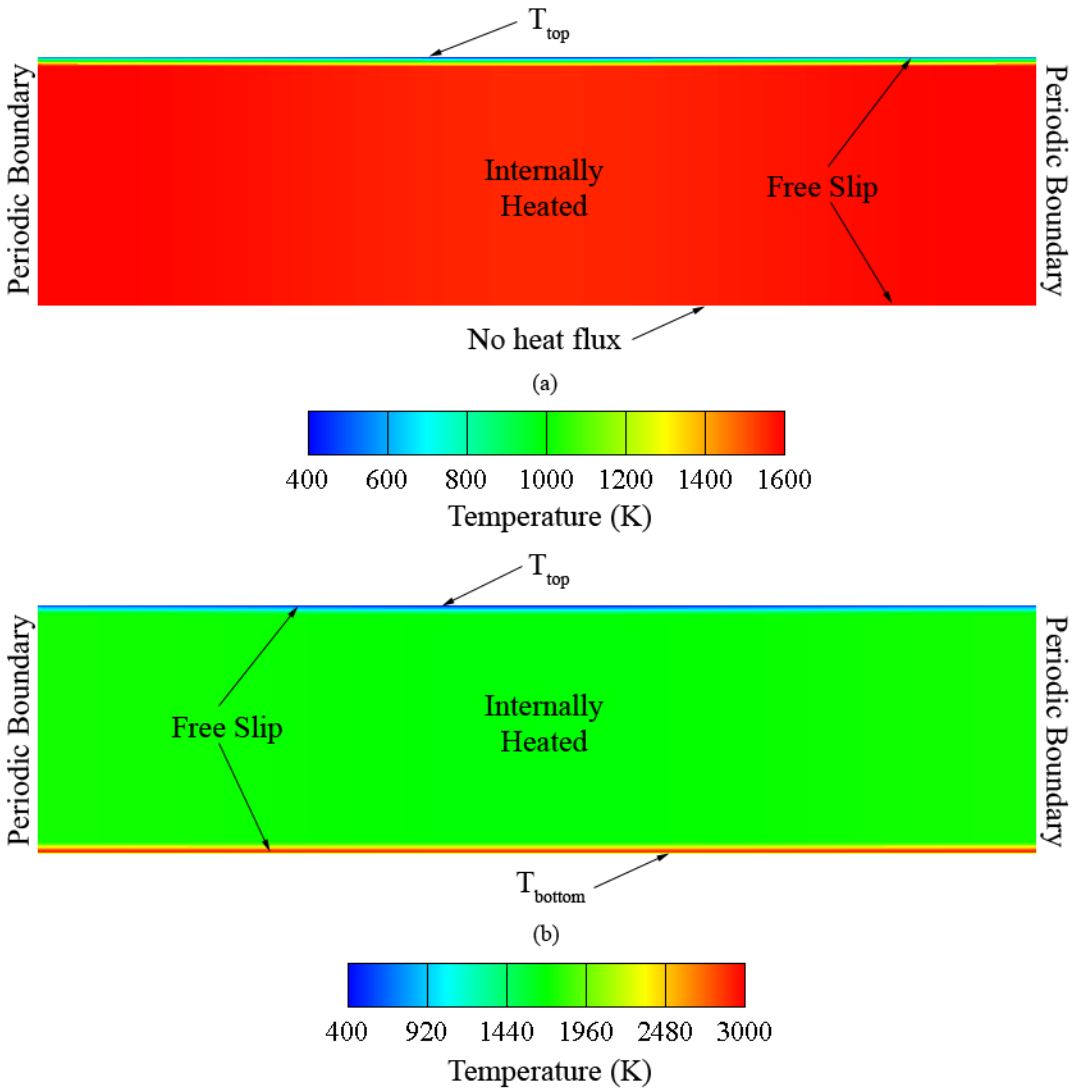

Figure 3.6 Initial temperature fields for the lherzolite simulations. Plot (a) shows the temperatures for the case of internal heating with no basal heating. Plot (b) shows the initial temperatures for the case that includes both internal and basal heating.

Results

The simulations regarding the power law and BIISV model comparison reveal some very interesting differences. The initial temperature distribution given by Equations (3.5) and (3.6) with the internal heating leads to a single avalanche in the middle of the domain near the beginning of the simulation. Figure 3.7 shows the viscosity contours at the end of the first time step, which is well before the first avalanche to show their similarities. Figure 3.8 shows the BIISV case during the first avalanche. Before the material plunges to the bottom of the domain, the cold thermal boundary layer grows in thickness. The gravitational potential energy accumulates until the cold dense material plunges downward. The material begins to sink in the middle of the domain, because of the initial temperature distribution given by Equation (3.6). Both the BIISV and the power law cases behave this way and look almost identical.

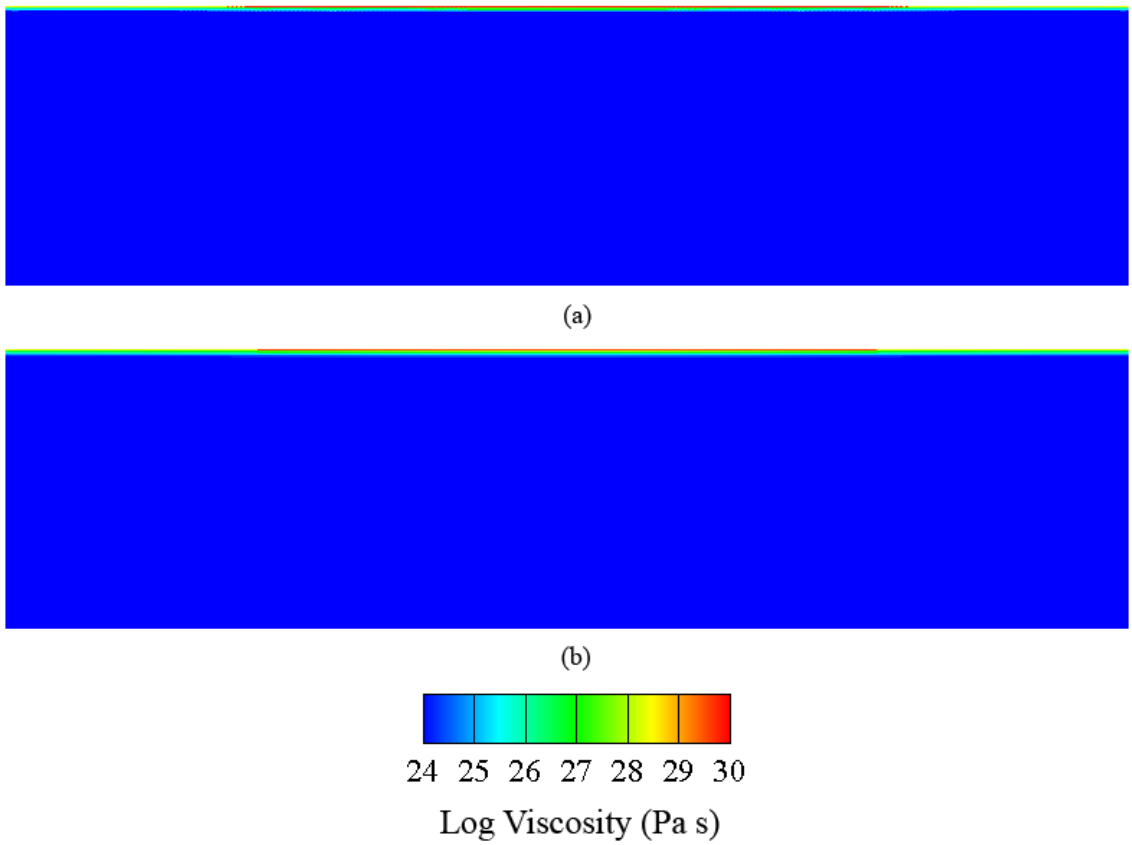

Figure 3.7 Viscosity contour plot for both a) power law model and b) BIISV model at the end of the first time step.

A more interesting comparison is the second set of avalanches that occur after the initial avalanche. After most of the cold surface material in the initial boundary layer has been removed by the first avalanche, cooling at the boundary causes a cold layer to redevelop on either side of the initial avalanche. The temperature distribution before the second set of avalanches is shown in Figure 3.9. The two models should be expected to deviate from each other based on the differences in the mathematical forms as indicated by Figure 3.1. The second set of avalanches occurred at somewhat different locations along the top boundary, but the resulting flow patterns are remarkably similar. The lateral extent of the two patches of cold thermal boundary layer in Figure 3.9 were

different for the two cases. The power law case had less lateral extent than the BIISV model, but both cases eventually produced instabilities that caused the thermal layer to plunge downward. Figure 3.10 shows the point when the material reached the bottom of the domain, for the power law at 4.5 Mya and BIISV model at 7.5 Mya.

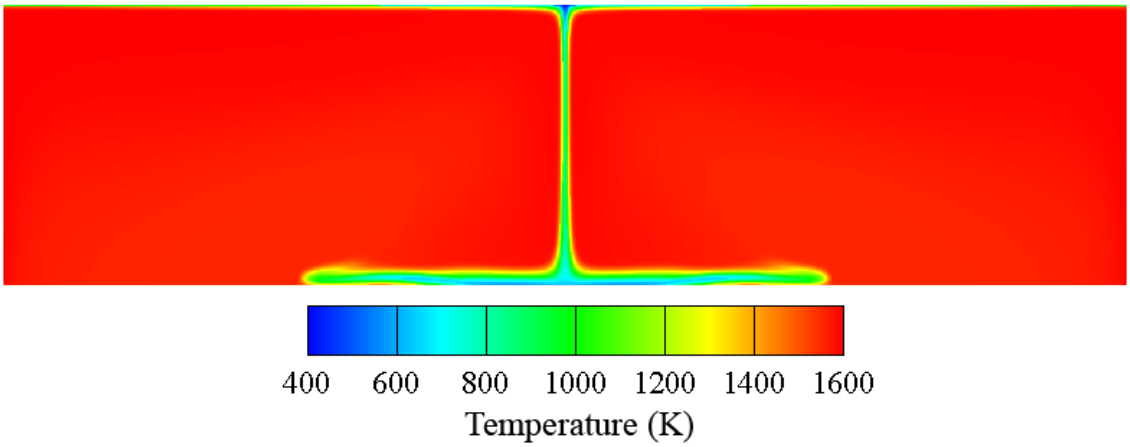

Figure 3.8 The first avalanche from case with internal heating only.

The results are similar in structure at the point when the material reached the domain bottom in the convection calculation, but some slight differences are apparent. One is the horizontal surface velocity as displayed in Figure 3.11. The peak amplitudes of the surface velocities are similar but the velocity profiles are somewhat different. The two solutions after this point differ more and more in their details, but the overall episodic behavior remains qualitatively similar. The relatively close match between the power law and BIISV simulations during the first two avalanches confirms that the BIISV model is working as anticipated.

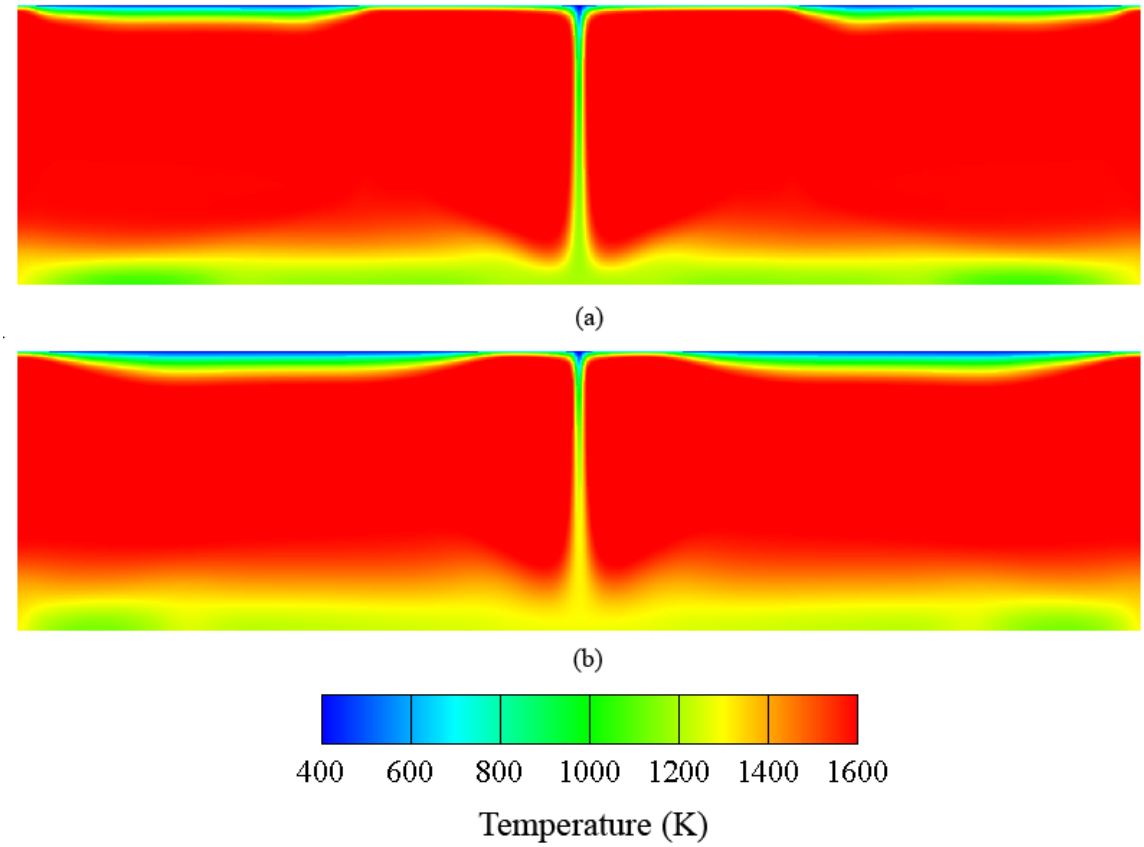

Figure 3.9 The temperature field for the a) power law model and the b) BIISV model at the time just before the second set of avalanches occurs.

We next examined the second BIISV fit to the power-law model which leads to a viscoplastic flow law. Because history dependence can play a vital role in flow dynamics, we expected to see some difference in behavior relative to the first BIISV fit that gave a perfectly plastic rheology with no history dependence.. The BIISV constants that yield the viscoplastic behavior are shown in Table 3.3. Figure 3.12 shows the resulting simulation after the second set of avalanches have plunged to the bottom of the domain. The temperature field in Figure 3.12b shows some similarity to the one in Figure 3.10b, but differences are clear. The avalanche locations have all shifted to the left. In Figure 3.12a the isotropic hardening variable is shown to illustrate how the hardened material

moved left of the original avalanche location. Some hardened material is even observed at the bottom of the domain. Based on Equation (3.25) and the constants given in Table 3.3, hardening is localized in the cold thermal layer where the temperature is below 1000 K.. Any material over 1000 K for these constants does not harden but instead behaves like a perfectly plastic material. The hardened material left on the upper surface acts like a road block for the unhardened cold material. As the simulation proceeds unhardened cold material is diverted downward as it comes in contact with the hardened material. This effect does not occur in the previous simulations, because the material's deformational history is not taken into account.

Figure 3.13b shows the strain rates involved at this same moment in the simulation. Notice the strain rates in Figure 3.13b are within the expected correlated range. Figure 3.13a shows the plastic strain calculated by Equation (3.46), which is a good measurement of the amount of deformation the material has experienced. The horizontal surface velocity for the viscoplastic case is compared to the perfectly plastic case in Figure 3.14. The relative amplitudes of the surface velocities are similar, which is expected due to both set of constants are trying to model the same material. The center avalanche remnant of the viscoplastic case displays slightly higher velocity than the perfectly plastic case because of the diverting effect described earlier. This shows that the hardened slow moving material can actually increase the flow around it and cause an accelerating effect on the avalanching material. This viscoplastic example shows the power and importance of including material history as part of the flow calculation. As a side note, we also explored a large range of initial isotropic hardening values. These did not change the answer by any appreciable degree.

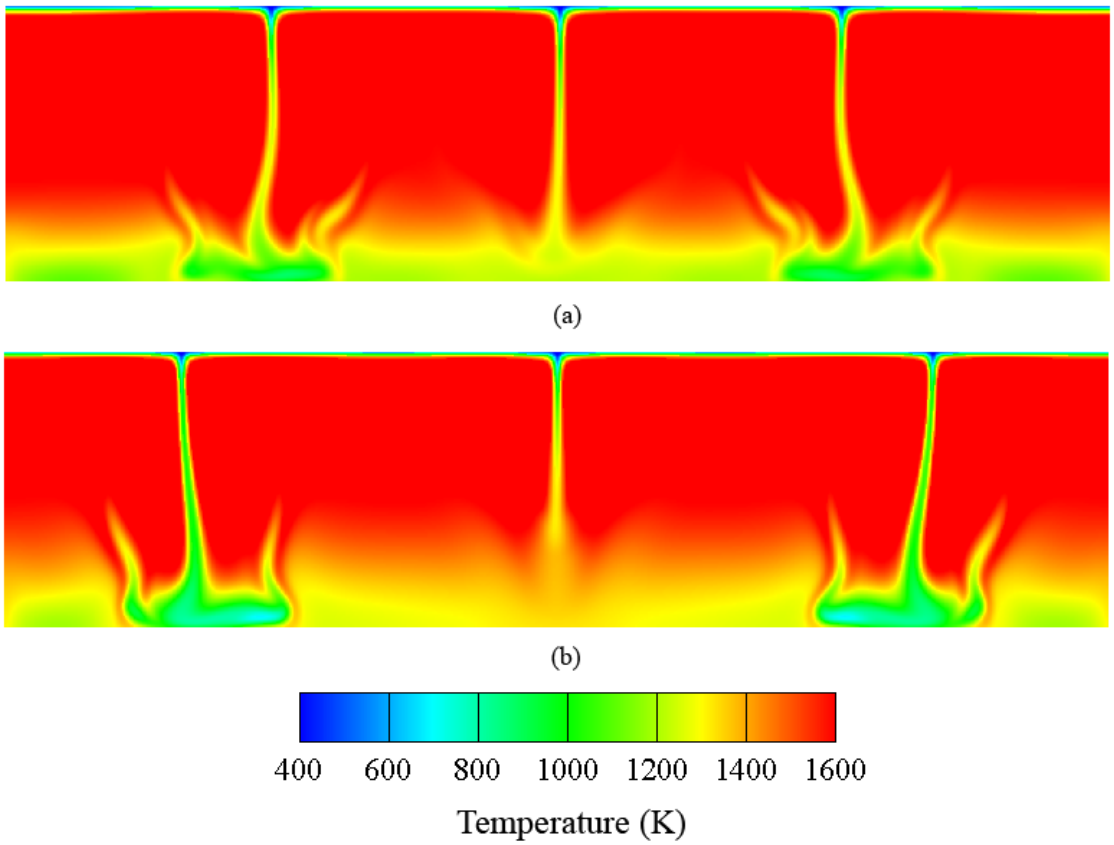

Figure 3.10 Temperature fields after the second set of avalanches in the a) power law model and the b) BIISV model.

We next describe two simulations that utilize the experimental data for lherzolite from Carter and Ave'Lallemant (1970). Figure 3.15 shows three time snapshots from the power law model using their constants for a case with only internal heating. Figure 3.16 shows the simulation using the BIISV constants fitted to the Carter and Ave'Lallemant (1970) experimental data. Both simulations have similar characteristics with one main difference in the flow pattern. Much like the previously discussed viscoplastic case, the current BIISV simulation has the history dependence. The isotropic hardening at the same times as Figure 3.16 is shown in Figure 3.17. The hardened material in the cold thermal boundary again acts a diverter to allow the material to flow around it. The power

law simulation shown in Figure 3.15 does not show this same behavior. The residual avalanches in the power law case continue to slow down and die and do not persist as in the BIISV case. Figure 3.18 shows a velocity magnitude plot illustrating this point. The cold material in the BIISV case continues to flow around and below the hardened material, while in the power law case new avalanches arise to remove the accumulation of cold gravitationally unstable surface material. The avalanche locations in the BIISV case tend to persist throughout the calculation.

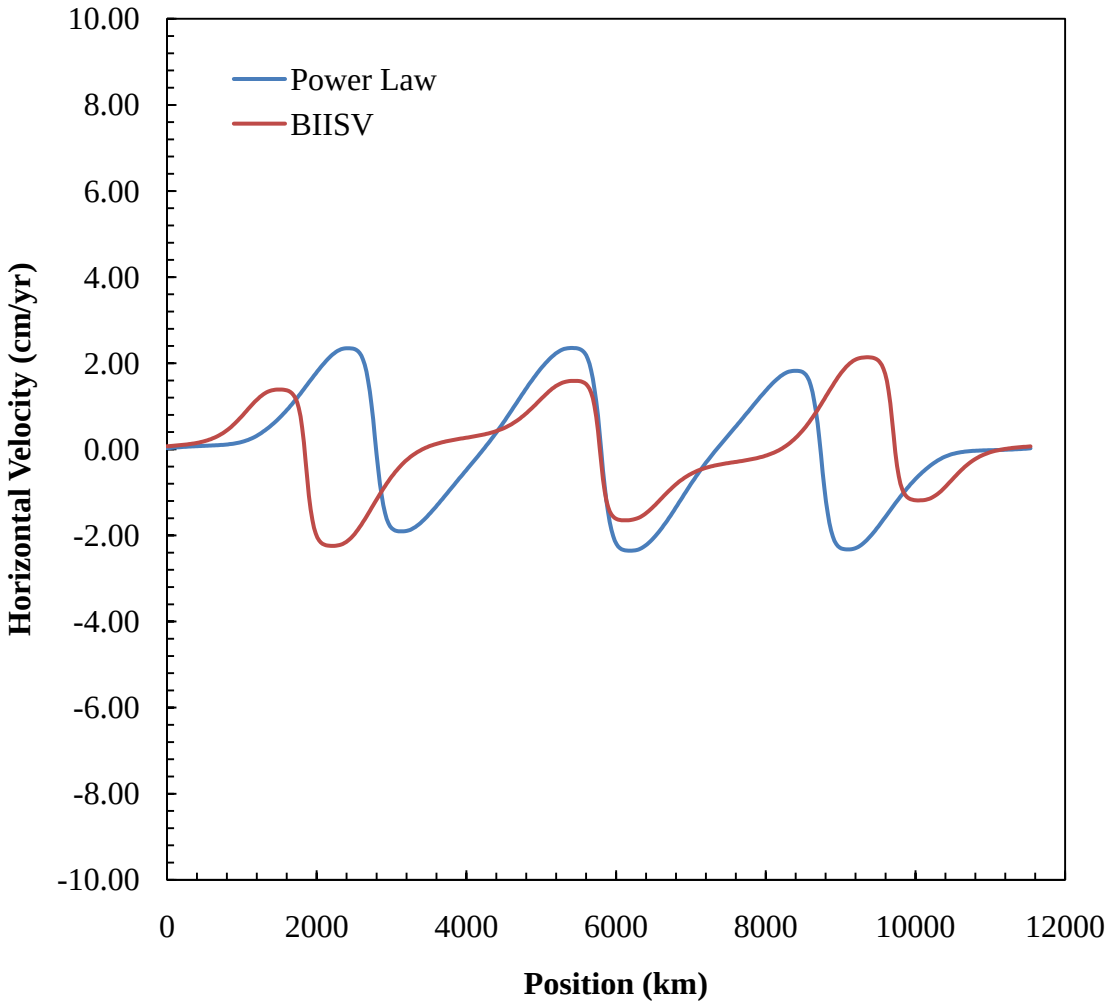

Figure 3.11 Horizontal surface velocity of both the power law model and BIISV model during the second set of avalanches.

The simulations where the domain is both internally and basally heated display somewhat different dynamics. As the first avalanche occurs, a hot plume also rises to the surface from the hot basal layer as shown in Figure 3.19a for the power law case and Figure 3.20a for the BIISV case. Smaller hot plumes also emerge throughout the simulation, bringing hot material to the surface. A significant distinction between the two models may be observed by comparing Figure 3.19b and Figure 3.20b. The key difference in the ability of the BIISV model to include hardening. In the BIISV case shown in Figure 3.20, a second large avalanche of cold material occurs in the center of the domain due to the diverting effect discussed earlier. Figure 3.21a shows the corresponding isotropic hardening field for the first avalanche, and Figure 3.21b shows the hardened material at the time of the second avalanches. Figure 3.20c shows a third avalanche appearing. In this case the hardened material in the cold boundary layer does not disappear, but, as also seen in Figure 3.17, the hardened material tends to persist and influence subsequent flow. Power law models without history simply cannot represent these long-lasting effects of material hardening. These results suggest that history effects may well be very important in understanding the cold upper thermal boundary layer's interaction with the rest of the mantle.

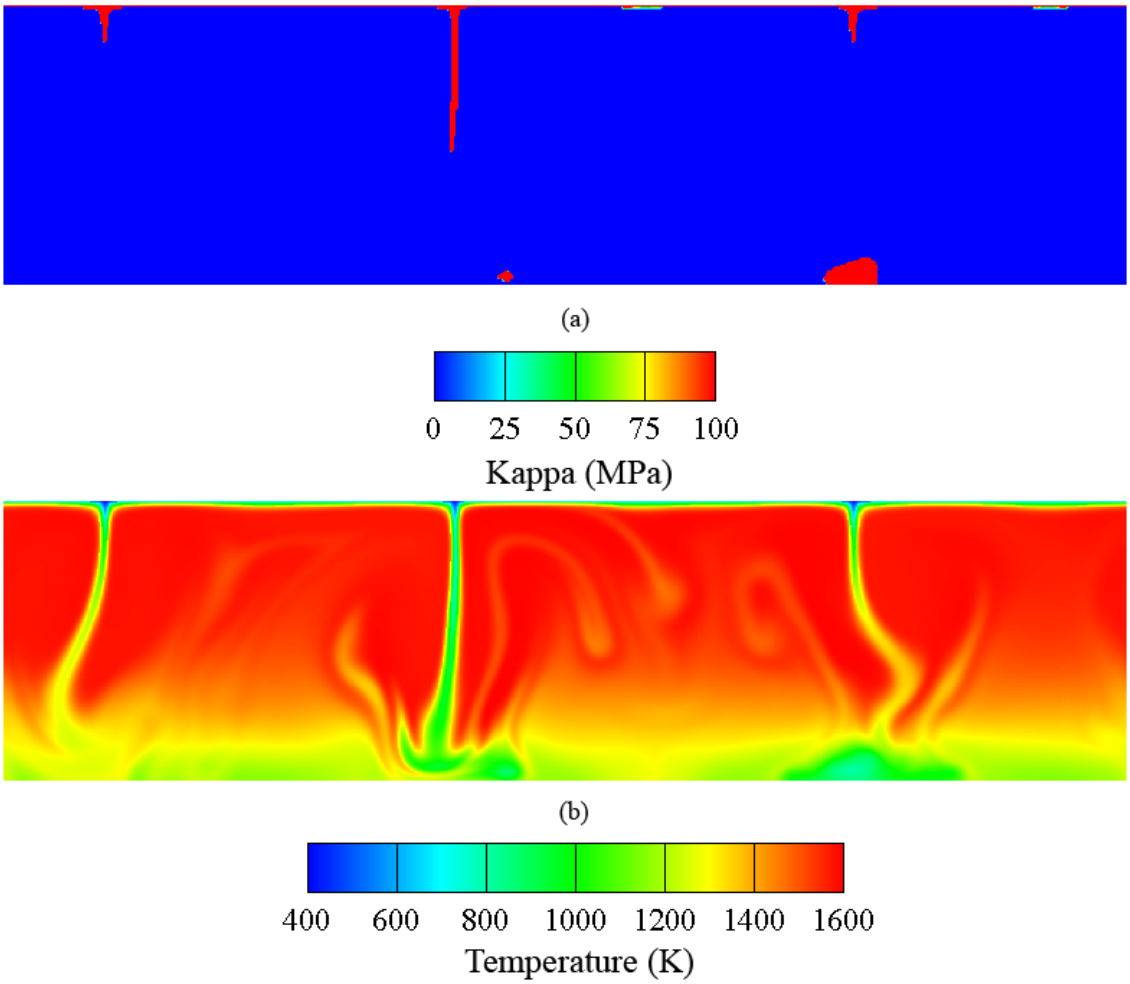

Figure 3.12 Viscoplastic BIISV test simulation with the a) isotropic history variable and the b) temperature field at the end of the second set of avalanches indicating that hardened material persists and influences the subsequent flow pattern.

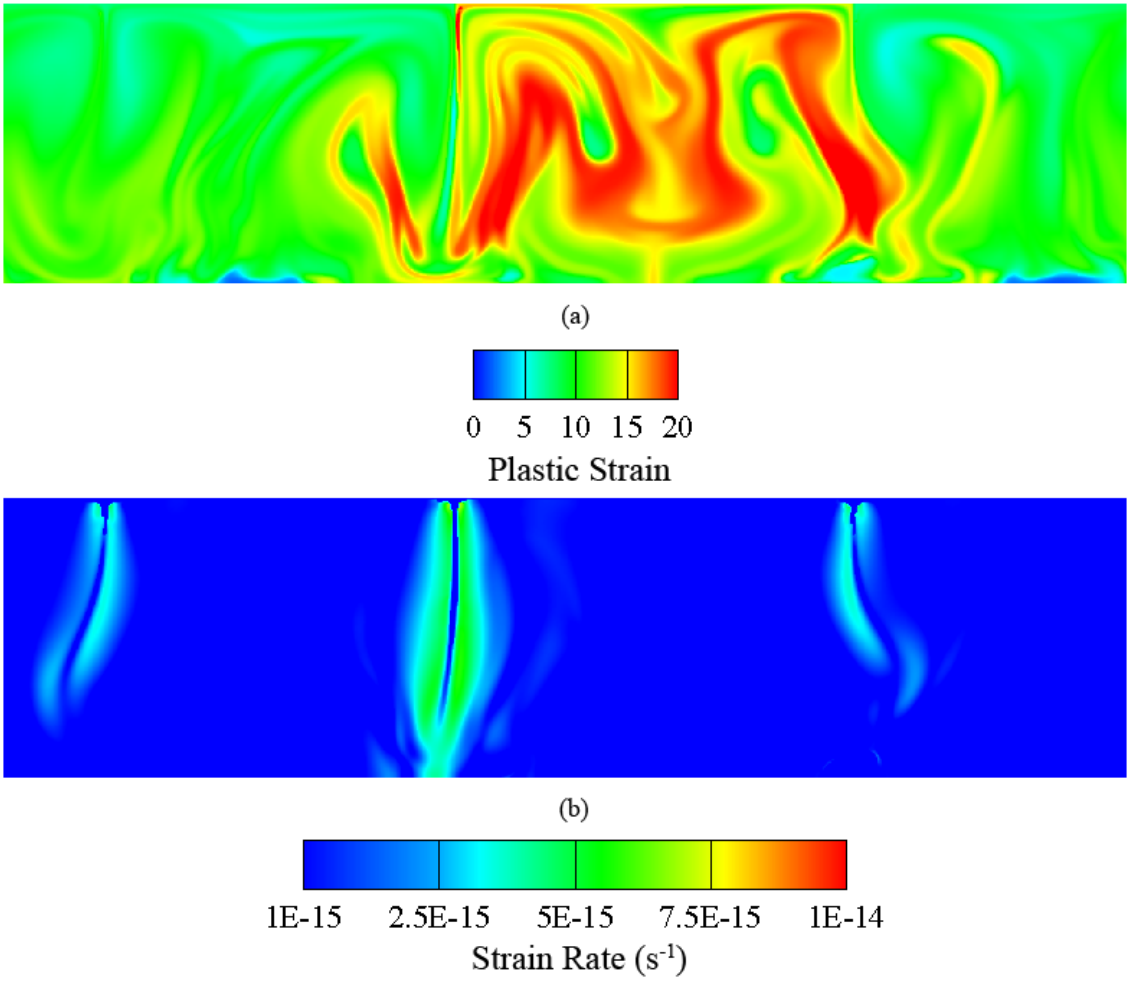

Figure 3.13 Contours of a) plastic strain and b) strain rate for the viscoplastic BIISV test simulation. Note the enormous plastic strains in the earth's mantle (up to 2000%).

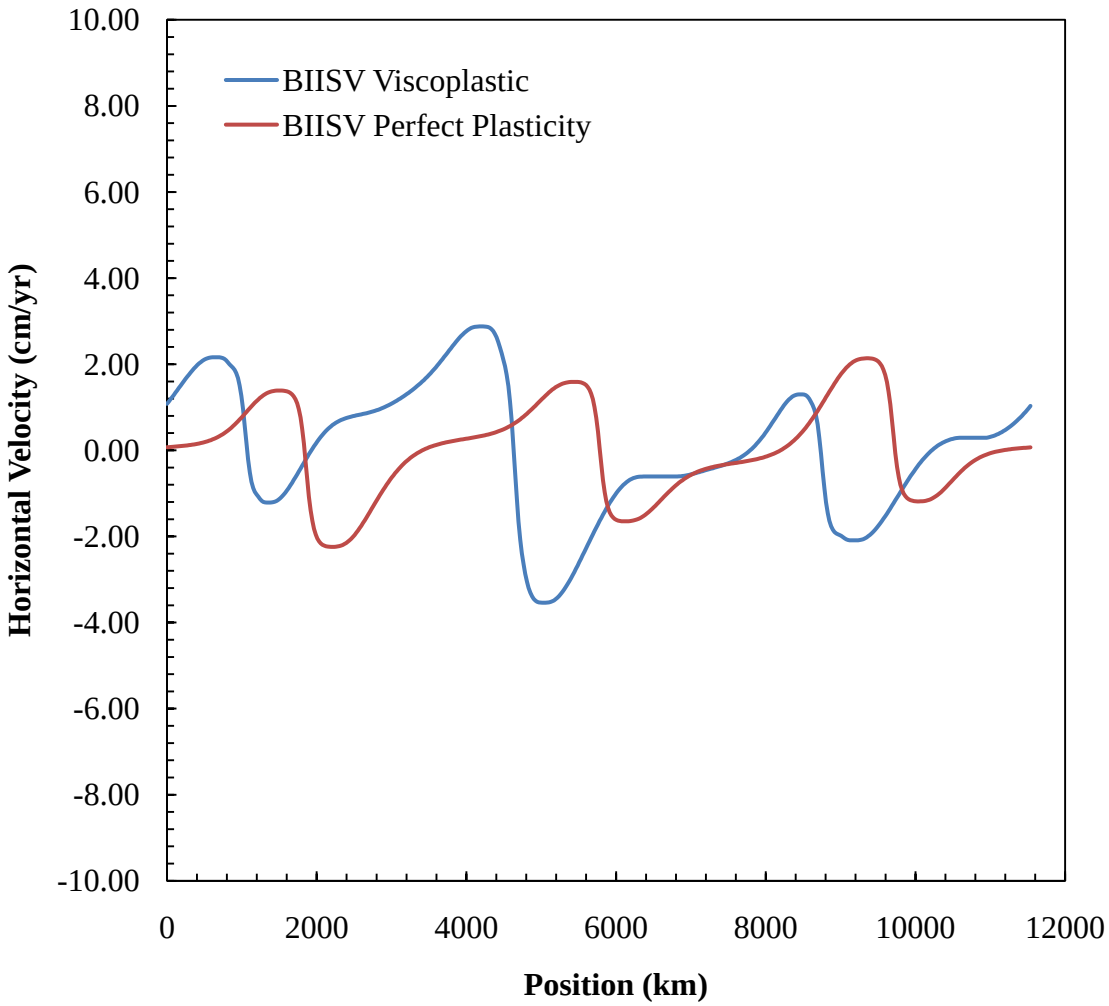

Figure 3.14 Comparison of horizontal surface velocities for the BIISV viscoplastic and BIISV perfectly plastic cases.

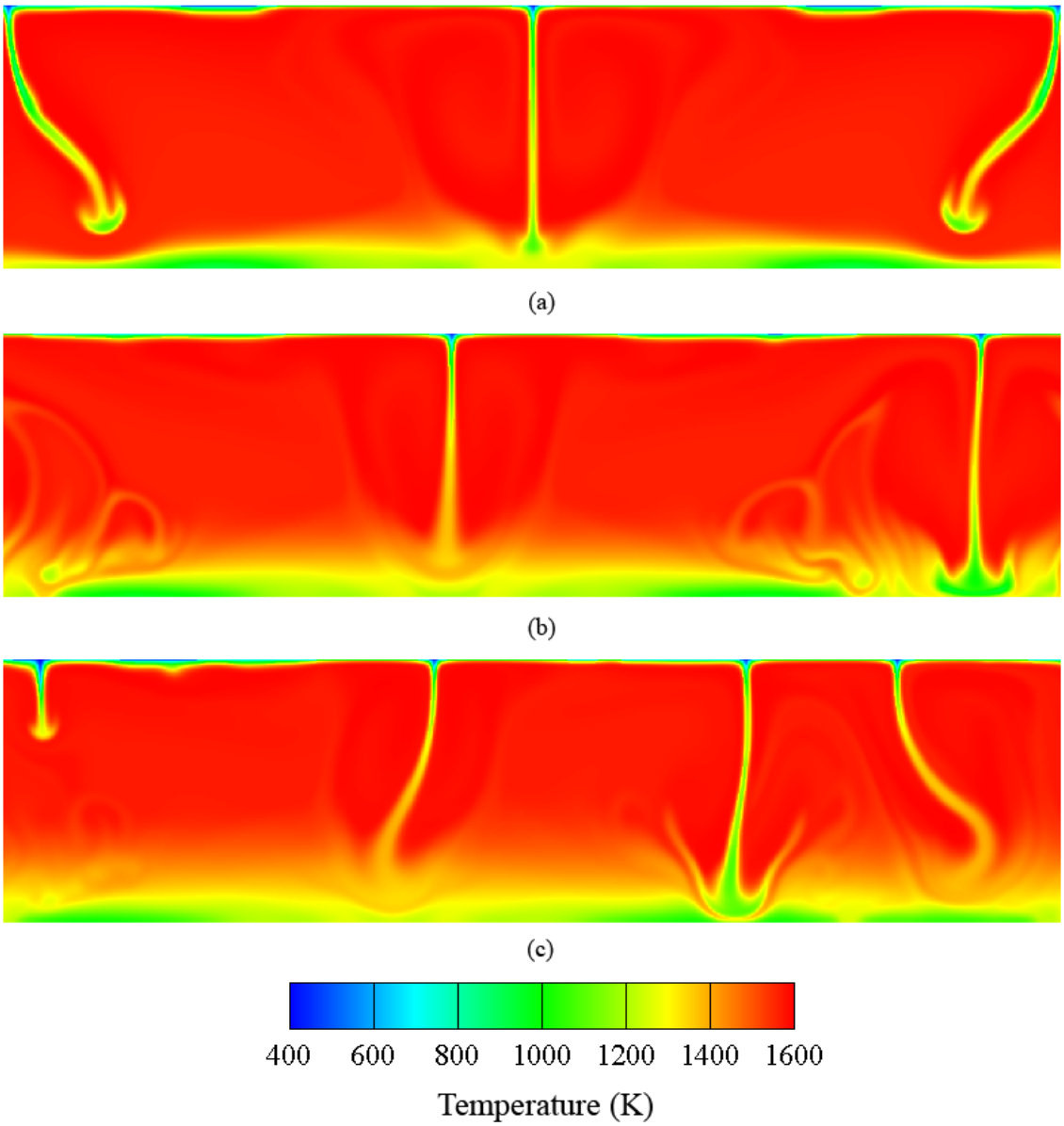

Figure 3.15 Temperature fields for a case with internal heating only using the power law model constants for lherzolite. Snapshots in time at a) 135 Myr, b) 170 Myr, and c) 220 Myr.

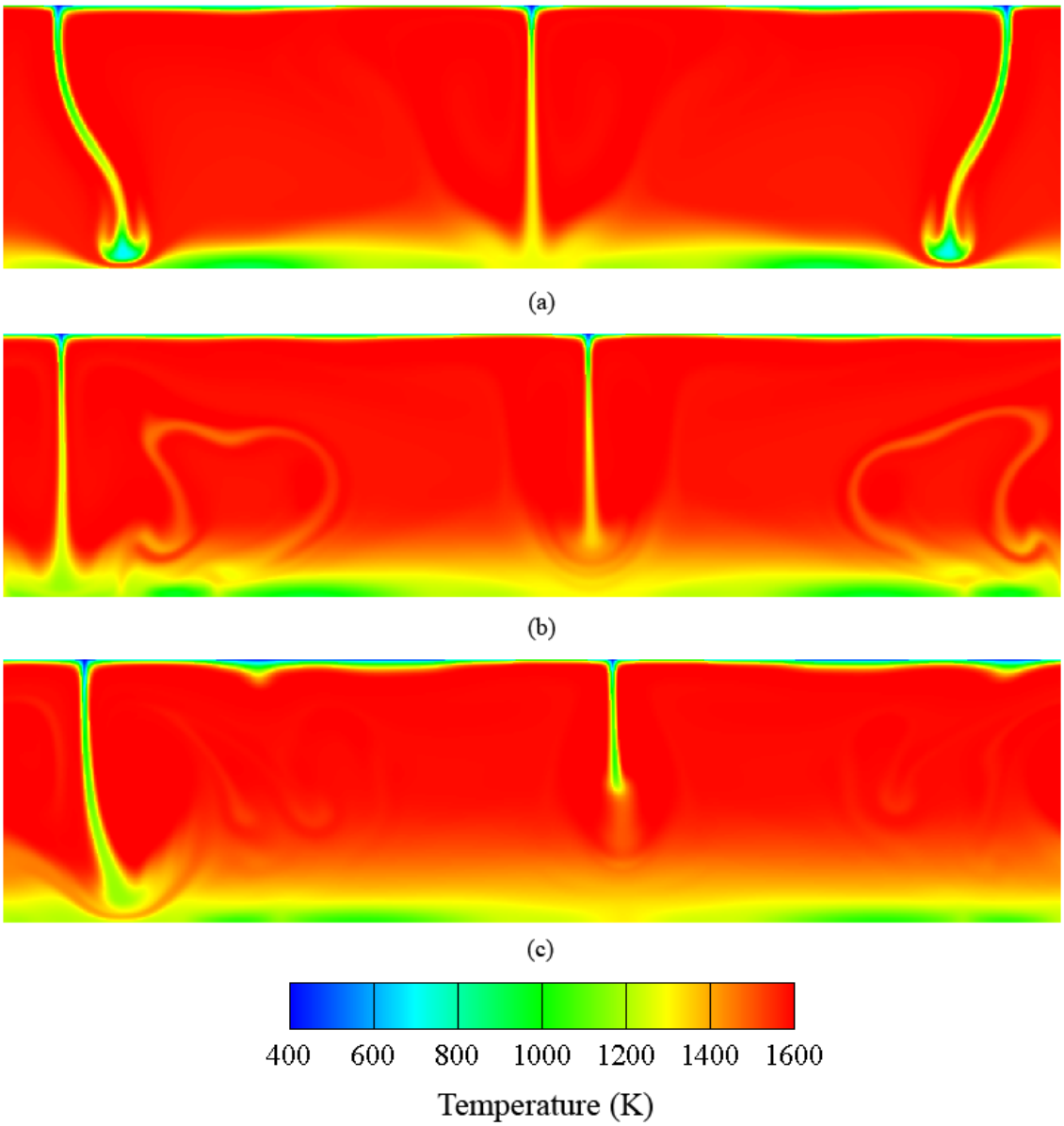

Figure 3.16 Temperature fields for a case with internal heating only using the BIISV viscoplastic model for lherzolite. Snapshots in time at a) 150 Myr, b) 200 Myr, and c) 280 Myr.

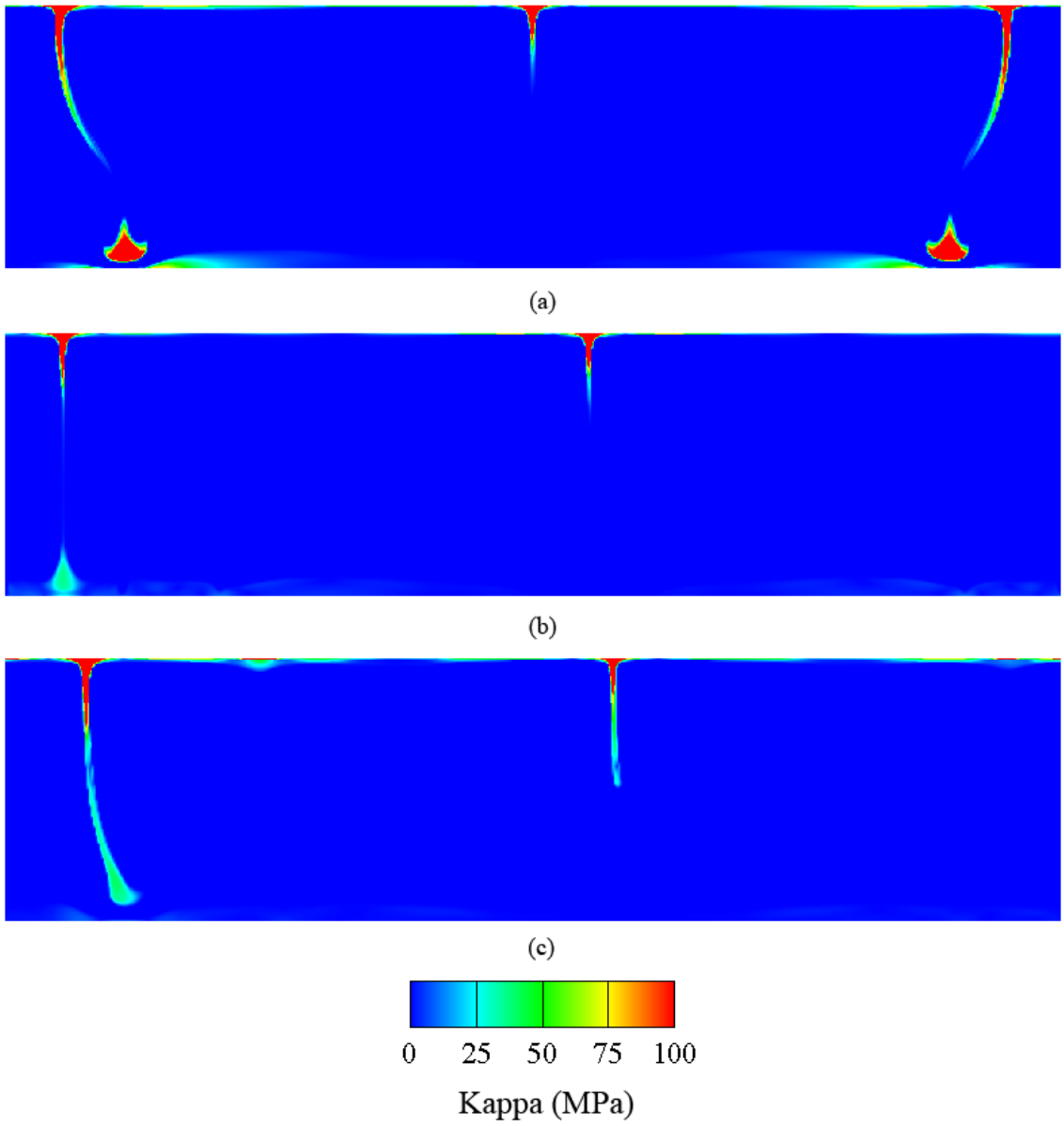

Figure 3.17 Isotropic hardening fields for case shown in Figure 3.16 using the BIISV viscoplastic model for lherzolite. Snapshots in time at a) 150 Myr, b) 200 Myr, and c) 280 Myr.

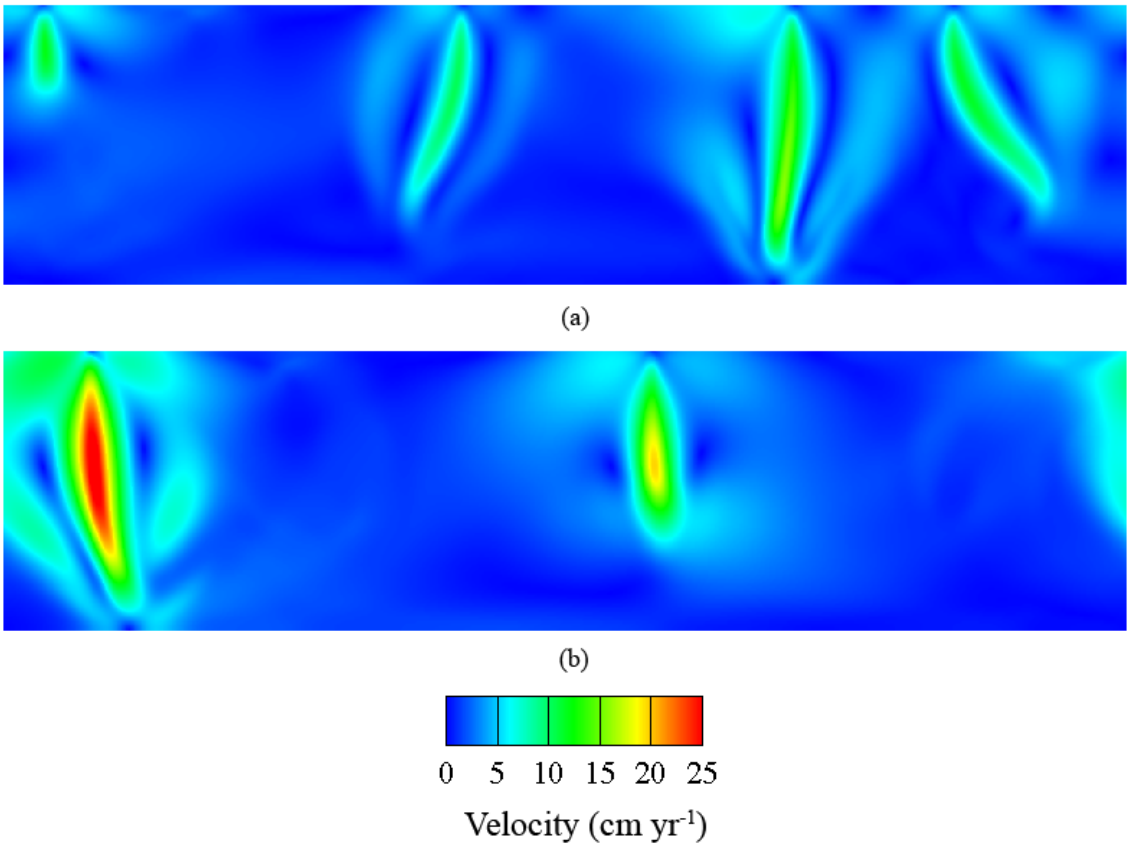

Figure 3.18 Velocity magnitude contours for a) power law model at 220 Myr and b) BIISV viscoplastic model at 280 Myr.

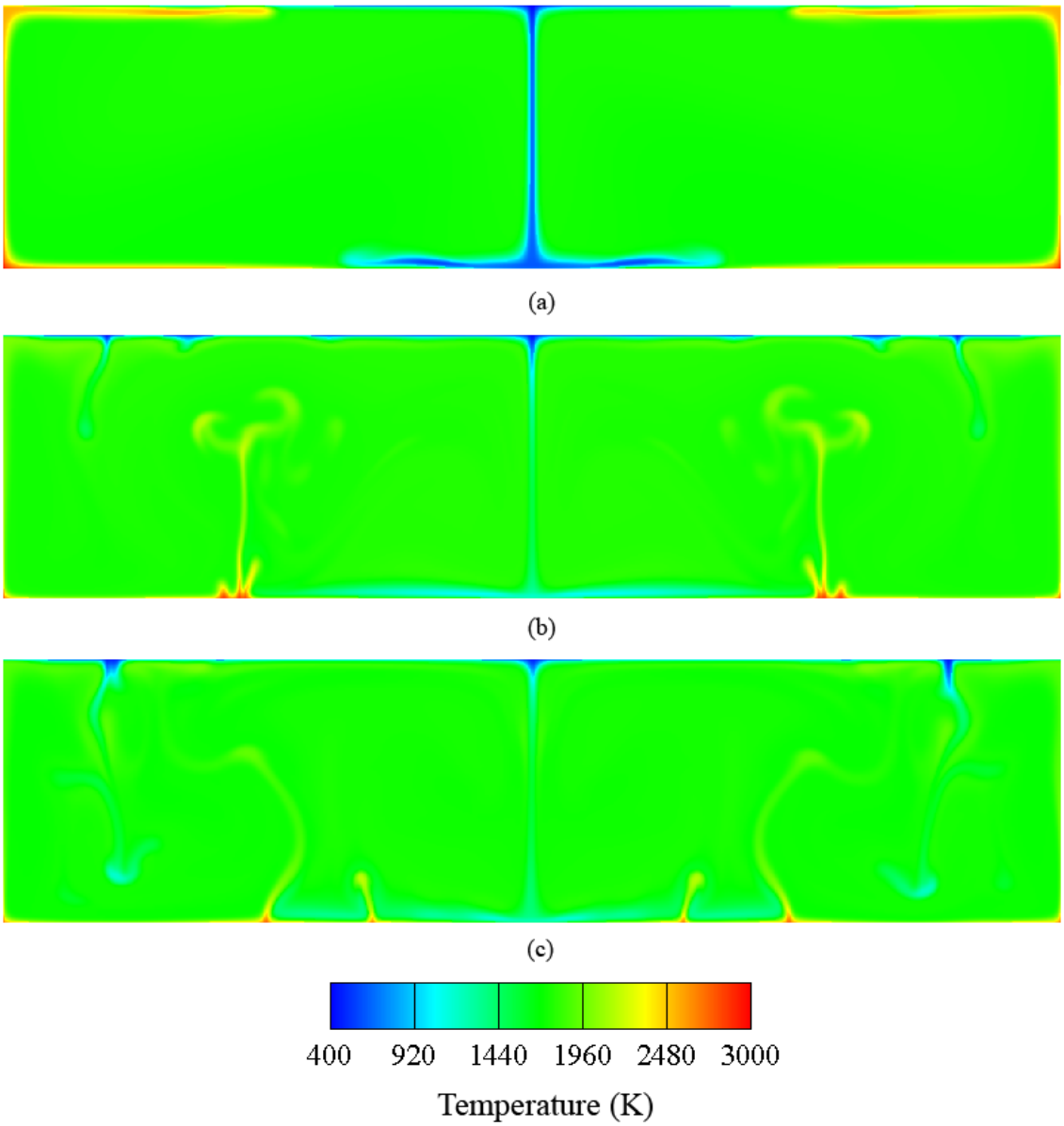

Figure 3.19 Temperature fields for the internally heated and basally heated simulation using the power law model constants for lherzolite. Snapshots in time at a) 15 Myr, b) 150 Myr, and c) 220 Myr.

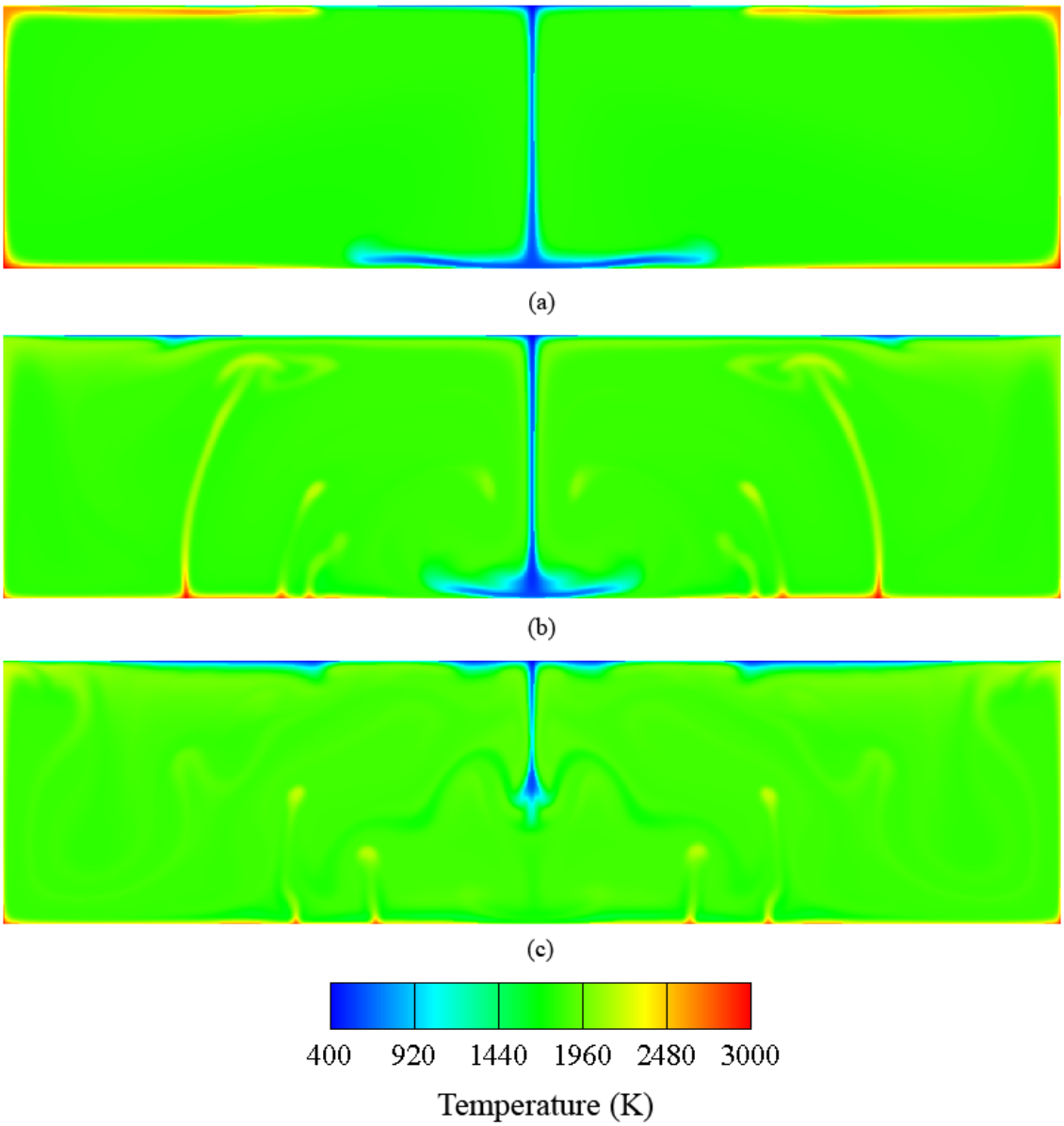

Figure 3.20 Temperature fields for the internally heated and basally heated simulation using the BIISV viscoplastic model constants for lherzolite. Snapshots in time at a) 17 Myr, b) 175 Myr, and c) 280 Myr.

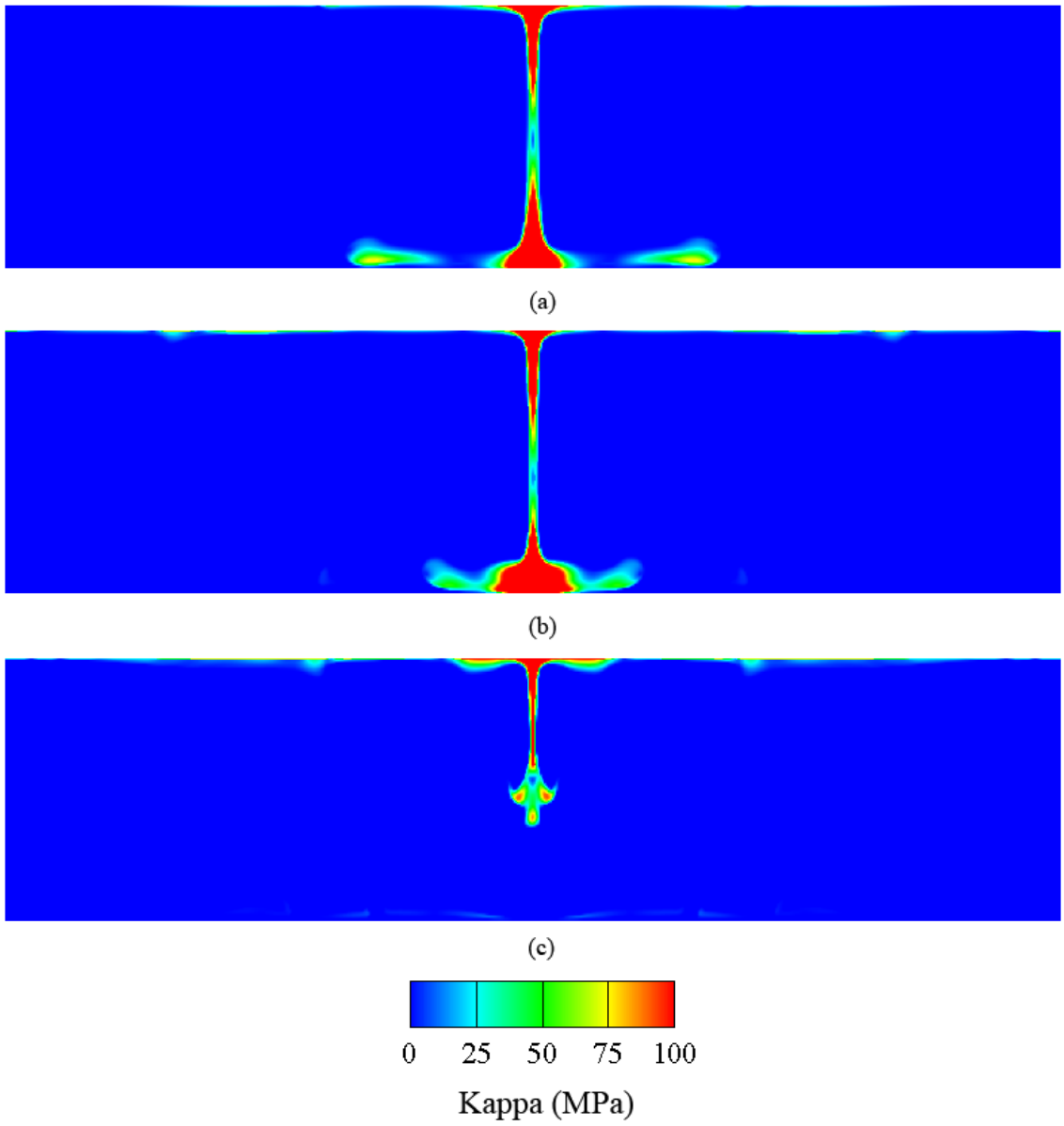

Figure 3.21 Isotropic hardening fields for the internally heated and basally heated simulation using the BIISV model constants for lherzolite. Snapshots in time at a) 17 Myr, b) 175 Myr, and c) 280 Myr.

Discussion and Conclusions

The simulations undertaken in this study illuminate a need to include a material's deformational history in modeling mantle dynamics. The utility of the BIISV model was

illustrated through its ability to capture one aspect of deformation history using only one of its internal state variables. The analysis also suggests that the steady state assumption implicit within the power law model should be called into question even for the large time scales involved in the mantle convection simulations. The simulations do not give a full picture of the relationship between the influence of deformational history and mantle convection, but this study calls attention to its importance. One noteworthy result from these calculations is that the persistence of zones of work hardened rock in the earth's upper mantle may well lead to increased persistence of where subduction takes place. This might possibly shed some new light on the mechanism responsible for the long lived weak zones that influence plate tectonics described by Gurnis *et al.* (2000).

For the BIISV model to have practical value, a crucial prerequisite is experimental work from which a reliable set of BIISV material constants can be obtained for relevant mineral phases and rock types. Even extending existing data over a larger range of temperatures and strain rates would be helpful. A more complete set of experimental stress-strain curves will obviously improve the realism of the simulations. The simple cases conducted in this study were to illustrate the capability of the BIISV model to capture phenomena that the widely used power law models simply cannot capture. With the BIISV model now in place many important features like recrystallization, grain size effects, and texture development could easily be added. Damage as has been explored by Tackley (1998) and Auth *et al.* (2003) could also be added to allow for failure without the need for the viscous yield limit which was used in this study. Including history variables in the rheological model opens the door to realism far beyond anything that has been realized in the past. Certainly implementing the BIISV

model in three dimensions to examine in 3D some of the new effects we discover in 2D is an exciting prospect. Based on the many phenomena this history variable approach has elucidated in the realm of metals in the engineering world, we are confident that it has the potential to lead to equally exciting new insights in the realm of the solid earth and its dynamics.

References

Aubertin, M., Gill, D.E. & Ladanyi B., 1991. An internal variable model for the creep of rocksalt, *Rock Mechanics and Rock Engineering*, **24**, 81-97.

Aubertin, M., Gill, D.E. & Ladanyi, B., 1991. A unified viscoplastic model for the inelastic flow of alkali Halides, *Mech. of Matls.*, **11**, 63-82.

Auth, C., Bercovici, D. & Christensen U.R., 2003. Two-dimensional convection with a self-lubricating, simple-damage rheology, *Geophys. J. Int.*, **154**, 783-800.

Bammann, D.J., 1990. Modeling temperature and strain rate dependent large deformations of metals. *Appl. Mech. Rev.*, **1**, 312-318.

Bammann, D. J. & Aifantis, E.C., 1987. A Model for Finite Deformation Plasticity, *Acta Mechanica*, **69**, 97-117.

Bammann, D.J., Chiesa, M.L., Horstemeyer, M.F. & Weingarten, L.I., 1993. Failure in ductile materials using finite element methods, in *Structural Crashworthiness and Failure*, eds. Jones, N. & Weirzbicki, T., Elsevier Applied Science.

Bammann, D. J. & Johnson, G.C., 1987. On the Kinematics of Finite-Deformation Plasticity, *Acta Mechanica*, **70**, 1-13.

Baumgardner, J. R., 1983. A Three-Dimensional Finite Element Model for Mantle Convection, Ph.D. Thesis, 271 pp., UCLA.

Baumgardner, J. R., 1985. Three-dimensional treatment of convective flow in the Earth's mantle, *J. Stat. Phys.*, **39**, 501-511.

Carter, N.L. & Ave'Lallemant, H.G., 1970. High temperature flow of dunite and perodidite, *Geol. Soc. Am. Bull.*, **81**, 2181-2202.

Chopra, P.N. & Paterson, M.S., 1981. The experimental deformation of dunite, *Tectonophysics*, **78**, 453-473.

Chopra, P.N. & Paterson, M.S., 1984. The role of water in the deformation of dunite, *J. Geophy. Res.*, **89**, B9, 7861-7876.

Christensen, U. R., 1984. Convection with pressure- and temperature-dependent non-Newtonian rheology, *Geophys. J. Roy. Astron. Soc.*, **77**, 343-384.

Christensen, U. R., 1989. The heat transport by convection rolls with free boundaries at high Rayleigh number, *Geophys. Astrophys. Fluid Dyn.*, **46**, 93-103.

Covey-Crump, S.J., 1994. The Application of Hart's state variable description of inelastic deformation to Carrara Marble at T<450C, *J. Geophys. Res*., **99**, B10, 19793-19808.

Daly, S. F., 1980. The vagaries of variable viscosity convection, *Geophys. Res. Lett.*, **7**, 841-844.

Goetze, C., 1978. The mechanisms of creep in olivine, *Phil. Trans. R. Soc. Lond*., **288**, A, 99-119.

Gurnis, M., Zhong, S. & Toth, J., 2000. On the competing roles of fault reactivation and brittle failure in generating plate tectonics from mantle convection, in *History and Dynamics of Global Plate Motions*, eds. Richards, M.A., Gordon, R., & van der Hilst, R., *Geophysics Monograph Series*, vol. 121, pp. 73-94, AGU, Washington, DC.

Hansen, U., Yuen, D.A. & Kroening, S.E., 1990. Transition to hear turbulence in thermal convection at infinite Prandtl number, *Phys. Fluids A*, **2**, 2157-2163.

Hart, E.W., 1970. A phenomenological theory for plastic deformation of polycrystalline metals, *Acta Metall*., **18**, 599-610.

Hart, E.W., 1976. Constitutive relations for the nonelastic deformation of metals, *J. Enger. Mater. Tech*., **98**, 193-202.

Hewitt, J.M., McKenzie, D.P. & Weiss, N.O., 1980. Large aspect ratio cells in two-dimensional thermal convection, *Earth Planet. Sci. Lett.*, **51**, 370-380.

Houston, M. H. & De Bremaecker, J.-C., 1975. Numerical models of convection in the upper mantle, *J. Geophys. Res.*, **80**, 742-751.

Jacoby, W. R. & Schmelling, H., 1982. On the effects of the lithosphere on mantle convection and evolution, *Phys. Earth Planet. Int.*, **29**, 305-319.

Jarvis, G.T., 1984. Time-dependent convection in the Earth's mantle, *Phys. Earth Planet. Int.*, **36**, 305-327.

Karato, S., 2008. *Deformation of Earth Materials*, Cambridge Univ. Press, UK. pp. 463.

Karato, S.I. & Toriumi, M., 1989. *Rheology of Solids and of the Earth*, Oxford Science Publications, Oxford.

Khan, A. S. & Huang, S., 1995. *Continuum Theory of Plasticity*, John Wiley & Sons, Inc., New York.

Kirby, S.H., 1983. Rheology of the lithosphere, *Reviews Geophys. Space Phys*., **21**, 1458-1487.

Krieg, R.D. & Krieg, D.B., 1977. Accuracies of numerical solution methods for the elastic-perfectly plastic model, *ASME J. Pressure Vessel Technol.*, **99**, 510-515.

McKenzie, D., Roberts, J. & Weiss, N., 1973. Numerical models of convection in the Earth's mantle, *Tectonophysics,* **19**, 89-103.

McKenzie, D.P., Roberts, J.M. & Weiss, N.O., 1974. Convection in the Earth's mantle: Towards a numerical simulation, *J. Fluid Mech*, 62, 465-538.

Moresi, L. & Solomatov, V., 1995. Numerical investigation of 2D convection with extremely large viscosity variations, *Phys. Fluids,* **7**, 2154-2162.

Olson, P., 1987. A comparison of heat transfer laws for mantle convection at very high Rayleigh numbers, *Phys. Earth Planet. Int.*, **48**, 153-160.

Parmentier, E.M., Turcotte, D.L. & Torrance, K.E. 1976. Studies of finite amplitude non-Newtonian thermal convection with application to convection in the Earth's mantle. *J. Geophys. Res.,* **81**, 1839-1846.

Ratcliff, J.T., Tackley, P.J., Schubert, G. & Zebib, A., 1997. Transitions in thermal convection with strongly variable viscosity, *Phys. Earth Planet. Int.,* **102**, 201-212.

Schubert, G. & Anderson, C.A., 1985. Finite element calculations of very high Rayleigh number thermal convection. *Geophys. J. Roy. Astron. Soc.*, **80**, 575-601.

Schubert, G., Turcotte, D.L. & Olson, P., 2001. *Mantle Convection in the Earth and Planets*, Cambridge Univ. Press, UK. pp. 940.

Tackley, P.J., 1993. Effects of strongly temperature-dependent viscosity on time-dependent, three-dimensional models of mantle convection, *Geophys. Res. Lett.,* **20**, 2187-2190.

Tackley, P.J., 1998. Self-consistent generation of tectonic plates in three-dimensional mantle convection, *Earth Planet. Sci. Lett*, **157**, 9-22.

Turcotte, D. L., Torrance, K.E. & Hsui, A.T., 1973. Convection in the Earth's mantle, *Meth. Comp. Physics*, **13**, 431-451.

Yang, W. & Baumgardner, J.R., 2000. A Matrix-Dependent Transfer Multigrid method for Strongly Variable Viscosity Infinite Prandtl Number Thermal Convection, *Geophys. Astrophys. Fluid Dynamics*, **92**, 151-195.

Yuen, D.A., Hansen, U., Zhao, W., Vincent, A.P. & Malevsky, A.V., 1993. Hard turbulent thermal convection and thermal evolution of the mantle. *J. Geophys. Res.*, **98**, 5355-5373.

CHAPTER IV

MODELING DAMAGE, RECRYSTALLIZATION, AND TEXTURE USING AN INTERNAL STATE VARIABLE FRAMEWORK WITH APPLICATION TO MANTLE DYNAMICS PROCESSES

Introduction

Silicate rheology largely governs mantle dynamics. Hence, the realism of numerical modeling of mantle processes relies critically upon the realism of the manner in which rheological behavior is represented. With the computational power available today, the amount of relevant physics that can be incorporated in mantle dynamics models is far beyond what was imaginable just a decade ago (Cohen, 2005). Certainly, models that track material deformational history are now entirely feasible and dramatically improve the realism by which material deformation can be represented as shown in chapter two.

A key aspect to modeling the dynamics of the earth's mantle is the ability to represent the essential behavior of the lithospheric plates in a realistic manner. This essential behavior certainly involves the occurrence of zones of weakness at plate boundaries. For this to occur as a spontaneous feature in a numerical treatment weakening mechanisms must exist in the constitutive model.

Over the past decade several investigators have introduced damage as a history-like variable as a weakening mechanism in mantle convection simulations. Several

researchers (Bercovici, 1998; Tackley, 2000; Bercovici and Karato, 2002; Ogawa, 2003; Auth *et al.* 2003) have applied a void volume damage model to realize plate-like behavior. All were successful in formulating a damage variable that produced a history effect. Bercovici and Karato (2002) have pointed out, however, that these models are ad hoc and do not have a physical basis and that more work must be done to establish the correct physical interpretation of the damage parameter. Our approach was to adapt a damage model originally developed for metals within the BIISV framework to silicates. Our work thus uses an approach similar to those of the earlier investigators but with a different mathematical form, a form that does, however, admit to physical interpretation. For metals, the BIISV framework with the addition of a damage model by Horstemeyer *et al.* (2000) has been shown to successfully predict failure with high fidelity.

Damage is not the only rheological mechanism that can cause the cold thermal boundary layer to weaken. Recrystallization is another. Recrystallization has been studied for olivine aggregates that are deformed to large total strains (Ave'Lallemant and Carter, 1970; Wenk and Tomé, 1999; Bystricky *et al.*, 2000; Zhang *et al.*, 2000) as well as other geomaterials like Carrera marble (Covey-Crump, 1997). Dynamic recrystallization can cause mechanical weakening as shown by the studies of Post (1977), Zeuch (1982, 1983), and Tullis and Yund (1985). For application to the mantle recrystallization has mostly been studied in the context of grain size evolution. The work done by Solomatov (2001), Solomatov *et al.* (2002), and Solomatov and Reese (2008) shows grain growth and reduction is an important aspect of mantle flow. In particular Solomatov and Reese (2008) draw attention to the heterogeneities in the mantle due to grain size variations and the possibility that parts of the mantle, because of large grains size and high strength,

could be poorly mixed. These previous studies did not explore the possibility that dynamic recrystallization might lead to zones of weakness in the lithosphere.

Another important aspect of mantle convection is texture evolution. Because texture development results in seismic velocity anisotropy, its reality in the earth's mantle is well documented (Downes *et al.*, 1992; Mainprice and Silver, 1993; Chastel *et al.*, 1993; Blackman *et al.*, 1996; Blackman and Kendall, 1997; Ben Ismail and Mainprice, 1998; Xu *et al.*, 1998; Dawson and Wenk, 2000). While texture has been studied by these authors in the context of seismic anisotropy, we show that it can also play a role in making the mantle's cold boundary layer less stable.

We introduce and describe treatments for damage, recrystallization, and texture within the BIISV model framework for application to mantle dynamics modeling. We show that damage, recrystallization, and texture development can all contribute to weakening in the mantle's cold upper thermal boundary layer.

Model Description

In chapter three we focused on implementation of the BIISV model in the TERRA2D mantle convection code of Yang and Baumgarnder (2000). The BIISV framework readily accommodates the addition of damage, recrystallization, and texture into the relevant equations. In this previous implementation weakening in the cold thermal boundary layer occurred as a consequence of a simple yield stress bound on the viscosity,

$$\mu_{\max} = \frac{\tau_y}{2\dot{\varepsilon}} \tag{4.1}$$

where τ_y is a constant specified yield stress, and $\dot{\varepsilon}$ is the second deviatoric invariant of the strain rate. Equation (4.1) allows the cold thermal boundary layer to weaken when the local stress would otherwise exceed the specified yield stress value, typically chosen to be 100 MPa. The simple model neglects important features that are described in this study. We will first discuss inclusion of damage as a weakening mechanism.

The mechanical properties of a material obviously depend upon the density and types of microdefects within its structure. Deformation alters these microdefects, and when their density passes a certain threshold, damage is said to have occurred. The notion of a damaged state in continuum field theory emerged when Kachanov (1958) introduced a damage variable to describe the microdefect density locally in a creeping material. The idea was that damage could be quantified as the volume fraction of voids (or cracks) under creep conditions. Rabatnov (1963) advanced this notion with an evolution rate equation for void (crack) density. In a practical application, Bercovici (1998), Tackley (2000), Bercovici and Karato (2002), Ogawa (2003), and Auth *et al.* (2003) used porosity in simulations involving zones of lithospheric weakening.

Our approach is to include the defect volume fraction, representing damage, as a new internal state variable (ISV). A representative volume element of solid material with defects, or damage, will experience a reduced material strength, an enhanced inelastic flow, and a degraded elastic moduli as damage grows. When the damage reaches a critical value, failure occurs. Different damage rules can easily be incorporated into the BIISV framework. Bammann *et al.* (1993) have demonstrated the usefulness of the Cocks and Ashby (1980) void growth rule as damage rate equation in the BIISV model for metals. Horstemeyer *et al.* (2000) extended the damage capability in BIISV by including

a void/crack nucleation model (Horstemeyer and Gokhale, 1999) and McClintock void growth (McClintock, 1968). For this study we chose a form similar to Horstemeyer *et al.* (2000) in order to capture the different stress state effects and different fracture mechanisms but with a specific mathematical form for ease of implementation in TERRA2D. The evolution of damage is given by Equation (4.2)

$$\dot{\phi} = \left(1-\phi^2\right)\left[d_1\left(\frac{4}{27} - \frac{J_3^2}{J_2^3}\right) + d_2\left(\frac{J_3}{J_2^{3/2}}\right) + d_3\frac{I_1}{J_2^{1/2}}\right]\dot{\varepsilon}^{in} \tag{4.2}$$

where ϕ is a scalar damage, d_1, d_2, and d_3 are non-dimensional constants, and $\dot{\varepsilon}^{in}$ is the magnitude of the inelastic strain rate. I_1, J_2, and J_3 in Equation (4.2) are the first stress invariant, second deviatoric stress invariant, and third deviatoric stress invariant given by

$$I_1 = \sigma_{kk} \tag{4.3}$$

$$J_2 = \frac{1}{2}\sigma'_{ij}\sigma'_{ji} \tag{4.4}$$

$$J_3 = \frac{1}{3}\sigma'_{ij}\sigma'_{jk}\sigma'_{ki}\,. \tag{4.5}$$

Equations (4.3)-(4.5) are using Einstein notation for simplicity. The justification for using the expressions of particular stress invariants in Equation (4.2) is discussed in Horstemeyer and Gokhale (1999). Briefly, the three different terms inside Equation (4.2) represent a way to isolate the accumulation of damage due to particular stress states. The first term will operate by itself in torsion (shear); the second term distinguishes between tension and compression, and the third term is triaxiality (the ratio between hydrostatic pressure and deviatoric stress). Including all three terms allows for flexibility by turning on different damage stress state dependencies for a given numerical calculation. Also note only tension and torsion will produce damage for this model. Compression will have

a healing effect. This is not truly physical because damage can be driven by compression as shown in Horstemeyer *et al.* (2000), but will be ignored for this study.

Equation (4.2) can be analytically integrated assuming all variables except damage are constant over time. Damage then takes the form

$$\phi = \tanh\left(\left[d_1\left(\frac{4}{27}-\frac{J_3^2}{J_2^3}\right)+d_2\left(\frac{J_3}{J_2^{3/2}}\right)+d_3\frac{I_1}{J_2^{1/2}}\right]\varepsilon^{in}+C_\phi\right) \tag{4.6}$$

where ε^{in} is the accumulated inelastic strain, and C_ϕ is a constant of integration that will be set to zero for the purpose of this study. As the value inside the hyperbolic tangent increases the value of damage saturates to unity. Equation (4.6) was plotted for different stress states as a function of inelastic strain. Table 4.1 reproduced from Horstemeyer and Gokhale (1999) shows the values of the stress invariant expressions for inside the hyperbolic tangent in Equation (4.6) for the different stress states torsion, tension, and compression. Figure 4.1 shows the damage accumulation for the stress states of tension and torsion (simple shear). The constants used for d_1, d_2, and d_3 were 25.0, 25.0, and 1.0, respectively. For these constants the torsion damage accumulation was slower than the tension case. Looking at Table 4.1 the torsion stress state only has a contribution from the first term in Equation (4.6), whereas the tension stress state has a contribution from both the second and third terms in Equation (4.6).

Table 4.1 Stress invariant expressions for different stress states. Reproduced from Horstemeyer & Gokhale (1999).

	Tension	Compression	Torsion
$\frac{4}{27}-\frac{J_3^2}{J_2^3}$	0	0	$\frac{4}{27}$
$\frac{J_3}{J_2^{3/2}}$	$\frac{2}{3\sqrt{3}}$	$-\frac{2}{3\sqrt{3}}$	0
$\frac{I_1}{J_2^{1/2}}$	1	-1	0

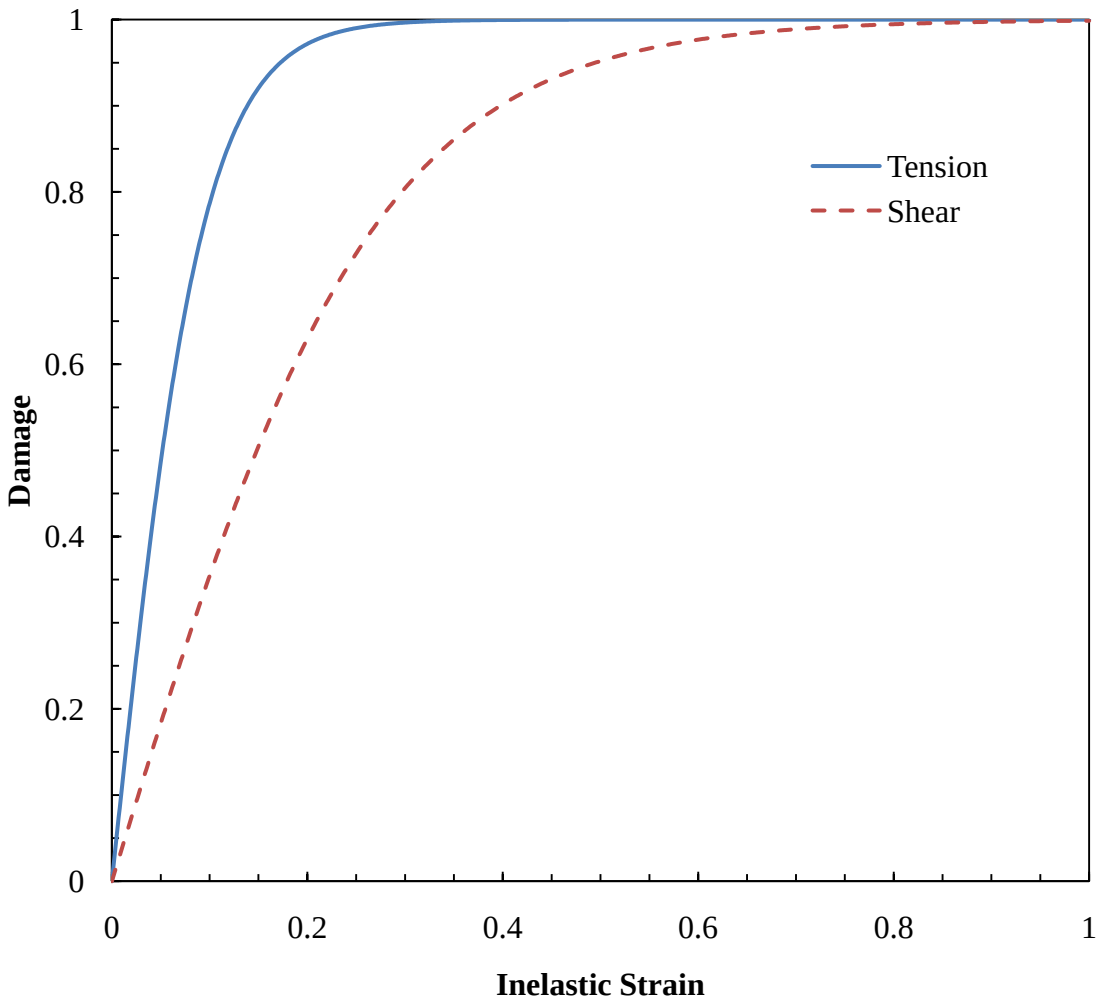

Figure 4.1 Damage accumulation versus inelastic strain for tension and shear stress states.

The inclusion of damage also affects some of the BIISV model equations discussed in chapters two and three. Damage (voids/cracks) will degrade the elastic moduli as well as increasing inelastic flow. The linear elasticity assumption can then be written,

$$\overset{\circ}{\underline{\sigma}} = \lambda(1-\phi)\,\mathrm{tr}\left(\underline{D}^{e}\right)\underline{I} + 2\mu(1-\phi)\underline{D}^{e} - \frac{\dot{\phi}}{(1-\phi)}\underline{\sigma} \tag{4.7}$$

where, λ and μ are the Lamé elastic constants. The Cauchy stress $\underline{\sigma}$ is advected with the elastic spin $\underline{W}^{e}$ as,

$$\overset{\circ}{\underline{\sigma}} = \dot{\underline{\sigma}} - \underline{W}^{e}\underline{\sigma} + \underline{\sigma}\underline{W}^{e} \tag{4.8}$$

which is done in order to keep the rate objective. The velocity gradient can be broken into both symmetric and skew symmetric parts with each being decomposed into elastic and plastic parts. The elastic stretching $\underline{D}^{e}$ and elastic spin $\underline{W}^{e}$ can be written,

$$\underline{D}^{e} = \underline{D} - \underline{D}^{in} \tag{4.9}$$

$$\underline{W}^{e} = \underline{W} - \underline{W}^{in} \tag{4.10}$$

Due to this decomposition, it is now appropriate to prescribe an equation for both the inelastic spin $\underline{W}^{in}$ and the flow rule $\underline{D}^{in}$. In this paper we prescribe the inelastic spin in the section dealing with modeling texture. The flow rule of the form

$$\underline{D}^{in} = f(T)\sinh\left[\frac{\left\|\underline{\sigma}'\right\| - \left(\kappa + Y(T)\right)(1-\phi)}{V(T)(1-\phi)}\right]\frac{\underline{\sigma}'}{\left\|\underline{\sigma}'\right\|} \tag{4.11}$$

where T is the temperature, κ is a scalar isotropic hardening variable, $\underline{\sigma}'$ is the deviatoric Cauchy stress, and $V(T)$, $Y(T)$, $f(T)$ are the temperature dependent scalar functions,

$$V(T) = C_1 \exp\left(\frac{-C_2}{T}\right) \tag{4.12}$$

$$Y(T) = \frac{1}{2} C_3 \exp\left(\frac{C_4}{T}\right)\left(1 + \tanh\left[C_{19}\left\{C_{20} - T\right\}\right]\right) \tag{4.13}$$

$$f(T) = C_5 \exp\left(\frac{-C_6}{T}\right). \tag{4.14}$$

Note the effect of damage on the linear elasticity in Equation (4.7) and inelastic flow in Equation (4.11). The form of Equation (4.11) is slightly different than the one found in chapter two and three, Equations (2.18) and (3.15), respectively. This chapter drops the effect of kinematic (anisotropic) hardening out of the flow rule and will be ignored through the duration of this chapter. Equations (4.7)-(4.14) along with the original evolution equation for isotropic hardening

$$\dot{\kappa} = \sqrt{\frac{2}{3}} H(T) \left\| \underline{D}^{in} \right\| - \left[\sqrt{\frac{2}{3}} R_d(T) \left\| \underline{D}^{in} \right\| + R_s(T) \right] \kappa^2 \tag{4.15}$$

$$R_d(T) = C_{13} \exp\left(\frac{-C_{14}}{T}\right) \tag{4.16}$$

$$H(T) = C_{15} - C_{16} T \tag{4.17}$$

$$R_s(T) = C_{17} \exp\left(\frac{-C_{18}}{T}\right) \tag{4.18}$$

can then be reduced to one dimensional set of equations and then numerically integrated to get the stress-strain behavior of damage. Table 4.2 contains the BIISV model constants for lherzolite used in chapter three. Using the constants for d_2, and d_3 mentioned earlier Figure 4.2 shows the stress-strain behavior for uniaxial tension with and without the inclusion of damage. As damage accumulates, the stress falls considerably. Another

constraint put on damage is that it is forced to be between 0 and 0.99 as negative damage is physically meaningless. The upper constraint of 0.99 allows for the completely damaged material to retain 1% of its original strength. This will be necessary to allow material to have a non-zero positive viscosity in the mantle convection simulations. This type of weakening allows for localization to occur in the cold thermal boundary layer, which we will discuss in a later section. Now we will turn attention to recrystallization as a weakening mechanism.

Table 4.2 BIISV model parameters used in this study.

Constant	Lherzolite Experimental Fit
C1 (MPa)	1.0×10^{-5}
C2 (K)	0.0
C3 (MPa)	1.0×10^{-5}
C4 (K)	0.0
C5 (s^{-1})	1.0×10^{-5}
C6 (K)	0.0
C15 (MPa)	1.03×10^{5}
C16 (MPa K^{-1})	65.8
C17 (s MPa^{-1})	4.15
C18 (K)	1.63×10^{4}

As was mentioned earlier most of the discussion of recrystallization in the context of the mantle has been in connection with the influence of grain size on rock strength. Grain size has been an important feature in modeling hardening materials since Hall (1951) and Petch (1953) introduced the inverse square root relation of grain size to stress. Yet, to restrict dislocation motion and hence the flow stress of the material to grain boundaries alone would be naïve and erroneous (Kuhlmann-Wilsdorf, 1968; Ashby, 1970). Upon deformation, crystalline material experiences the development of subgrain boundaries that affect the flow stress, and the subgrain boundaries evolve as deformation

proceeds such that differences between grains and subgrains become indiscernible (Hughes, 1992; Hughes, 1993). Hence, just from deformation the mean free path of dislocations decreases. This, in a sense, is recrystallization from the perspective of dislocation boundary effects on the work hardening rate. Recrystallization typically occurs from two sources: deformation under which dynamic recrystallization results and high homologous temperatures under which static recrystallization occurs. Poirer and Nicolas (1975) described two mechanisms that operate during dynamic recrystallization: one is the nucleation of new grains accompanied with grain growth, and the second is continued substructure development that forms and changes subgrains. As the material deforms the grain size is reduced and in silicates this has shown to cause a mechanical weakening (Post, 1977; Zeuch, 1982, 1983; Tullis and Yund, 1985).

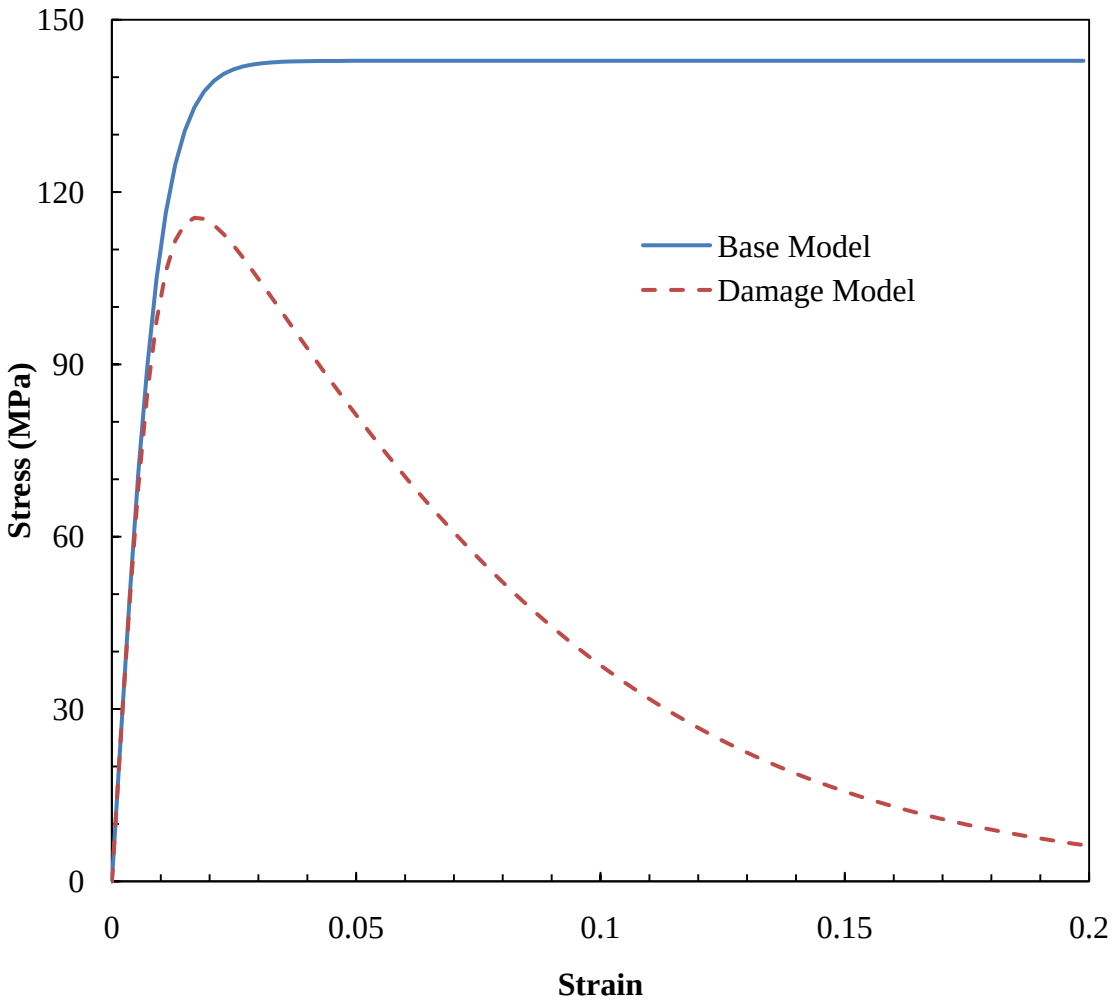

Figure 4.2 Comparison between the BIISV model with and without inclusion of damage model for a tension test. The strain rate for this test was 1.0×10^{-5} s^{-1} at a temperature of 1000 K.

Because of these observations, we restrict our treatment to the mechanical weakening produced by recrystallization. Other effects will be ignored in this study as a first order approach. As such, we make the recrystallization ISV affect the recovery of the isotropic hardening ISV. In a continuum sense, the rate of isotropic hardening then changes due to the dislocation boundaries that are changing from the recrystallization

events. The changes in isotropic hardening evolution equation, Equation (4.15), to include this first order mechanical weakening is

$$\dot{\kappa} = \sqrt{\frac{2}{3}} H(T) \left\| \underline{D}^{in} \right\| - \left[\sqrt{\frac{2}{3}} R_d(T) \left\| \underline{D}^{in} \right\| + R_s(T) + R_x \right] \kappa^2 \tag{4.19}$$

where R_x is the newly introduced effect of recrystallization. R_x has the ability to annihilate the statistically stored dislocations, which is what the isotropic hardening represents in an average continuum sense. We further define R_x as

$$R_x = \hat{R}_x \left(\bar{\kappa} - \kappa_c \right) \tag{4.20}$$

$$\hat{R}_x = r_1 \exp\left(\frac{-r_2}{T} \right) \tag{4.21}$$

$$\kappa_c = r_3 \sqrt{\frac{H(T) \left\| \underline{D}^{in} \right\|}{R_d(T) \left\| \underline{D}^{in} \right\| + R_s(T)}} \tag{4.22}$$

$$\dot{\bar{\kappa}} = \sqrt{\frac{2}{3}} H(T) \left\| \underline{D}^{in} \right\| - \left[\sqrt{\frac{2}{3}} R_d(T) \left\| \underline{D}^{in} \right\| + R_s(T) \right] \bar{\kappa}^2 \tag{4.23}$$

where r_1, r_2, and r_3 are constants. The variable $\bar{\kappa}$ is a dummy variable that acts like a switch to turn on recrystallization when it gets above a specified value of hardening, κ_c. The dummy variable $\bar{\kappa}$ has its own evolution equation shown in Equation (4.23) that is identical to the original unaltered κ evolution equation. The form of κ_c shown in Equation (4.22) is used, because for a given strain rate and temperature the value of $\bar{\kappa}$ will eventually reach this value at steady state. See Bammann (1990) for details on the calculation of the steady state value. The constant r_3 can then be used to pick how far before steady state recrystallization will turn on by choosing a value between 0 and 1.

Equation (4.21) allows for a temperature dependence on how much weakening affects the isotropic hardening in Equation (4.19).

By including recrystallization in the isotropic hardening the overall mechanical behavior will soften after a material accumulates enough hardening. The behavior of Equations (4.7)-(4.11) can be shown by solving a reduced set of one dimensional BIISV equations representing uniaxial compression following the same procedure used in Bammann (1990). The BIISV model constants in this study are the same as in chapter three and listed in Table 4.2. The constants r_2 and r_3 used to determine the stress-strain recrystallization behavior are 18,000 K and 0.5. Figure 4.3 shows the difference between including recrystallization and the original behavior by varying r_1 values of 0.05 MPa^{-2}, 0.1 MPa^{-2}, and 0.5 MPa^{-2}. The recrystallization model decreases the stress by lowering the isotropic hardening. The behavior shown in Figure 4.3 has the isotropic hardening dropping to a steady state much lower than the original BIISV model to allow for localization to occur. The constants used in Figure 4.3 show the effects of introducing the recrystallization model. When experimental stress strain data becomes available we will be able to correlate real recrystallization constants. Until then, these constants will be used to show the model's capability. Finally, we will now discuss modeling texture in the BIISV model.

As was earlier stated evidence for texture development in the mantle is abundant from seismic anisotropy observations. The question is how do we model the effects of texture in a constitutive model like the BIISV model? Besides directly implementing crystallographic orientations within the constitutive model, the most appropriate repository for a macroscale representation of textural and dislocation substructural

rotations (microtexture) is the inelastic spin and the effects on the hardening rule, but inelastic spin prescriptions have not typically been based on both texture and dislocation substructure (Horstemeyer and McDowell, 1998).

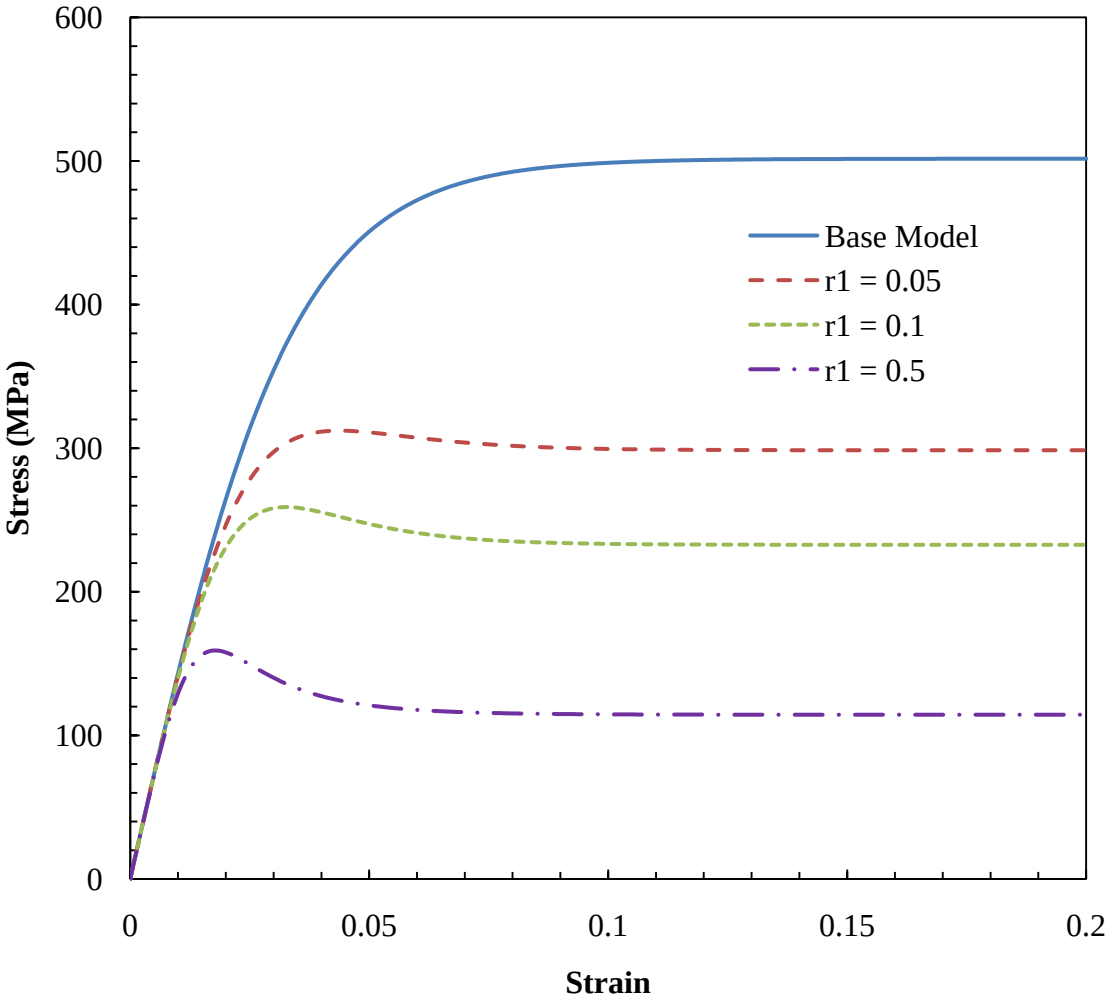

Figure 4.3 Comparison between the BIISV base model and including recrystallization for different r_1 values. (Units for r_1 are MPa^{-2}). The strain rate for these tests was 1.0×10^{-4} s^{-1} at a temperature of 1200 K.

Some guidelines are in order to develop this ISV in the context of macroscale continuum theory. First, anisotropic hardening arises from two kinematical sources: (1) heterogeneity arising from nonuniformity of deformation among grains, sometimes

referred to as textural or orientation hardening and (2) from heterogeneous dislocation substructures that arrange themselves as lamellar bands, dense dislocation walls, microbands, cell walls, and subgrains. A new anisotropic ISV, $\underline{A}$, would represent the configurational or geometrical quantity from the two kinematic sources that seem to be lacking in macroscale models. This ISV would represent the effect of texture and dislocation substructure on the macroscale hardening evolution equations and plastic spin. Prantil *et al.* (1993), and others have proposed textural evolution equations cast in a mesoscale polycrystalline plasticity framework.

The texture/substructure ISV $\underline{A}$ could have up to a rank of order four. For numerical efficiency, simpler representations of $\underline{A}$ can be second order or even scalar (a second order tensor representation is used in this paper). We introduce the texture/substructure effect into the hardening moduli functions and inelastic spin to account for deformation-induced texture by means of the following evolution equation

$$\overset{\circ}{\underline{A}} = a_1 \underline{D}^{in} - a_2 \left\| \underline{D}^{in} \right\| \left\| \underline{A} \right\| \underline{A}, \tag{4.24}$$

where a_1 and a_2 are constants. The texture tensor $\underline{A}$ is also advected with the elastic spin as,

$$\overset{\circ}{\underline{A}} = \dot{\underline{A}} - \underline{W}^e \underline{A} + \underline{A} \underline{W}^e \tag{4.25}$$

in order to maintain objectivity. The constants a_1 and a_2 were chosen to be unity to allow the texture ISV to act like a structure tensor. The magnitude of the texture ISV will never be greater than one with these constants. The inelastic spin can then be prescribed in terms of the texture ISV

$$\underline{W}^{in} = \frac{1}{w_1 \exp\left(w_2 \varepsilon^{in}\right)}\left(\underline{A}\underline{D}^{in} - \underline{D}^{in}\underline{A}\right) \tag{4.26}$$

where w_1 and w_2 are constants. The form of Equation (4.26) is similar to that of Bammann and Aifantis (1987) and closer to the form of Horstemeyer and McDowell (1998). The main difference is the kinematic hardening ISV is used in prescribing inelastic spin instead of the texture ISV. We then use the texture ISV to affect the isotropic hardening evolution given by Equation (4.19) as,

$$\dot{\kappa} = \sqrt{\frac{2}{3}} H\left(T\right)\left\|\underline{D}^{in}\right\|\left\|\cos\theta\right\| - \left[\sqrt{\frac{2}{3}} R_d\left(T\right)\left\|\underline{D}^{in}\right\| + R_s\left(T\right) + R_x\right]\kappa^2 \tag{4.27}$$

$$\cos\theta = \frac{\underline{A} : \underline{D}^{in}}{\left\|\underline{A}\right\|\left\|\underline{D}^{in}\right\|} \tag{4.28}$$

where the $\cos\theta$ variable will have a value between -1 and 1. The value of $\cos\theta$ will be 1 in uniaxial tension and -1 in uniaxial compression. Torsion (shear) is what will be affected by the inclusion of Equations (4.24)-(4.28). This is known as torsional softening. To the authors' knowledge, no effective stress-strain curves have been published for olivine or olivine aggregates that illustrate the differences in compression versus torsion or simple shear. However, one would expect differences though; as such differences have been observed in titanium (Tome and Kocks, 1985), which is similar to olivine in that it is a hexagonal close packed crystal. In fact, many crystalline materials display this behavior. Essentially, different stress states promote different styles of textural evolution.

Equations (4.24)-(4.28) can also be integrated numerically to reveal the effects of the texture development on the mechanical behavior. We chose the constants w_1 and w_2 to have values of unity for simplicity, but the constants can be correlated to experimental

data once they are obtained. Figure 4.4 shows the change in the mechanical behavior between the original BIISV model and the version that includes the texture model. The texture model admits torsional softening (Horstemeyer and McDowell, 1998) for a lower steady state value of stress.

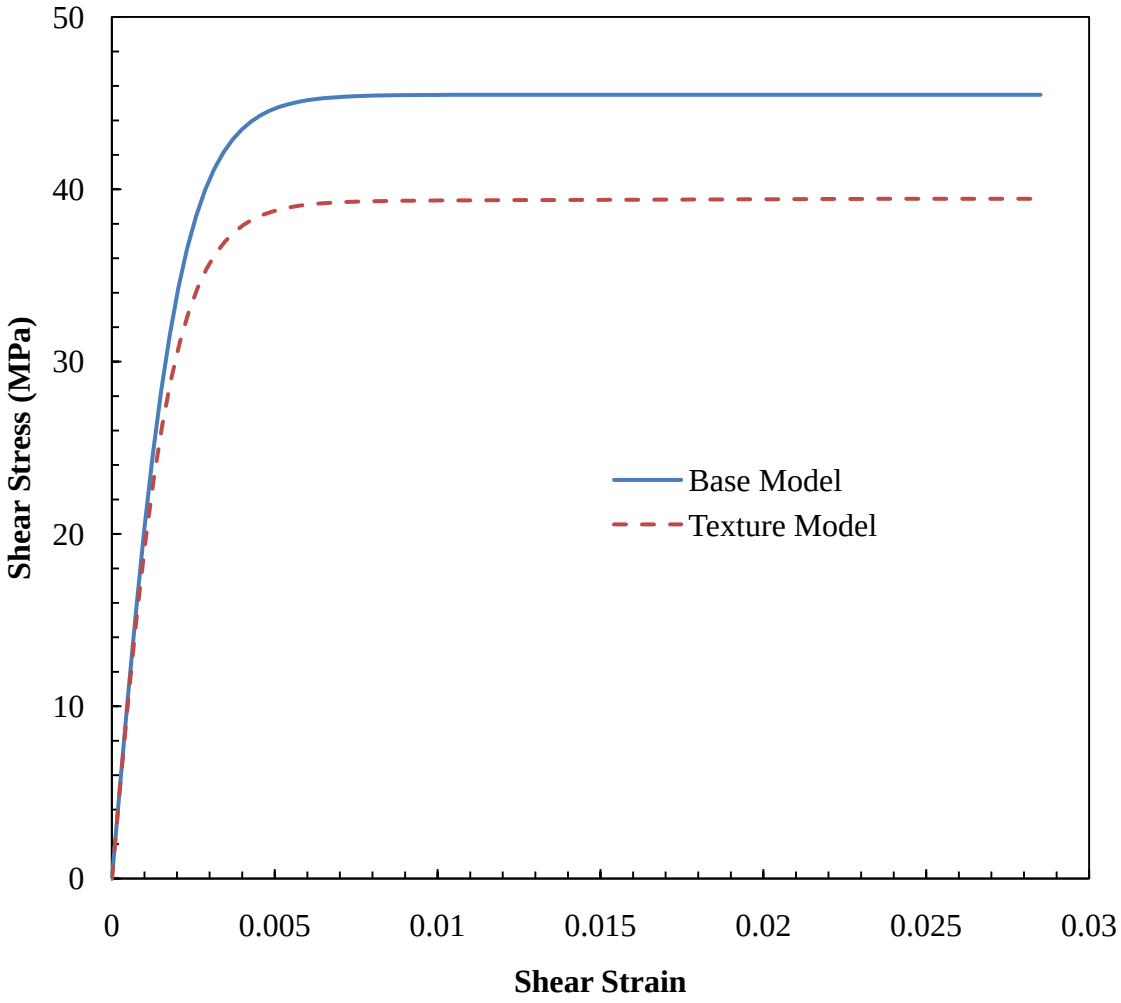

Figure 4.4 Comparison between BIISV model in torsion with and without texture model. The strain rate involved in these tests was 1.0×10^{-7} s^{-1} at a temperature of 1000 K.

We will now briefly describe our approach for incorporating the damage, recrystallization, and texture treatments into the BIISV model. The implementation of the

BIISV model in chapter three used the radial return method originally proposed by Krieg and Krieg (1977). Only slight changes are necessary in the implementation. Only the changes in the procedure will be discussed here. As was done in chapter three, only the deviatoric response will be considered. Future work can include effects of pressure on the yield surface. The new value of damage is calculated using the updated values of stress to evaluate the different stress invariant expressions and the updated value for inelastic strain. In this study the value used for the first invariant in Equation (4.6) is the pressure calculated by TERRA2D. In the recrystallization model the trial $\bar{\kappa}$ is calculated first and then the trial κ is determined. As is seen in Equation (4.11) only the trial κ value affects the yield criterion. Both trial values are updated in the same way after the inelastic strain increment is found. The texture model affects the implementation in three ways. First, the updated inelastic spin is calculated using previous time step values for $\underline{A}$, $\underline{D}^{in}$, and ε^{in}, which in turn is applied to rotate the stress and texture tensors to maintain objectivity. Second, the updated value for $\|\cos\theta\|$ is calculated also using previous time step values for $\underline{A}$ and $\underline{D}^{in}$. Finally, the updated value of $\|\cos\theta\|$ is utilized to determine the inelastic strain increment, which is applied to update all the ISVs. The computational cost of this method is around 10% of the total simulation time, which is only a 1% increase from the previous BIISV implementation. We will now turn our attention to the setup of the example cases to illustrate these new features in TERRA2D.

Numerical Simulations Setup

The illustrative mantle convection cases run for this study resemble both those by Yang and Baumgardner (2000) and those found in chapter three. Table 4.3 lists the

parameters common to all the TERRA2D cases performed in this study. Each element in computational mesh has a 22.57 km length on each side. Figure 4.5 illustrates the boundary conditions for these cases. The side boundary conditions are periodic and the top and bottom surfaces are free slip. A constant temperature of 300 K is maintained on the upper surface and the bottom surface does not allow any vertical heat flux. Equation (4.29) describes the initial vertical temperature distribution,

$$T_i(y) = \begin{cases} T_{ref}, & 0 < y < n_2 - 5 \\ T_{upper} + \dfrac{T_{ref} - T_{upper}}{5}(n_2 - y), & n_2 - 5 < y < n_2 \end{cases}, \tag{4.29}$$

which represents an initial upper thermal boundary layer that is five elements thick for the grid resolution 512 by 128. The horizontal temperature distribution is given by

$$T(x, y) = T_i(y) + 0.03 T_i(y)(h/2)\cos\frac{2\pi x}{w}, \tag{4.30}$$

which represents a temperature field with two counter-rotating convecting cells. The Boussinesq approximation and uniform internal heating are assumed for all the cases.

Table 4.3 Input parameters common to all the illustrative cases in this study.

width, w	11560 km
thickness, h	2890 km
horizontal number of cells, n_1	512
vertical number of cells, n_2	128
reference density, ρ_0	3400 kg m^{-3}
Gravitational acceleration, g	10 m s^{-2}
thermal expansion coefficient, α	2.5×10^{-5} K^{-1}
thermal conductivity, k	4 W m^{-1} K^{-1}
specific heat, c_p	10^3 J kg^{-1} K^{-1}
heat generation rate, H	5×10^{-12} W kg^{-1}
reference viscosity, μ_0	1×10^{23} Pa s
minimum viscosity, μ_{min}	0.01 μ_0
reference temperature, T_0	1500 K

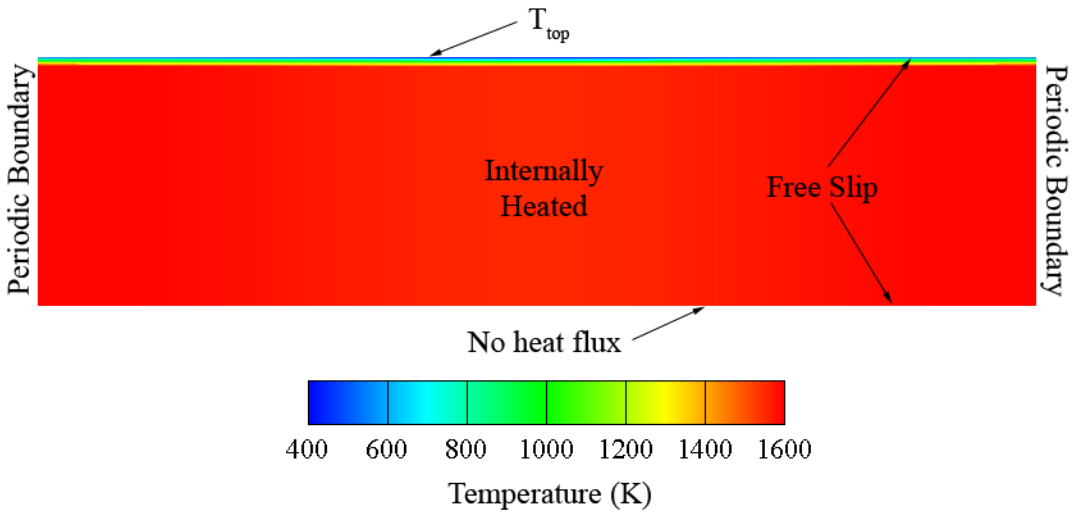

Figure 4.5 Thermal and velocity boundary conditions for illustrative TERRA2D simulations.

To highlight some of the changes in mantle dynamics arising from the inclusion of damage, recrystallization, and texture, we performed a limited parametric study. We isolate the individual damage parameters to show how different stress states can affect damage growth. For recrystallization we vary the r_1 parameter to illustrate its affect on the dynamics but keep the r_2 and r_3 parameters fixed at 18,000 K and 0.5, respectively.

We use different initial texture states to show the role played by initial texture. The different initial texture states are no initialization, plane strain compression, and shear. No initialization means that the initial values of $\underline{A}$ are all zero. For the plane strain compression initial texture, the tensor $\underline{A}$ is

$$\underline{A} = \begin{bmatrix} 1 & 1 \\ 1 & -1 \end{bmatrix}, \tag{4.31}$$

which is characteristic of a rolled material. The shear initial texture is prescribed by

$$\underline{A} = \begin{bmatrix} 0 & 1 \\ -1 & 0 \end{bmatrix}, \tag{4.32}$$

which corresponds to a material that has undergone considerable shear. Other exotic histories could be conceived that shows the power of including history effects in a material model. Finally, a simulation with a mixture of these models is presented to show the flow features that emerge by combining the three treatments. Table 4.4 lists the different cases with their respective parameters values. The following section discusses the results of the cases described in Table 4.4.

Table 4.4 TERRA2D parametric study cases.

Case #	d_1	d_2	d_3	r_1 (MPa^{-2})	Include Texture	Texture Initialization
1	0	0	0	0	no	n/a
2	5	0	0	0	no	n/a
3	0	50	0	0	no	n/a
4	0	0	1	0	no	n/a
5	5	50	1	0	no	n/a
6	0	0	0	1000	no	n/a
7	0	0	0	10	no	n/a
8	0	0	0	0.1	no	n/a
9	0	0	0	0	yes	none
10	0	0	0	0	yes	plane strain compression
11	0	0	0	0	yes	shear
12	0.01	0.01	0	1	yes	shear

Results

The first case represents a reference case of the BIISV model with none of the three new treatments active. As expected the BIISV without these weakening processes results in an extremely strong immobile cold thermal boundary layer that does not break up. Figure 4.6 shows three snapshots from the time history of this case. Figure 4.6c displays classic stagnant lid behavior as reported by Moresi and Solomatov (1995), Yang and Baumgardner (2000), and others. Small thermal instabilities or drips emerge from the bottom of the cold thermal layer. The case summarized by Figure 4.6 is different from the reference case in chapter three, because the current simulation does not contain the yield stress viscosity limit described by Equation (4.1). The case of Figure 4.6 serves as a baseline against which the remaining simulations can be compared.

Cases 2, 3, 4, and 5 highlight various aspects of the damage treatment presented earlier. Figure 4.7 displays snapshots for Case 2 where only the shear/torsional feature in the damage treatment is active. In this case, only material in a state of shear stress accumulates damage. As shown in Figures 4.7a and 4.7b the thermal boundary layer experiences localized weakening and plunges toward the bottom. The upper layer is eventually depleted after this initial avalanche of its cold and strong material. As the case proceeds the damage causes weakening throughout the boundary layer and inhibits the layer from achieving any appreciable thickness. Figure 4.7c shows small drips removing the cool but weakened material from the thin boundary layer. The flow pattern of Figure 4.7c resembles an isoviscous case in which the strength of the boundary layer is the same as that of the deeper interior.

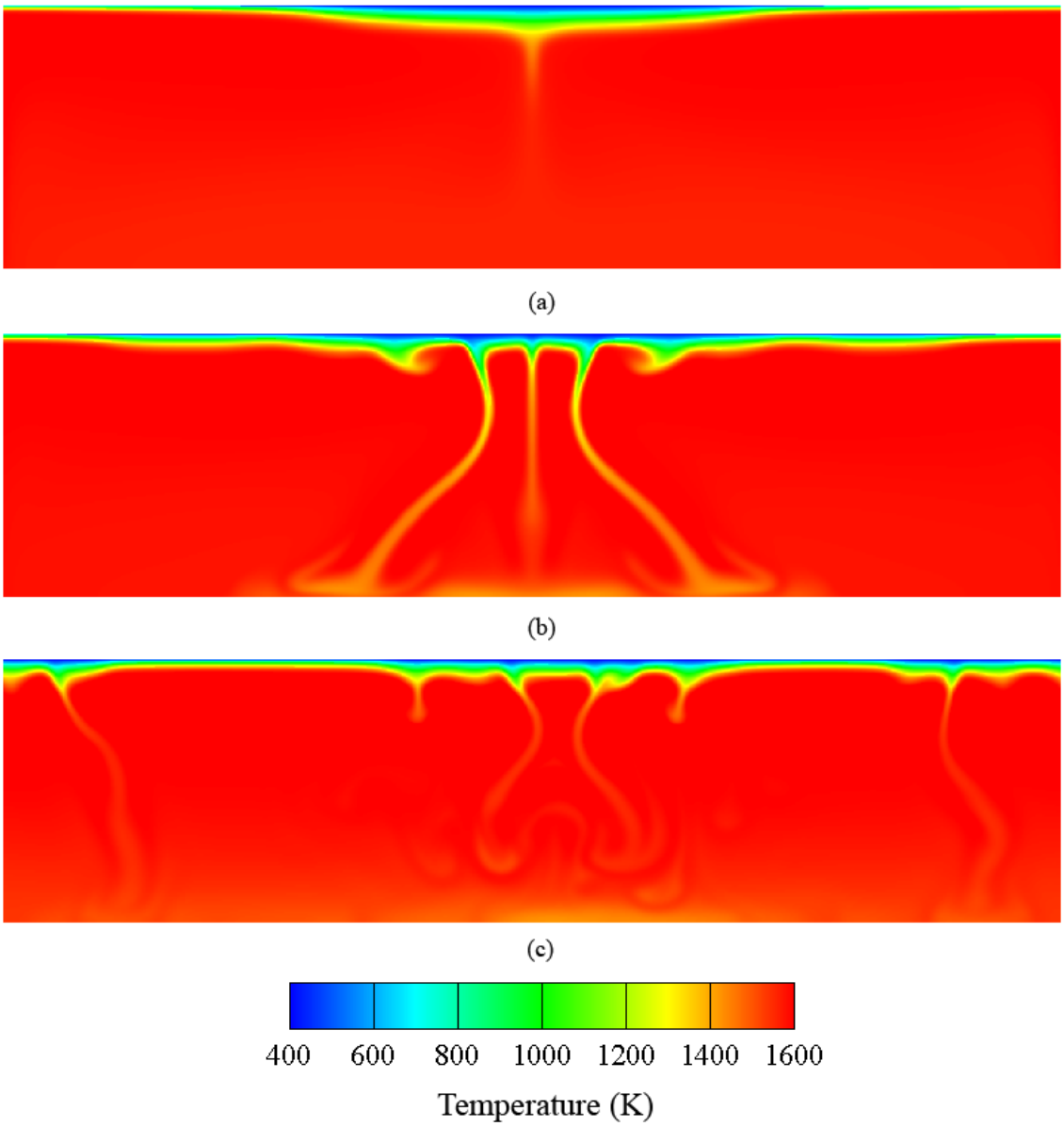

Figure 4.6 Temperature fields for the baseline BIISV Case 1. Snapshots in time at a) 50 Myr, b) 200 Myr, and c) 700 Myr.

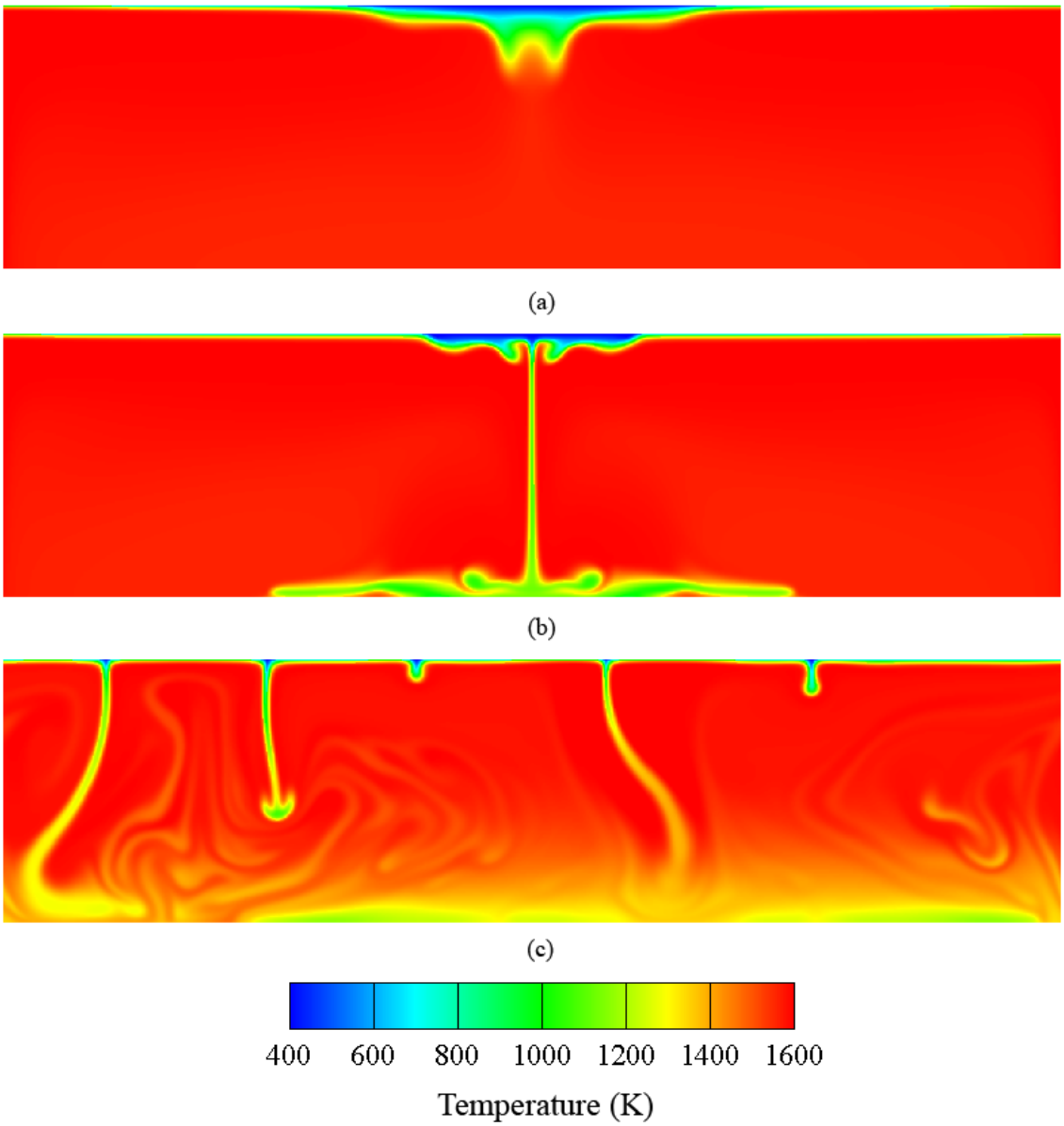

Figure 4.7 Temperature fields for Case 2 with damage contribution only from the shear/torsion. Snapshots in time at a) 30 Myr, b) 50 Myr, and c) 200 Myr.

Case 3 includes the damage effects from only tension/compression. In this case only material under tension accumulates damage. Figure 4.8 shows snapshots from this case. Much like in Case 2, Figures 4.8a and 4.8b show the cold boundary layer localizing and plunging downward; however, not all the cold thermal layer is removed in the first

avalanche. Note the small area of thickened thermal boundary layer left over even in Figure 4.8c. However, the rest of the upper layer is thin and weak just as in Case 2.

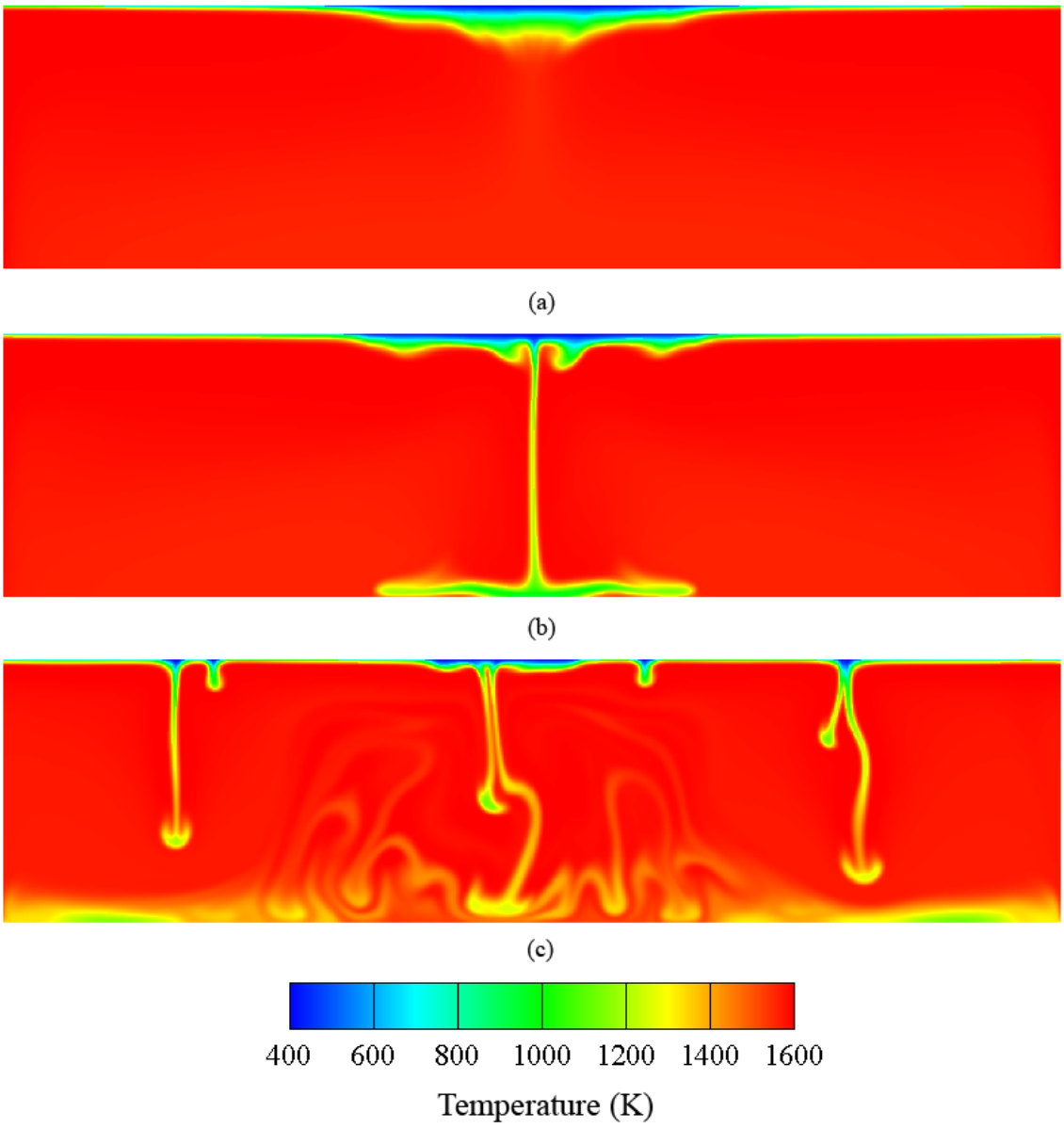

Figure 4.8 Temperature fields for Case 3 with damage only from tension/compression. Snapshots in time at a) 30 Myr, b) 50 Myr, and c) 200 Myr.

Case 4 includes the damage effects from triaxiality. In this case only material under high stress states of triaxiality accumulates damage. As shown in Figure 4.9 damage arising from triaxial deformation is not as effective as from the shearing and tensile types of deformation of Cases 2 and 3 in mobilizing the thermal boundary layer. Although this type of damage allows some of the boundary layer to mobilize, it is not sufficiently effective to cause the entire boundary to mobilize. Figure 4.10 displays damage fields for Cases 2, 3, and 4 at 50 Myr. The damage field resulting from shear deformation in Figure 4.10a shows saturation levels of damage accumulation throughout the cold material. By contrast, the damage accumulation arising from tensile deformation displayed in Figure 4.10b is spotty because the material undergoes this type of deformation less consistently. While some of the cold material is under tension, other regions are under compression, which has a healing effect on damage. Figure 4.10c shows the damage accumulation field due to triaxiality. Only a thin zone at the base of the thermal boundary layer has high positive triaxiality. This represents only a small region which is consistently under a high tensile pressure relative to where the hydrostatic pressure prevails. The latter situation tends to heal this type of damage. More research needs to be done to determine pressure effects on damage accumulation and mantle dynamics as a whole.

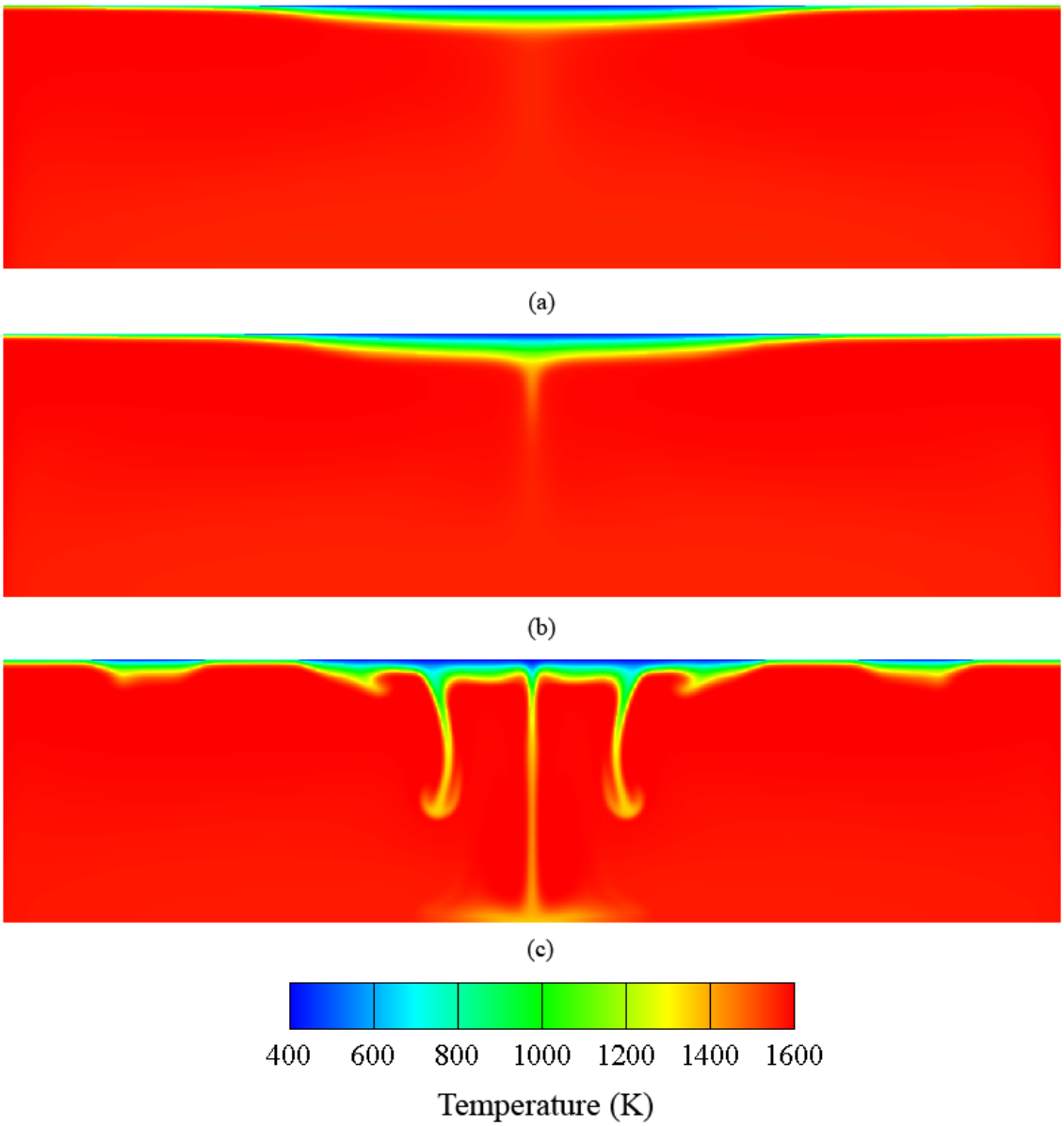

Figure 4.9 Temperature fields for Case 4 with damage only from triaxial deformation. Snapshots in time at a) 30 Myr, b) 50 Myr, and c) 200 Myr.

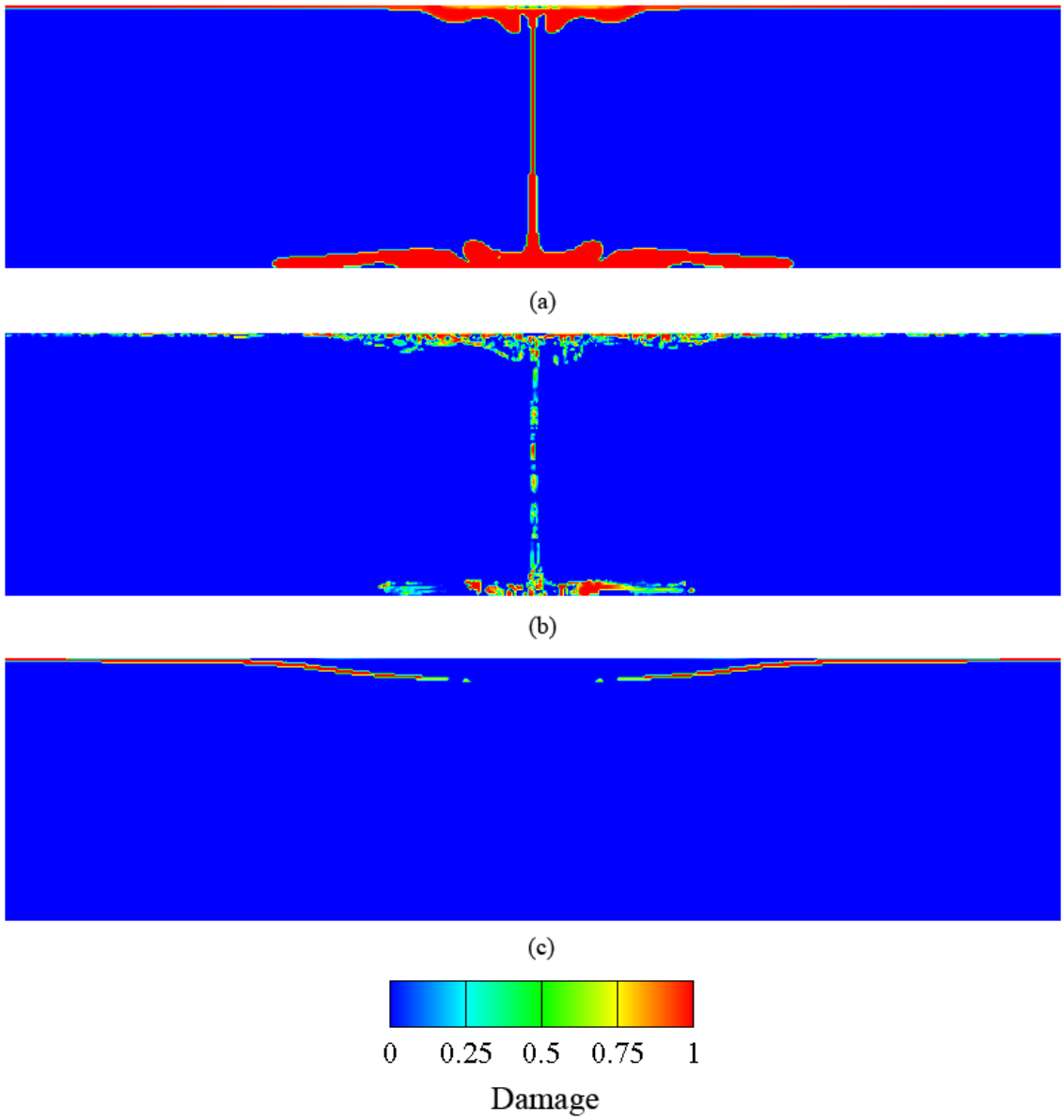

Figure 4.10 Plots of the damage field for the three damage cases at a time of 50 Myr a) torsion/shear component alone (Case 2), b) tension/compression component alone (Case 3), and c) triaxiality component alone (Case 4).

The fourth damage case, Case 5, includes all three damage components. Figure 4.11 shows time snapshots of the temperature field for this case. At the beginning of the case weakening of the thermal boundary layer occurs via accumulating shear but is

slowed due to negativity of the triaxiality component. Eventually the tension/compression damage accumulation is sufficiently strong for the layer to mobilize and plunge into the interior. The tension/compression damage component dominates at later times shown in Figure 4.11c, which is why Figures 4.8c and 4.11c have similar character. Again, shearing damage appears to be the dominant damage mechanism at the beginning of the subduction, but tensile damage maintains the thermal layer mobility later in time.

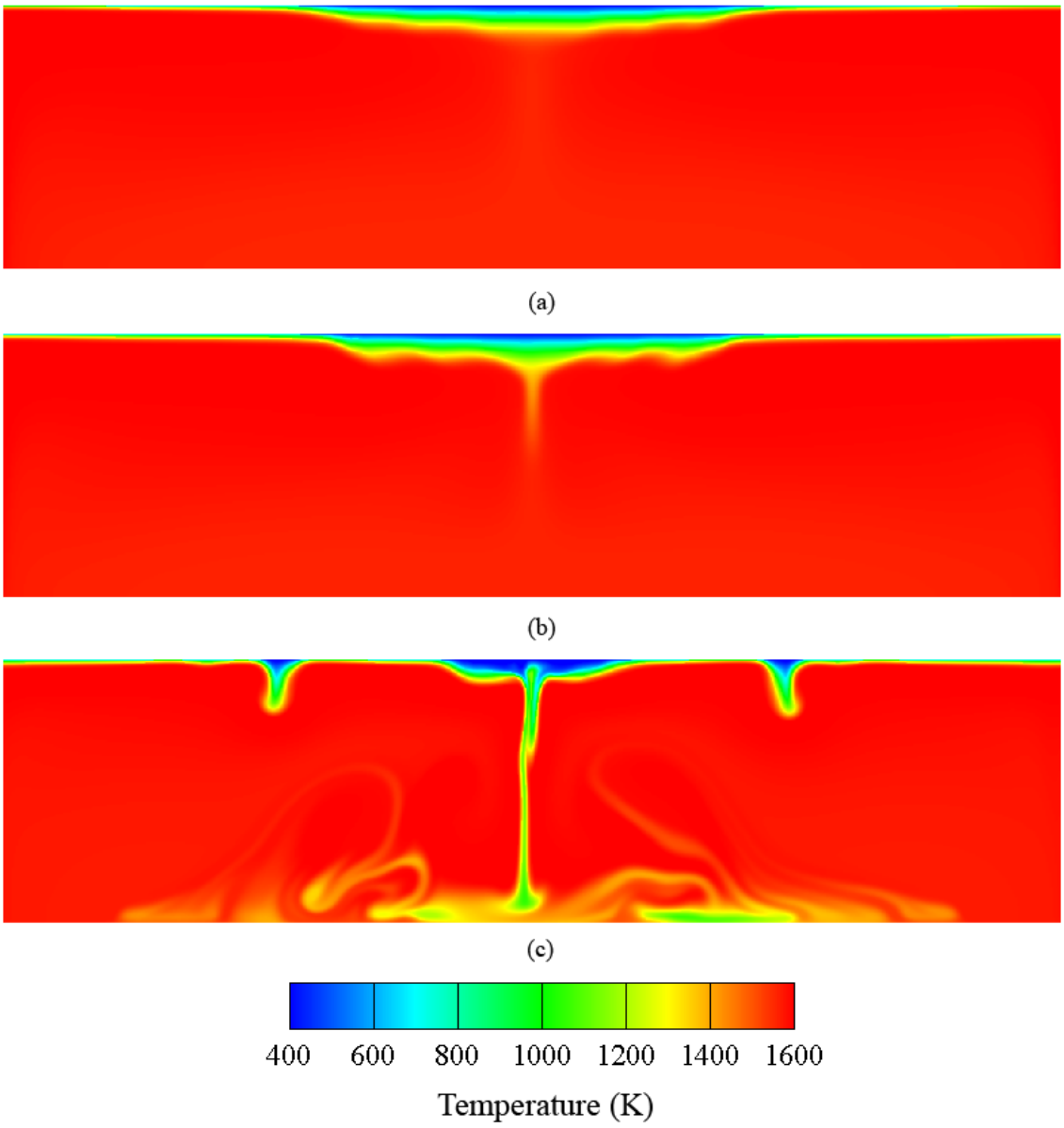

Figure 4.11 Temperature fields for Case 5 with all damage components active . Snapshots in time at a) 30 Myr, b) 50 Myr, and c) 200 Myr.

We will now turn attention to the recrystallization cases in Table 4.4, Cases 6, 7, and 8. The r_1 parameter value chosen for Case 6 corresponds to an extreme intensity of recrystallization. Physically, r_1 represents the probability of a recrystallization event occurring. The event destroys some of the isotropic hardening that originally gave the

material its strength. At temperatures above 800 K this translates to steady state strength of less than 1% the material's original steady state strength without recrystallization. Figure 4.12 shows snapshots of the temperature field for Case 6. The case looks strikingly similar to the one performed in chapter three using a yield stress value of 100 MPa. Figure 4.13 compares the two cases at times when the avalanches look similar. Case 6 is at time of 170 Myr, while the yield stress case is at a time of 150 Myr. Although there is a small displacement in time, qualitatively the flow features are very similar. For this value for r_1, the state stress relationship shown in Figure 4.3 results in deformation behavior much like the yield stress rheology with a yield stress of 100 MPa. The time delay between the two cases is due to Case 6 requiring some extra stress to surmount the hump in the stress-strain curve.

Figure 4.14 displays the results of Case 7 for a 100-fold decrease of the r_1 parameter relative to Case 6. In this case periodic avalanches near the middle of the domain occur at 90 Myr intervals starting at 50 Myr. At 320 Myr the periodicity of the avalanches slows considerably, and newly forming avalanches have a similar periodic character. Figure 4.14a shows the first avalanche in progress at 30 Myr, and Figure 4.14b shows the temperature field just after the second avalanche. Figure 4.14c shows the other avalanche regime after its second avalanche.

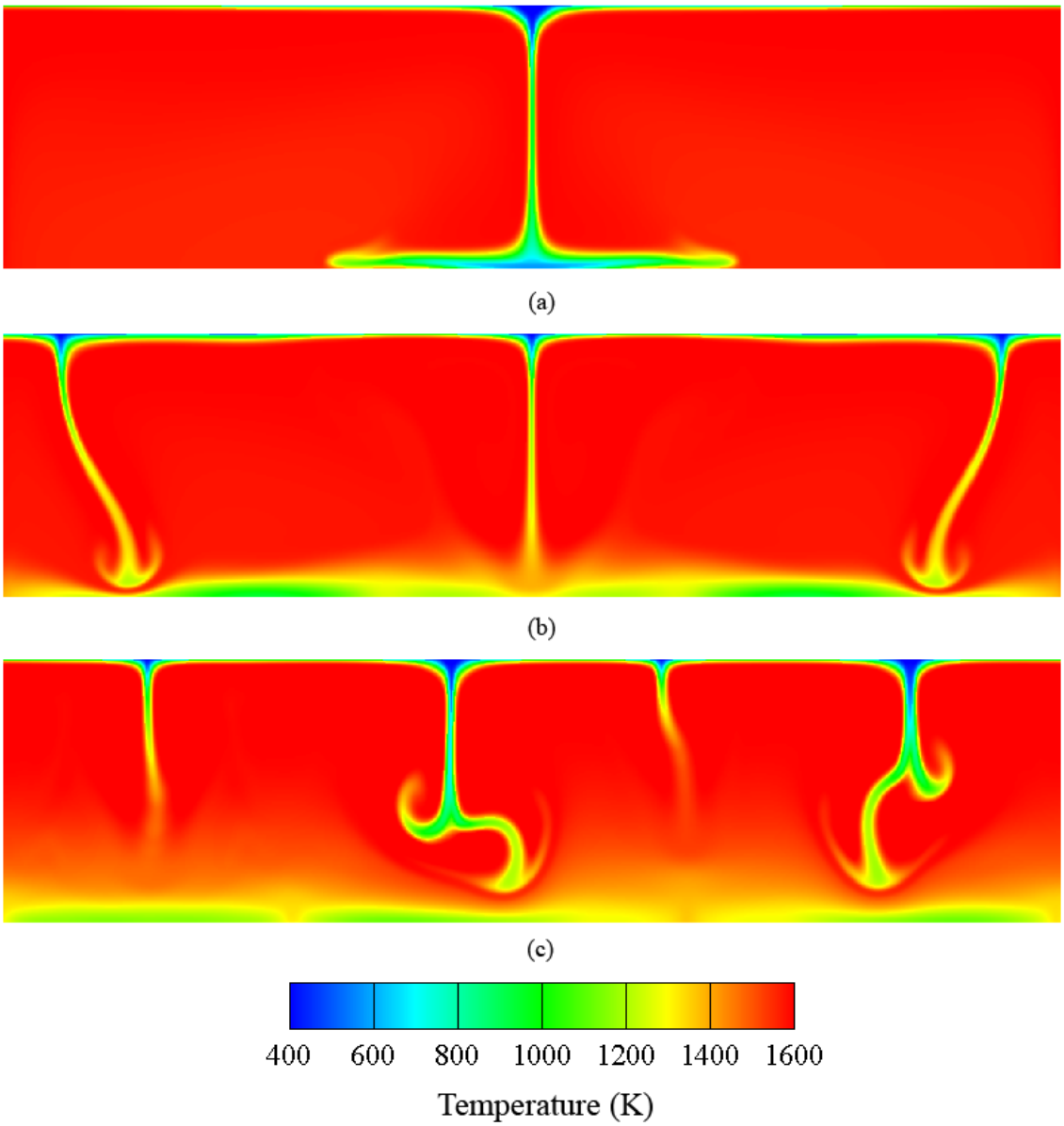

Figure 4.12 Temperature fields for Case 6 with the recrystallization parameter r_1 = 1000 MPa^{-2}. Snapshots in time at a) 30 Myr, b) 170 Myr, and c) 380 Myr.

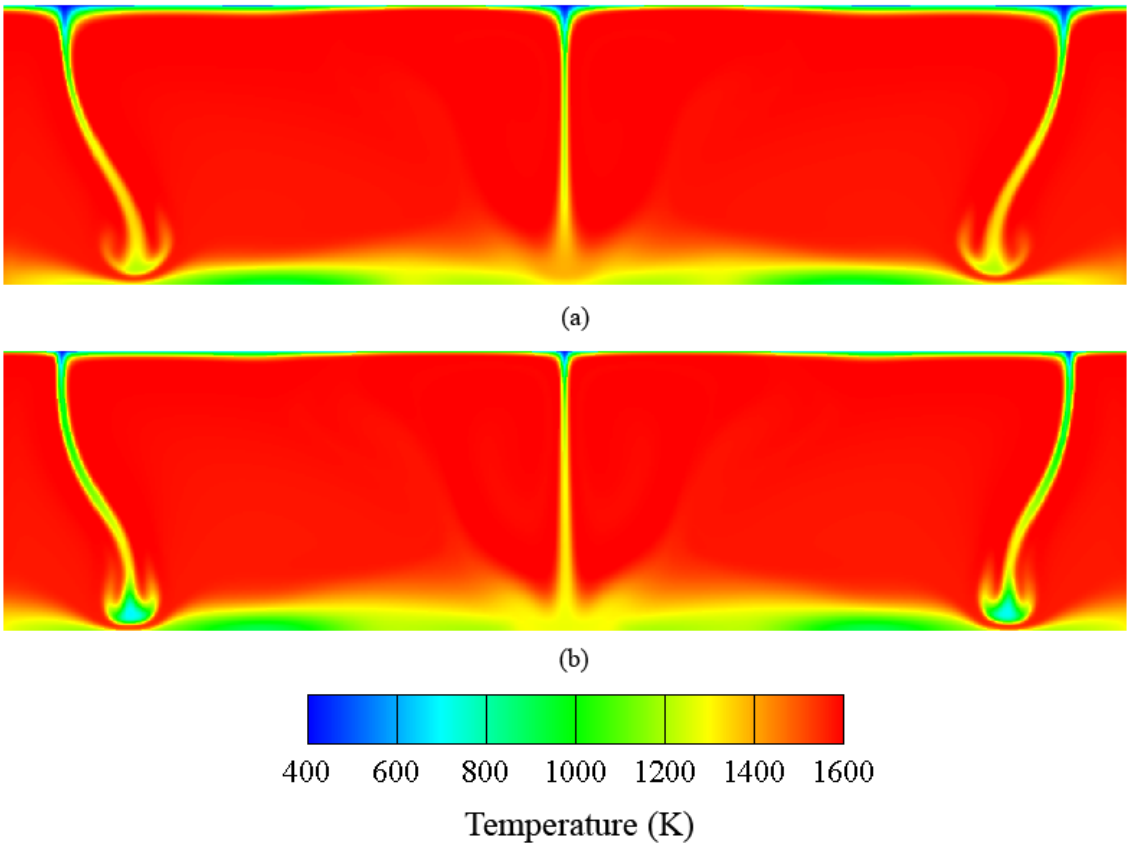

Figure 4.13 Comparison of temperature fields from a) recrystallization Case 6 with r_1 = 1000 MPa^{-2} at 170 Myr and b) yield stress case with τ_y = 100 MPa (reported in chapter three) at 150 Myr.

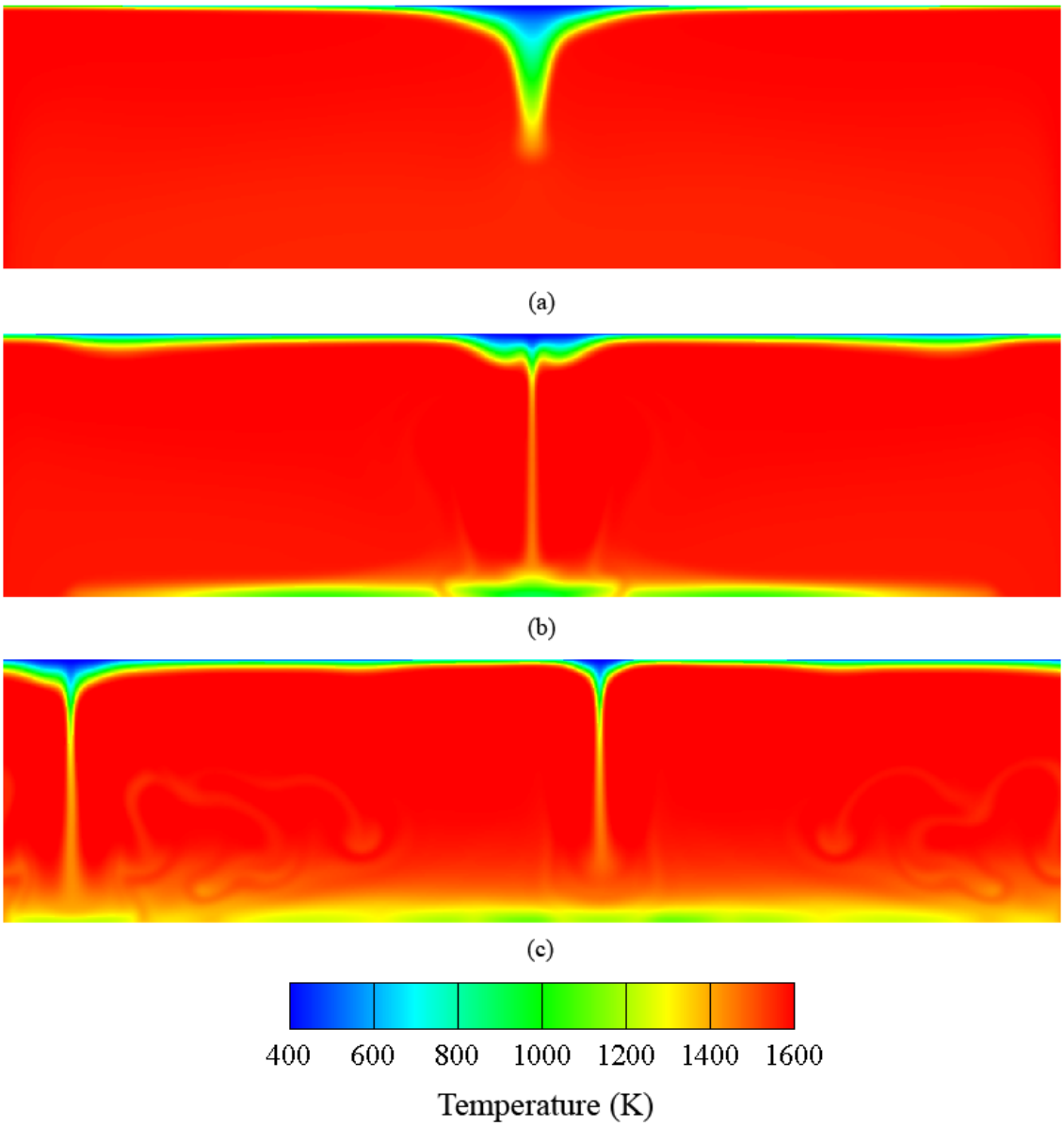

Figure 4.14 Temperature fields for Case 7 with recrystallization parameter $r_1 = 10$ MPa^{-2}. Snapshots in time at a) 30 Myr, b) 170 Myr, and c) 380 Myr.

The third recrystallization case, Case 8, shown in Figure 4.15 involves a further reduction in the r_1 parameter to 0.1 MPa^{-2}. The magnitude of the first avalanche of this case shown in Figure 4.15b is much smaller than the first avalanches of Cases 6 and 7. The avalanches in Case 8 do not deplete the colder material in the thermal boundary layer

as thoroughly as in the other cases. Figure 4.15c has features of stagnant lid drips on the left side of the domain and a small avalanche pattern similar to Figure 4.14b on the right side of the domain. Values of r_1 smaller than 0.1 MPa^{-2} tends to drive the dynamics toward the stagnant lid character of the baseline Case 1. For another point of comparison Figure 4.16 displays the isotropic hardening for Cases 6, 7, and 8 at 170 Myr. As expected the recrystallization reduces the magnitude of the isotropic hardening in the thermal boundary layer. The average isotropic hardening in the coldest (uppermost) part of the boundary layer for Cases 6, 7, and 8 is about 700 MPa, 3,000 MPa, and 10,000 MPa, respectively. This is why Case 8 had stagnant lid characteristics, because the stresses involved where over 10,000 MPa, which is an order of magnitude beyond the limiting 800 MPa strength of the oceanic lithosphere (Kohlstedt *et al.*, 1995).

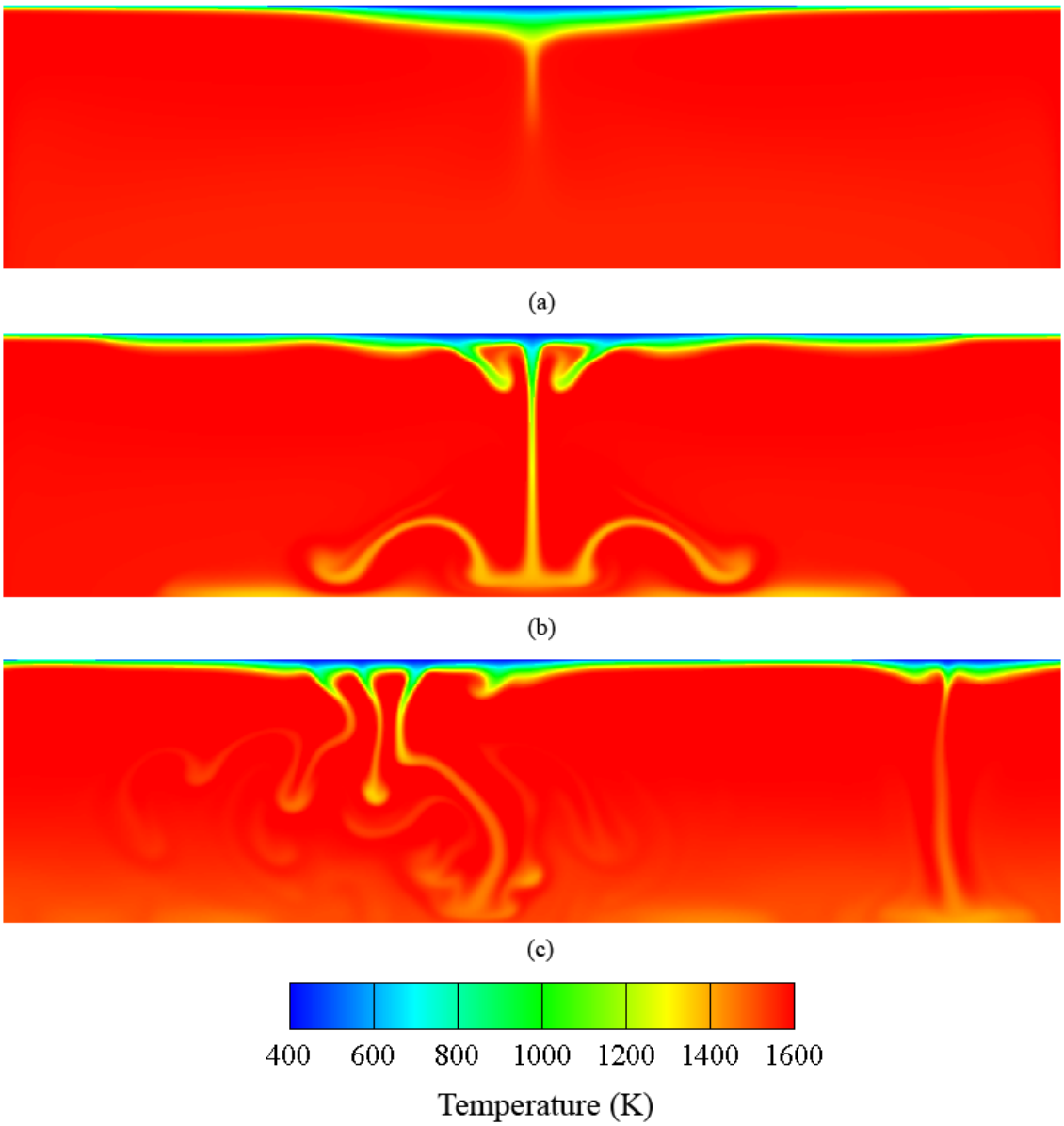

Figure 4.15 Temperature fields for Case 8 with recrystallization parameter $r_1 = 0.1$ MPa^{-2}. Snapshots in time at a) 50 Myr, b) 200 Myr, and c) 700 Myr.

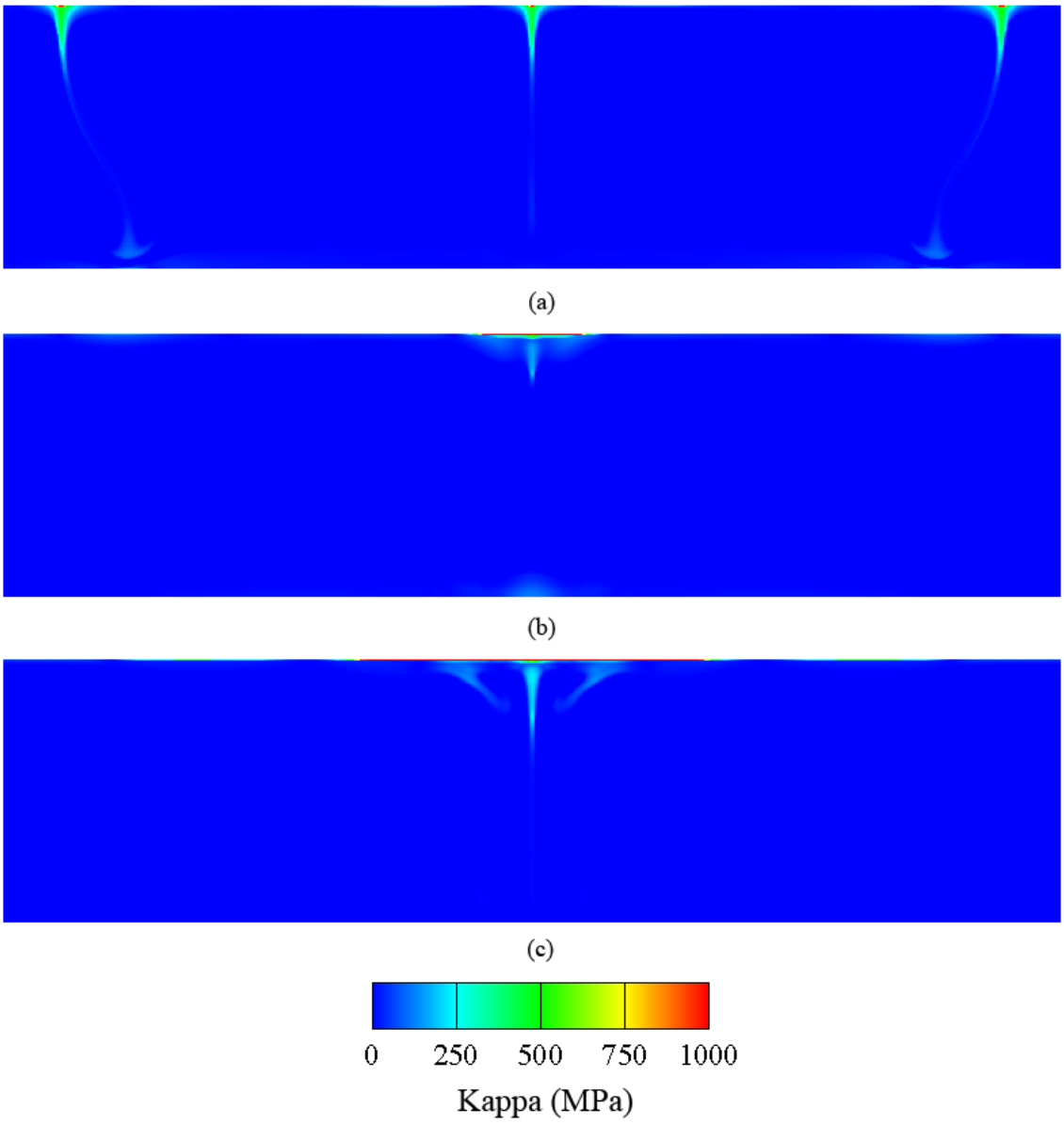

Figure 4.16 Isotropic hardening fields for the three recrystallization cases at 170 Myr for a) r_1 = 1000 MPa^{-2}(Case 6), b) r_1 = 10 MPa^{-2}(Case 7), and c) r_1 = 0.1 MPa^{-2}(Case 8).

Next we turn attention to the texture cases listed in Table 4.4. These cases differ only in the manner in which they are initialized. Case 9 has no initial texture. Figure 4.17 displays snapshots of the temperature field from this case at three different times.

Comparing Figure 4.17 with Figure 4.6 we observe that the inclusion of texture clearly affects the dynamics of the flow. With this texture capability, we can use the stress states and texture development from other cases to initialize new cases. One can choose initial ISV texture values, for example, corresponding to plane strain conditions similar to those that arise from the rolling of a metal sheet. Cases 10 and 11 contain such initial states for the texture ISV. Figure 4.18 shows the case for Case 10, which has an initial plane strain compression history, while Figure 4.19 displays the case for Case 11, which has an initial shear history. One of the characteristic common to all three texture cases is that texture alone is not effective in completely mobilizing the thermal boundary layer. While the warmer material in the boundary layer has a tendency to plunge downward more frequently than in the baseline case, the colder material tended to remain. The initial history affects the beginning part of the time history, but eventually all three texture cases display qualitatively similar dynamics. The shear initialization has the most dramatic effect on the initial flow as can be observed by comparing Figure 4.19a with Figure 4.17a and Figure 4.18a. One other noteworthy feature of these texture cases is the increased level of rotational flow throughout the domain due to the torsional softening, similar to that observed by Dawson and Wenk (2000), who used a crystal plasticity formulation. Figure 4.20 shows this increased rotational flow relative to the baseline case in all the three texture cases. We expected an increase in rotational flow because the texture model includes an additional rotational degree of freedom that arises from the inelastic spin in Equation (4.26). Figure 4.21 plots the ISV tensor component A_{12} that reflects the degree of texture development from the three texture cases to compare the different textures in the three cases. These cases illustrate that texture does indeed influence flow dynamics.

Furthermore, they illustrate that if one desires a model with history dependence to predict the future, initial conditions that reflect the system's previous history can play an important role.

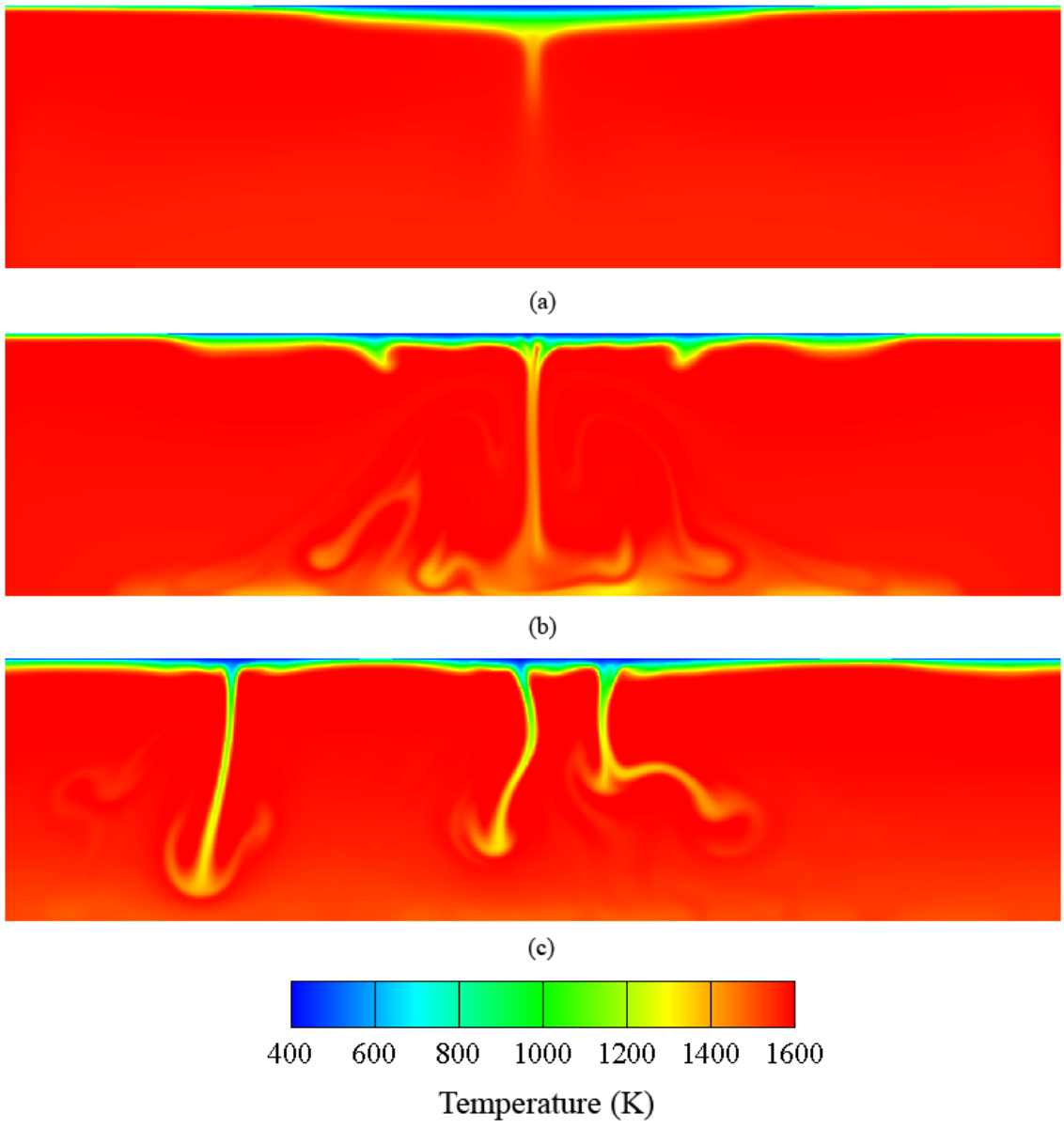

Figure 4.17 Temperature fields for Case 9 with texture development and no initial texture. Snapshots in time at a) 50 Myr, b) 200 Myr, and c) 600 Myr.

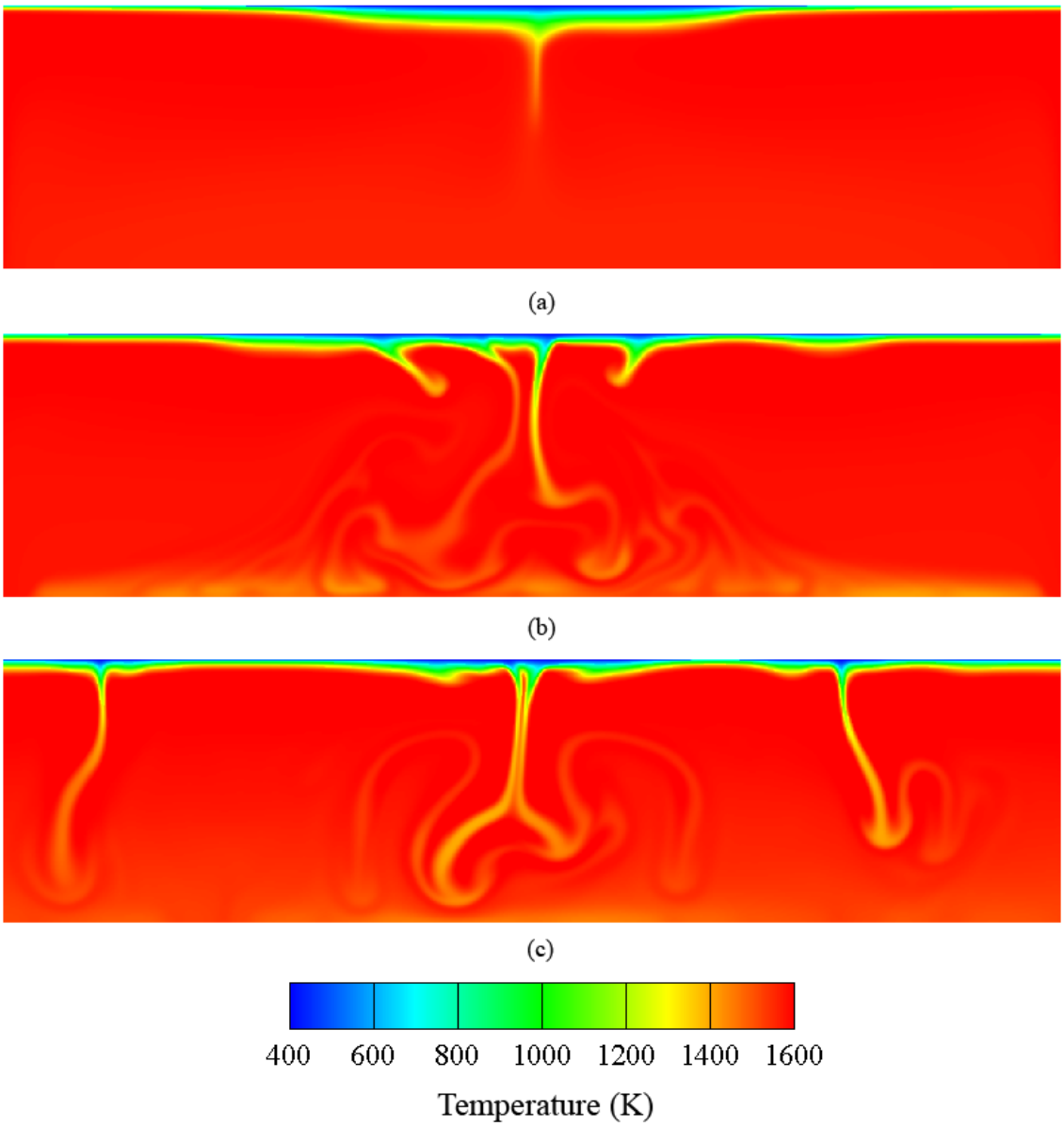

Figure 4.18 Temperature fields for Case 10 with texture development and initial plane strain texture. Snapshots in time at a) 50 Myr, b) 200 Myr, and c) 600 Myr.

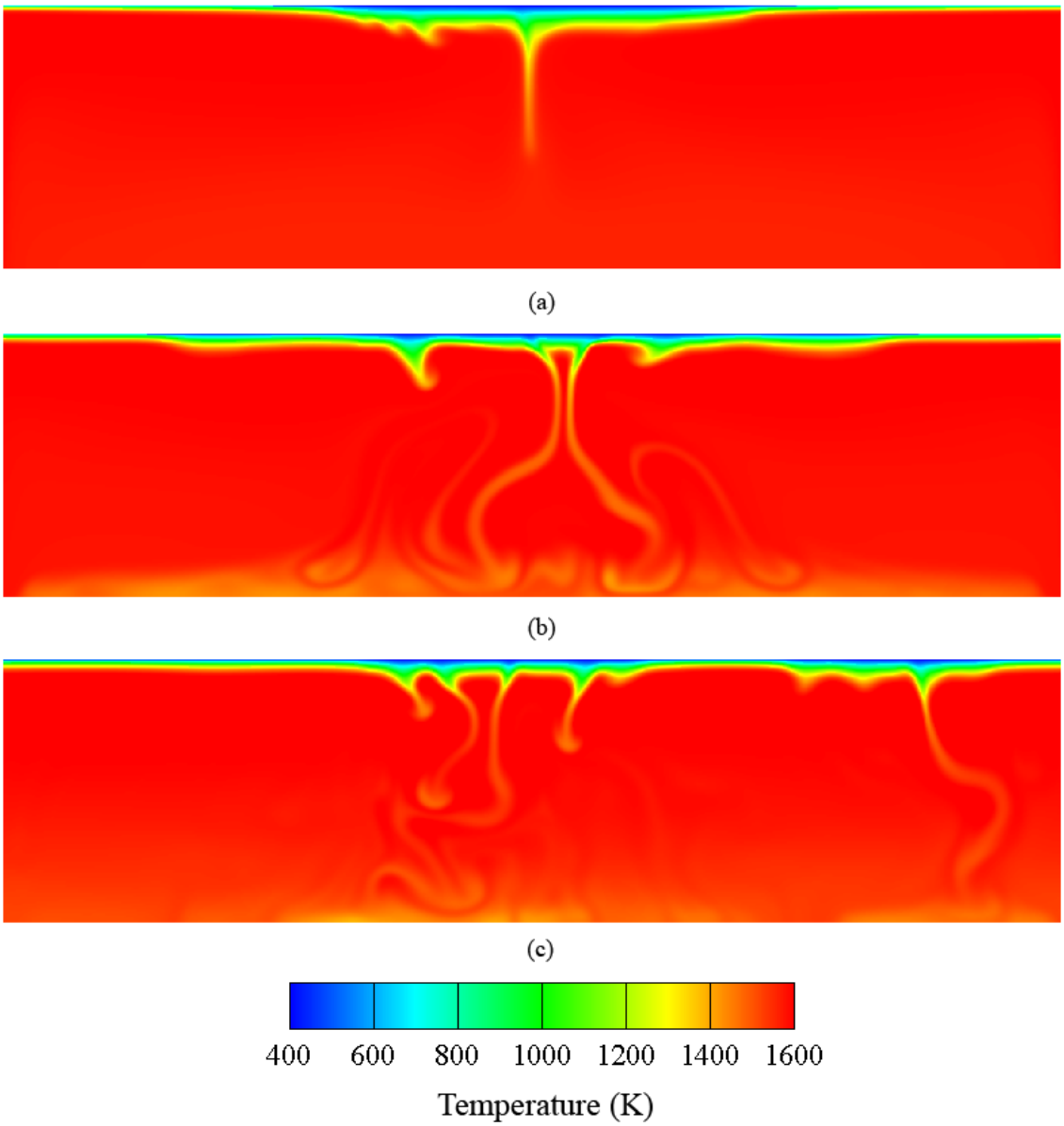

Figure 4.19 Temperature fields for Case 11 with texture development and initial shear texture. Snapshots in time at a) 50 Myr, b) 200 Myr, and c) 600 Myr.

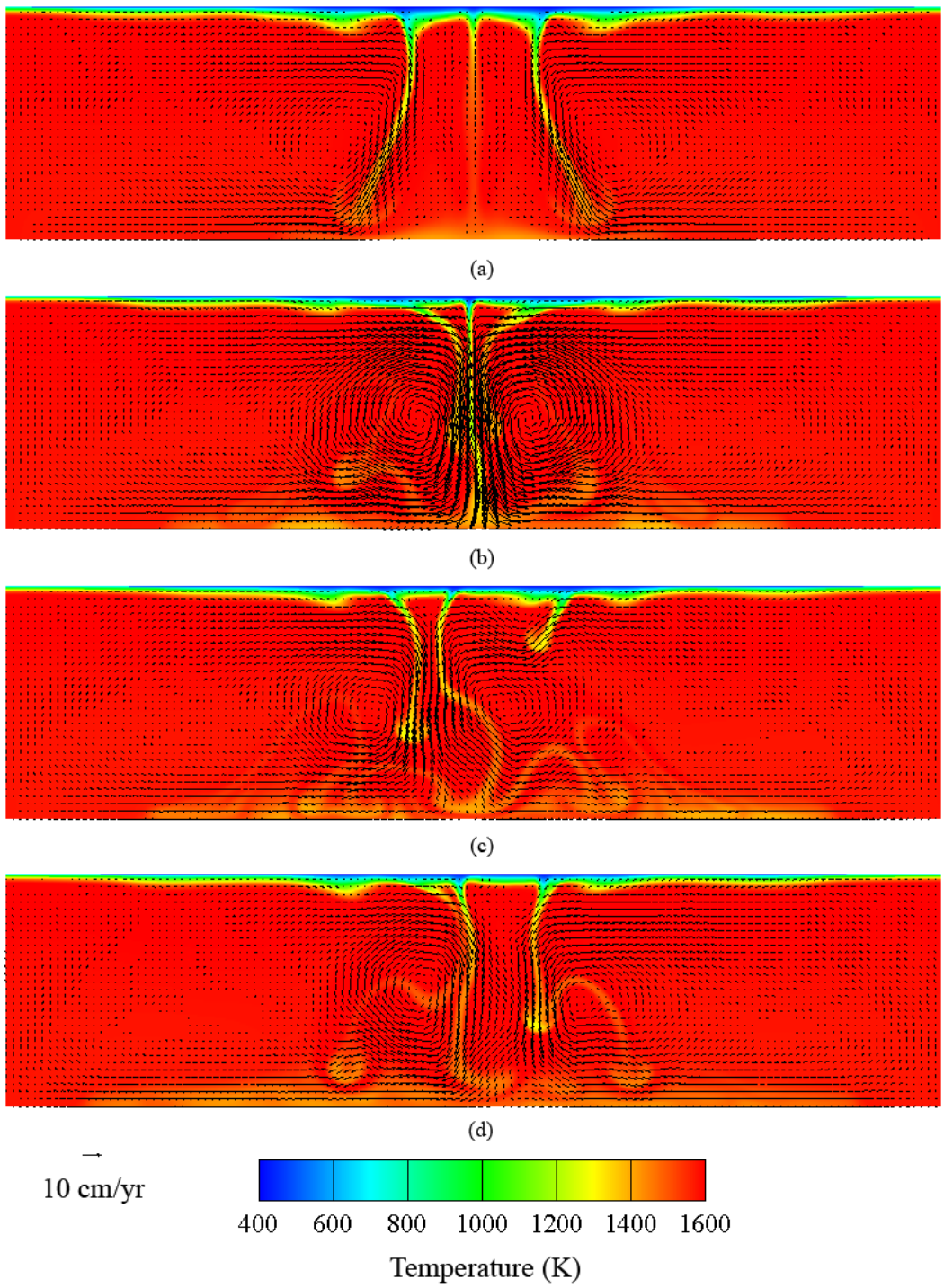

Figure 4.20. Plots of velocity and temperature fields for texture cases at 180 Myr for a) no texture (Case 1), b) texture model with no initial history (Case 9), c) texture model with plane strain initial history (Case 10), and d) texture model with shear initial history (Case 11). Reference velocity vector is located in bottom left corner.

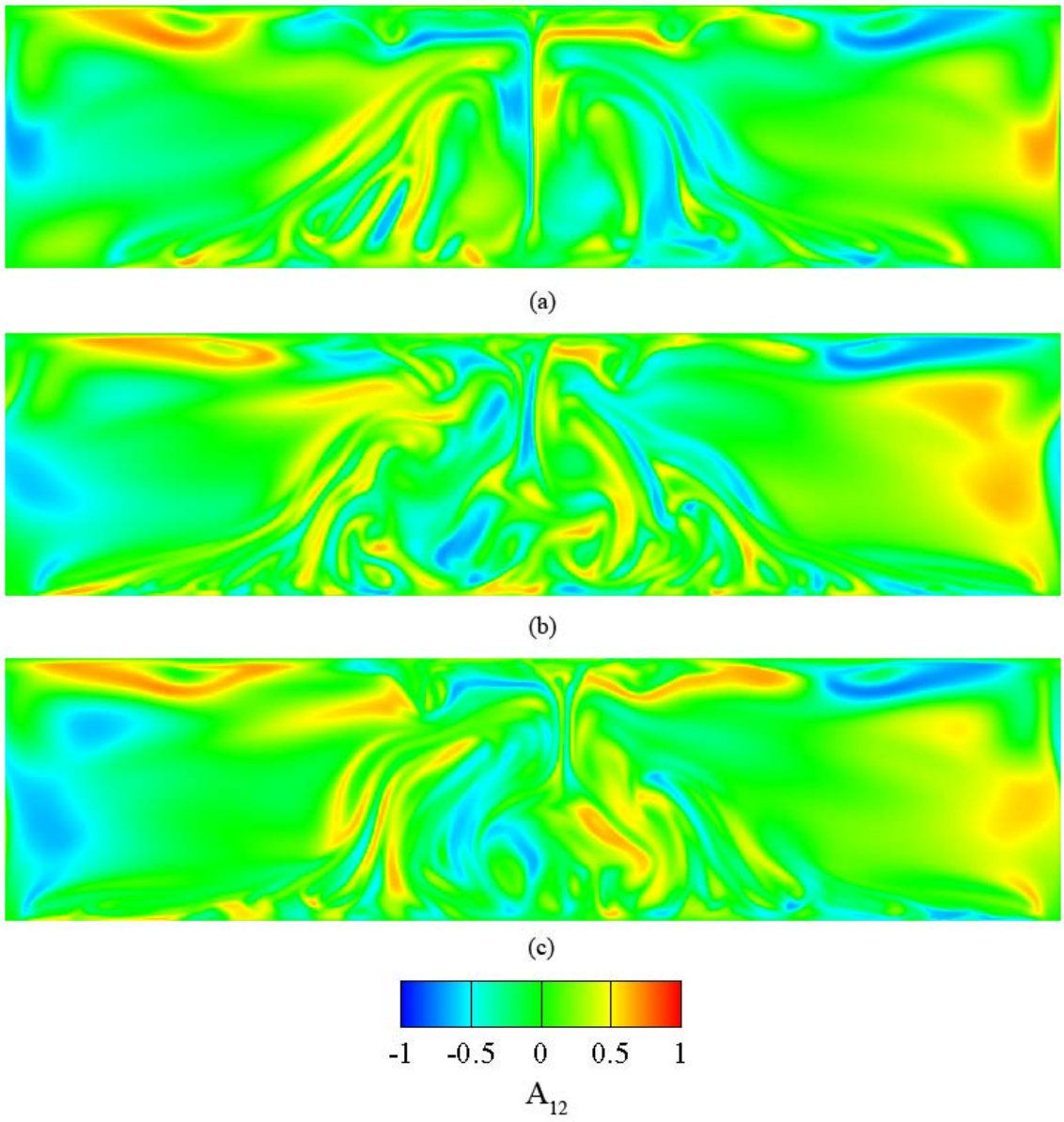

Figure 4.21. Plots of ISV tensor component A_{12} (a measure of texture development) for the different texture cases at 180 Myr for a) no initial history (Case 9) b) plane strain compression initial history (Case 10), and c) shear initial history (Case 11).

The final case, Case 12, combines the damage, recrystallization, and texture treatments to explore the consequences when all are included. We carefully chose the damage and recrystallization parameter values listed in Table 4.4 so each of the

weakening mechanisms would be active We also included a shearing initial history for the texture ISV for illustrative purposes. Figure 4.22 displays the different aspects of this mixed treatment case. This case displays characteristics of all three treatments. For instance, Figure 4.22a looks similar to a mixture of shear history in Figure 4.19a and recrystallization in Figure 4.14a. Figure 4.22b has aspects of both damage and recrystallization treatments as revealed by comparing with Figures 4.7b and 4.8b in regard to damage and Figure 4.19b in regard to recrystallization. Figures 4.23 and 4.24 display the fields for damage accumulation and the A_{12} component of the texture ISV, respectively. Notice in Figure 4.23 that damage accumulation is everywhere far from the saturation value of 0.99. Finally, Figure 4.25 shows the velocity field at different times and reveals the strong rotational flow characteristic of strong texture development. Case 12 displays the three treatments' ability to work together to produce a rich diversity of dynamical regimes.

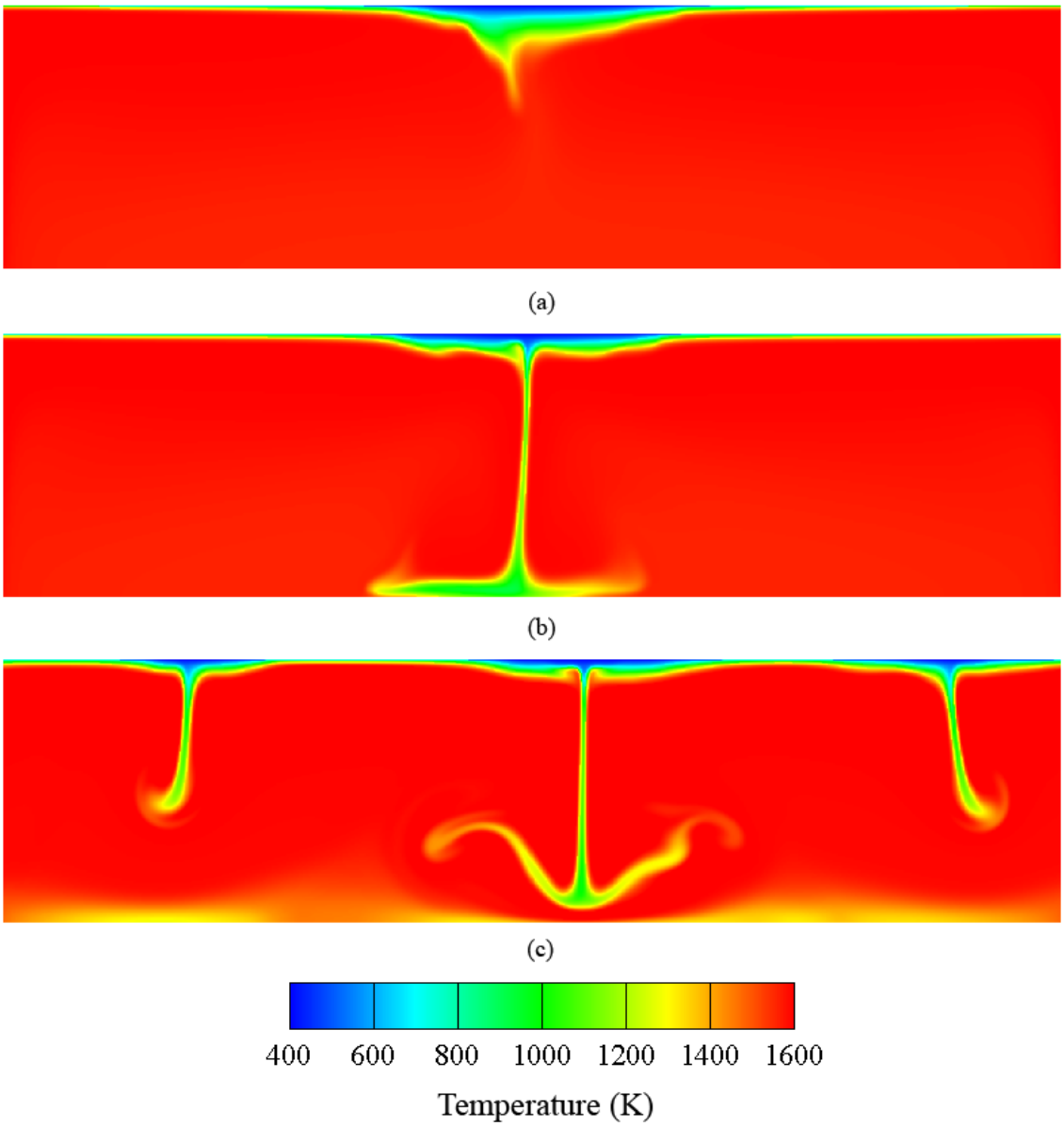

Figure 4.22 Temperature fields for Case 12 with damage, recrystalization, and texture all active. Snapshots in time at a) 30 Myr, b) 50 Myr, and c) 300 Myr.

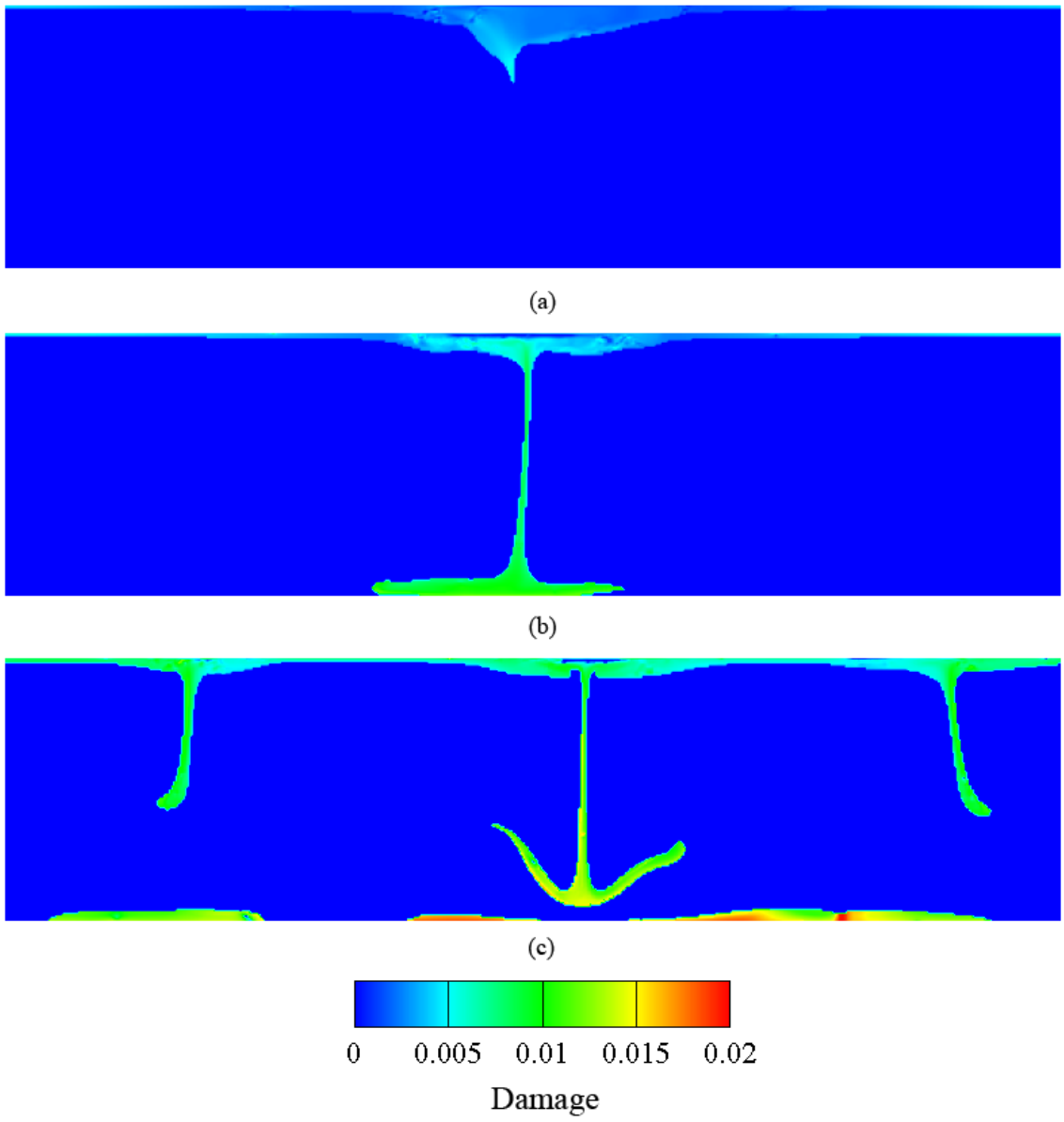

Figure 4.23 Plots of damage accumulation for Case 12 with damage, recrystallization, and texture all active. Snapshots in time at a) 30 Myr, b) 50 Myr, and c) 300 Myr.

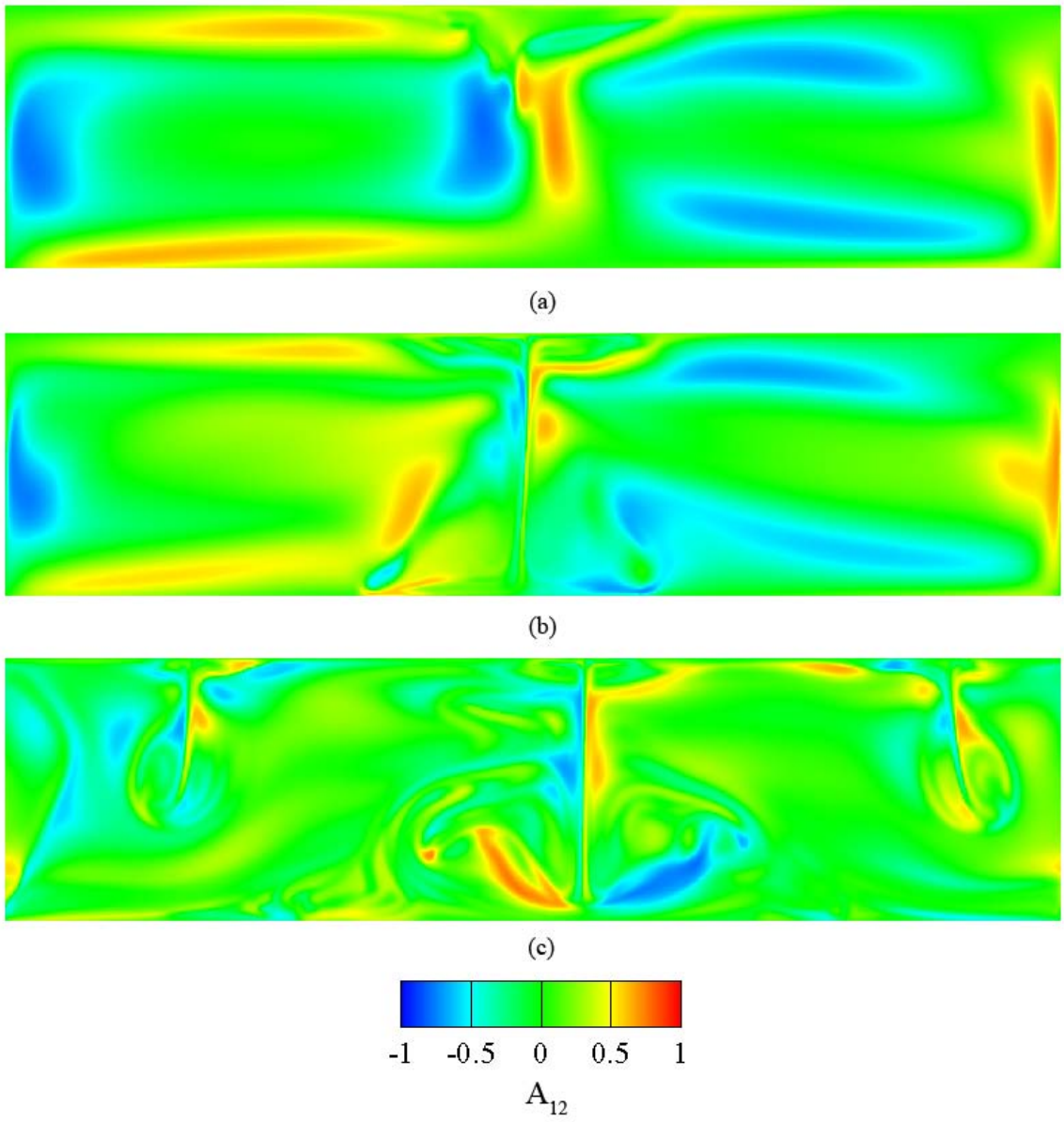

Figure 4.24 Plots of the ISV tensor component A_{12} (a measure of texture development) for Case 12 with damage, recrystalization, and texture all active. Snapshots in time at a) 30 Myr, b) 50 Myr, and c) 300 Myr.

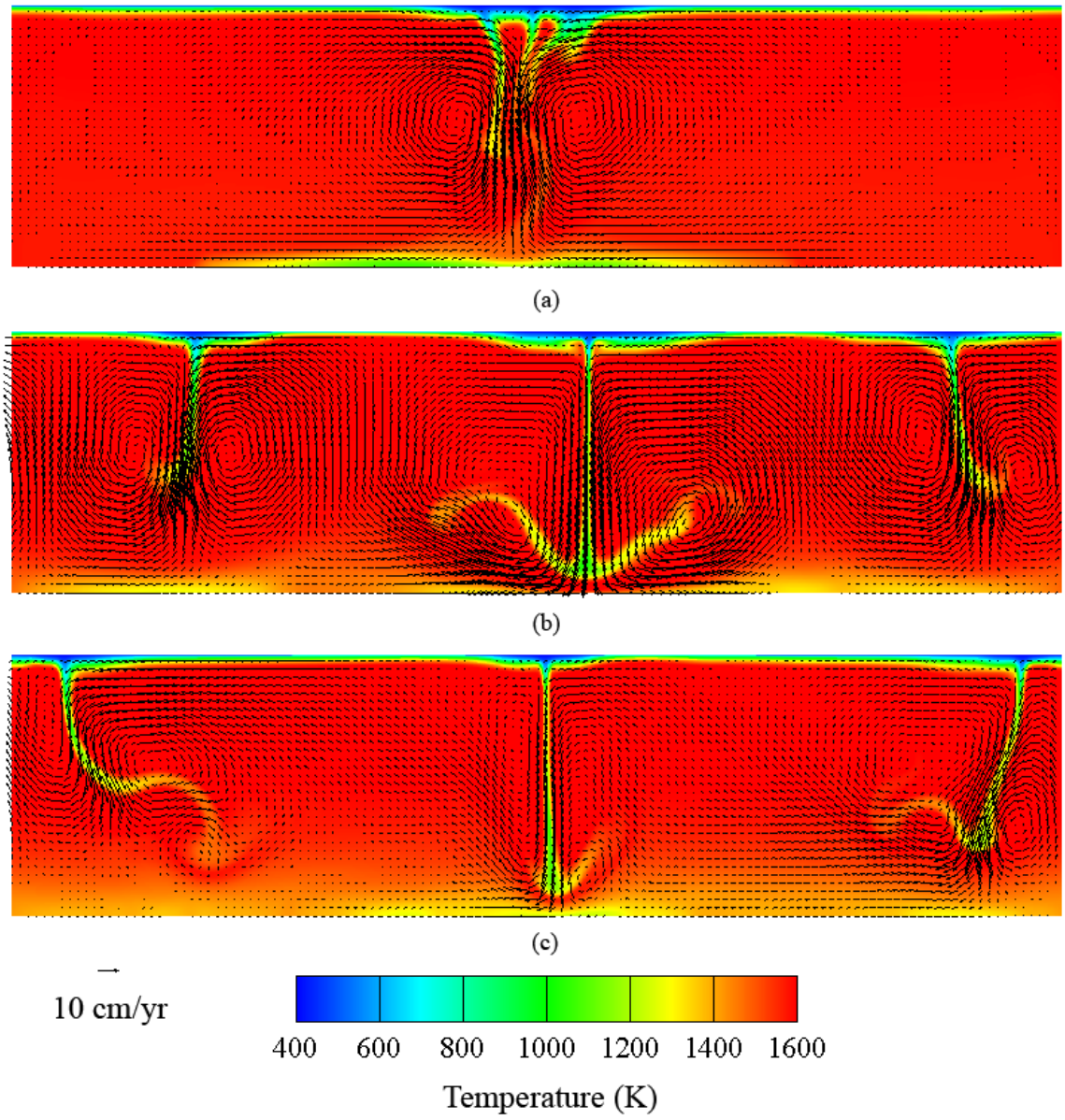

Figure 4.25 Plots of velocity and temperature fields for Case 12 with damage, recrystalization, and texture all active. Snapshot in time at a) 120 Myr, b) 300 Myr, and c) 530 Myr. Reference velocity vector is in lower left corner.

Discussion and Conclusions

An implication of the mixed treatment case is a possible mechanism for deep focus earthquakes. Deep focus earthquakes have been a conundrum to earth scientists

since their discovery by Wadati (1927). Deep focus earthquakes occur below 300 km in the earth, and due to high pressures and temperatures the brittle fracture mechanism that causes shallow earthquakes is unlikely (Karato, 2003). Many mechanisms have been proposed regarding the origin of these earthquakes (Karato, 2003), but the predominant theory is a thermal runaway instability (adiabatic instability) proposed by many researchers (Griggs & Baker, 1969; Hobbs *et al.*, 1986; Ogawa, 1987; Hobbs & Ord, 1988; and Karato *et al.*, 2001) which will be briefly discussed here.

Thermal runaway instability occurs due to an energy release followed by subsequent weakening from a temperature increase. First inelastic deformation due to a high strain rate dissipates energy which then increases the local temperature in a material. The local increase in temperature enhances the inelastic deformation which in turn can lead to unstable deformation of the material. The faulting that follows the unstable deformation is thus due to a ductile failure mechanism. The weakening mechanisms described in this paper are also ductile failure mechanisms that could conceivably produce similar unstable deformation at deep earthquake depths between 300 km and 680 km.

One of the characteristics of deep earthquakes is the low number of aftershocks compared to shallow earthquakes. The thermal runaway instability mechanism would explain the low number of aftershocks by the partial melting produced by the deformation would release most of the built up stress along a fault plane. The large reduction of stress would not allow many subsequent aftershocks to occur. In a similar manner the recrystallization model presented here admits the possibility for a quick reduction of stress followed by no aftershocks. The recrystallization model inherently

allows for a reduction of stress once the hardening reaches a critical value. Past this critical value the hardening is reduced, but reaches a new steady state value as shown in Figure 4.3. The localization of a deep earthquake with this recrystallization model would occur by first reaching this critical stress that then causes the material to weaken quickly. The material would continue to weaken until the new steady state is reached which would then continue to deform, but not in a catastrophic softening sense. In the same fashion the damage model would have a similar effect to reduce a large amount of stress and would not leave any residual stresses for aftershocks to arise. More research must be done to show exactly how the weakening described in this paper could admit this type of behavior on a large slab.

The illustrative cases carried out in this study demonstrate the flexibility of the BIISV model to include texture, damage, and recrystallization effects in mantle dynamics investigations. These cases reveal that the damage treatment can mobilize the cold thermal boundary layer in an effective manner. Similarly we show that the recrystallization treatment, by diminishing the isotropic hardening also can assist in mobilizing the otherwise very strong thermal boundary material. The texture treatment adds a new material rotational degree of freedom that increases rotational flow around descending material. Combining these treatments offers a much more complete rheological framework which is able to utilize material history ought to enable some new discoveries in the dynamics of the earth's interior. It is conceivable that it could provide new insights into the mechanism responsible for deep focus earthquakes.

Future work involves improving many aspects of the BIISV framework enhanced with the texture, damage, and recrystallization. The influence of pressure on the damage

model is but one example. An urgent need is the experimental determination of the material parameters for mantle minerals and rocks for the inelastic constants as well as the new parameters described in this study. Obviously there is strong incentive to implement the enhanced BIISV model with the texture, damage, and recrystallization treatments into a 3D code to explore the rich 3D dynamics impossible to address in 2D. In the meantime there are many interesting problems to investigate in 2D with the existing framework.

References

Ashby, M.F., 1970. The deformation of plastically non-homogeneous materials, *Philos. Mag.*, **21**, 399-424.

Auth, C., Bercovici, D. & Christensen U.R., 2003. Two-dimensional convection with a self-lubricating, simple-damage rheology, *Geophys. J. Int.*, **154**, 783-800.

Ave'Lallemant, H.G. & Carter, N.L., 1970. Syntectonic Recrystallization of Olivine and Modes of Flow in the Upper Mantle, *Geol. Soc. Am. Bull.*, **81**, 2203-2220.

Bammann, D.J. & Aifantis, E.C., 1987. A model for finite deformation plasticity, *Acta Mech.*, **69**, 97-117.

Bammann, D.J., 1990. Modeling temperature and strain rate dependent large deformations of metals. *Appl. Mech. Rev.*, **1**, 312-318.

Bammann, D.J., Chiesa, M.L., Horstemeyer, M.F. & Weingarten, L.I., 1993. Failure in ductile materials using finite element methods, in *Structural Crashworthiness and Failure*, eds. Jones, N. & Weirzbicki, T., Elsevier Applied Science.

Ben Ismail, W. & Mainprice, D., 1998. An Olivine Fabric Dababase: An Overview of Upper Mantle Fabrics and Seismic Anisotropy, *Tectonophysics*, **296**, 145-157.

Bercovici, D., 1998. Generation of plate tectonics from lithosphere-mantle flow and void-volatile self-lubrication, *Earth Planet. Sci. Lett.*, **154**, 139-151.

Bercovici, D. & Karato, S., 2002. Theoretical Analysis of Shear Localization in the Lithosphere, in *Reviews in Mineralogy and Geochemistry*, Vol. 52, pp. 387-420, eds. Karato, S. & Wenk, H.-R., Mineralogical Society of America, Washington DC.

Blackman, D.K., Kendall, J.M., Dawson, P.R., Wenk, H.-R., Boyce, D. & Morgan, J.P., 1996. Teleseismic Imaging of Subaxial Flow at Mid-Ocean Ridges: Traveltime Effects of Anisotropic Mineral Texture in the Mantle, *Geophys. J. Int.*, **127**, 415-426.

Blackman, D.K. & Kendall, J.M., 1997. Sensitivity of Teleseismic Body Waves to Mineral Texture and Melt in the Mantle Beneath a Mid-Ocean Ridge," *Phil. Trans. A. - Math. Phys. and Eng. Sci.*, **355**, 1723, 217-231.

Bystricky, M., Kunze, K., Bulini, L. & Burg, J.-P., 2000. High Shear Strain of Olivine Aggregates: Rheological and Seismic Consequences, *Science*, **290**, 1564-1567.

Chastel, Y.B., Dawson, P.R., Wenk, H.-R. & Bennett, K., 1993. Anisotropic convection with implications for the upper mantle, *J. Geophys. Res.*, **98**, 17,757-17,771.

Cocks, A.C.F. & Ashby, M.G., 1980. Intergranular fracture during power-law creep under multiaxial stresses, *Metal Science*, **14**, 395-402.

Cohen, R.E., ed., 2005. High-Performance Computing Requirements for the Computational Solid Earth Sciences, 94 pp., http://www.geo-prose.com/.

Covey-Crump, S.J., 1997. The high temperature static recovery and recrystallization behavior of cold-worked Carrara marble, *J. Struct. Geol.*, **19**, 2, 225-241.

Dawson, P.R. & Wenk, H.-R., 2000. Texturing of the upper mantle during convection, *Phil. Mag. A*, **80**, 3, 573-598.

Downes, H., Embeyisztin, A. & Thirwall, M.F., 1992. Petrology and Geochemistry of Spinel Peridotite Xenoliths from the Western Pannonian Basin (Hungary) - Evidence for an Association between Enrichment and Texture in the Upper Mantle, *Contributions to Mineralogy and Petrology*, **109**, 3, 340-354.

Griggs, D.T. & Baker D.W., 1969. The origin of deep-focus earthquakes, in *Properties of Matter Under Unusual Conditions*, pp. 23-42, eds. Marks, H. & Feshbach, S., Interscience.

Hall, E.O., 1951. The deformation and ageing of mild steel: III. Discussion of results, *Phys. Soc. Lond.*, **64**, 747-753.

Hobbes, B.E. & Ord, A., 1988. Plastic instabilities: implications for the origin of intermediate and deep focus earthquakes, *J. Geophys. Res.*, **89**, 10521-10540.

Hobbes, B.E., Ord, A. & Teyssier, C., 1986. Earthquakes in the ductile regime, *Pure and Appl. Geophys.*, **124**, 310-336.

Horstemeyer, M.F. & McDowell, D.L., 1998. Modeling Effects of Dislocation Substructures in Polycrystal Elastoviscoplasticity, *Mech. Matls.*, **27**, 145-163.

Horstemeyer, M.F. & Gokhale, A.M., 1999. A void-crack nucleation model for ductile metals, *Int. J. Solids Struct.*, **36**, 5029-5055.

Horstemeyer, M.F., Lathrop, J., Gokhale, A.M. & Dighe, M., 2000. Modeling stress state dependent damage evolution in a cast Al-Si-Mg aluminum alloy, *Theor. Applied Fract. Mech.*, **33**, 31-47.

Hughes, D.A., 1992. Microstructure and Flow Stress of Deformed Polycrystalline Metals, *Scripta Metall*, **27**, 969-974.

Hughes, D.A., 1993. Microstructural Evolution in a Non-Cell Forming Material: Al-Mg, *Acta Metall. et Mater.*, **41**, 1421-1430.

Kachanov, L.M., 1958. Time of the Rupture Process under Creep Conditions, *IVZ Akad. Nauk. S.S.R., Odt Tech Nauk*, **8**, 26-31.

Karato, S., 2003. *The Dynamic Structure of the Deep Earth*, pp. 241, Princeton University Press, Princeton, New Jersey.

Karato, S., Riedel, M.R. & Yuen, D.A., 2001. Rheological structure and deformation of subducted slabs in the mantle transition zone: implication for mantle circulation and deep earthquakes, *Phys. Earth Planet. Interiors*, **127**, 83-108.

Kohlstedt, D.L., Evans, B. & Mackwell, S.J., 1995. Strength of the lithosphere: Constraints imposed by laboratory experiments, *J. Geophys. Res.*, **100**, B9, 17587-17602.

Krieg, R.D. & Krieg, D.B., 1977. Accuracies of numerical solution methods for the elastic-perfectly plastic model, *ASME J. Pressure Vessel Technol.*, **99**, 510-515.

Kulhmann-Wilsdorf, D., 1968. *Work Hardening*, eds. J.P. Hirth, J. Weertman, pp. 97, Gordon and Breach, New York.

Mainprice, D. & Silver, P.G., 1993. Interpretation of SKS-Waves Using Samples from the Subcontinental Lithosphere, *Phys. Earth Planet. Interiors*, **78**, 3-4, 257-280.

McClintock, F.A, 1968. A criterion for ductile fracture by the growth of holes, *ASME J. Appl. Mech.*, **35**, 363-371.

Moresi, L. & Solomatov, V., 1995. Numerical investigation of 2D convection with extremely large viscosity variations, *Phys. Fluids*, **7**, 2154-2162.

Ogawa, M, 1987. Shaer instability in a viscoelastic material as the cause for deep earthquakes, *J. Geophys. Res.*, **92**, 13801-13810.

Ogawa, M., 2003. The plate-like regime of a numerically modeled thermal convection in a fluid with temperature-, pressure-, and stress-history-dependent viscosity, *J. Geophys. Res.*, **108**, 2067-2084.

Petch, N.J., 1953. The cleavage strength of polycrystals, *J. Iron Steel Inst.*, **174**, 25-28.

Poirer, J.P. & Nicolas, A., 1975. Deformation induced recrystallization due to progressive misorientation of subgrains with special reference to mantle peridotites, *J. Geol.*, **83**, 707-720.

Post, R.L., 1977. High-temperature creep of Mt. Burnett dunite, *Tectonophysics*, **42**, 75-110.

Prantil, V.C., Jenkins, J.T. & Dawson, P.R., 1993. An Analysis of Texture and Plastic Spin for Planar Polycrystals, *J. Mech. Phys. Solids*, **41**, 8, 1357-1382.

Rabotnov, I.N., 1963. On the equations of state for creep, *Progress in Applied Mechanics-The Prager Anniversary Volume*, 307-315.

Solomatov, V.S., 2001. Grain size-dependent viscosity convection and the thermal evolution of the Earth, *Earth Plant. Sci. Lett.*, **191**, 203-212.

Solomatov, V.S., El-Khozondar, R. & Tikare, V., 2002. Grain size in the lower mantle: constraints from numerical modeling of grain growth in two-phase systems, *Phys. Earth Plant. Interiors*, **129**, 265-282.

Solomatov, V.S. & Reese, C.C., 2008. Grain size variations in the Earth's mantle and the evolution of primordial chemical heterogeneities, *J. Geophys. Res.*, **113**, B07408, doi:10.1029/2007JB005319.

Tackley, P., 2000. Self-consistent generation of tectonic plates in time-dependent, three-dimensional mantle convection simulations, 2. Strain weakening and asthenosphere, *Geochem. Geophys. Geosystems*, **1**, 1026, doi:10.1029/2000GC000043.

Tome, C. & Kocks, U.F., 1985. The yield surface of HCP crystals, *Acta Metall.*, **33**, 4, 603-621.

Tullis, J. & Yund, R.A., 1985. Dynamic recrystallization of feldspar: a mechanism of shear zone formation, *Geology*, **13**, 238-241.

Wadati, K., 1927. Existence and study of deep earthquakes, *J. Meteorol. Soc. Jpn.*, **2**, 5, 119-145.

Wenk, H.-R. & Tomé, C.N., 1999. Modeling dynamic recrystallization of olivine aggregates deformed in simple shear, *J. Geophys. Res.*, **104**, B4, 25,513-25,527.

Xu, Y., Menzies, M.A., Vroon, P., Mercier, J.C. & Lin, C., 1998. Texture-Temperature-Geochemistry Relationships in the Upper Mantle as Revealed from Spinel Peridotite Xenoliths from Wangqing, NE China, *J. Petrology*, **39**, 3, 469-493.

Yang, W. & Baumgardner, J.R., 2000. A Matrix-Dependent Transfer Multigrid method for Strongly Variable Viscosity Infinite Prandtl Number Thermal Convection, *Geophys. Astrophys. Fluid Dynamics*, **92**, 151-195.

Zeuch, D.H., 1982. Ductile faulting, dynamic recrystallization and grain-size-sensitive flow in olivine, *Tectonophysics*, **83**, 293-308.

Zeuch, D.H., 1983. On the inter-relationship between grain size sensitive creep and dynamic recrystallization of olivine, *Tectonophysics*, **93**, 151-168.

Zhang, S., Karato, S., Gerald, J.F., Faul, U.H. & Zhou, Y., 2000. Simple shear deformation of olivine aggregates, *Tectonophysics*, **316**, 133-152.

CHAPTER V

CONCLUSIONS AND FUTURE WORK

Conclusions

Using the BIISV model as the starting point we developed an internal state variable model to include damage, recrystallization, and texture development effects to increase the relevant material physics in mantle convection simulations that the conventional simple power law model cannot capture. The enhanced BIISV model developed in this study represents a self consistent way to model the deformation of geologic materials. The mantle convection simulations performed and described in this study provide insight into our understanding of mantle dynamics that have been ignored by the power law model traditionally used. With just the inclusion of the BIISV model, hardened areas in the cold thermal boundary layer developed giving rise to long lived zones that diverted cold mantle material downward. When damage, recrystallization, and texture development were added the new enhanced BIISV model provided necessary weakening mechanisms for the cold thermal boundary layer to break up and sink downward. We also showed the enhanced BIISV model can handle different initialized history through the use of the ISVs. Mantle simulations can now be initialized with a past deformational history allowing for other mantle processes to be understood. The enhanced BIISV model represents a substantial advance in realistically modeling mantle materials, which could ultimately aid in our limited understanding of the earth's interior.

Future Work

Three Dimensional Implementation

Mantle convection is inherently a three dimensional process. The two dimensional simulations presented in this thesis are useful for development and understanding purposes, but a three dimensional implementation must be addressed. We will eventually implement the enhanced BIISV model into TERRA, which is a 3D spherical version of TERRA2D. This will become more feasible as computational power increases.

Heterogeneous Grain Sizes

With the inclusion of the recrystallization model described in Chapter 4, it is possible to alter the formulation to include an evolving grain size. With grain size being tracked and included, we could see how different initializations of heterogeneous grain size distributions could affect mantle dynamics.

Pressure Dependence

Currently, the model presented here does not address pressure dependence on the deformation of a material. The pressure effects should be included in the flow rule, because geologic materials begin to yield at different stresses depending on how high the applied hydrostatic pressure is. We would like to use the pressure dependent model by Hammi *et al.* (2008), which included a pressure dependence on the deformation and applied it to powder metals. All geologic materials have some sort of pressure dependence that should be included in the enhanced BIISV model especially those materials near the earth's surface. Also damage's growth due to pressure effects warrants

further research due to the large pressures in the mantle. We would also like to move away from the Boussinesq approximation and use more advanced equations of state in conjunction with the enhanced BIISV model.

Quantifying Heat Released During Avalanche Event

In the previous chapters the enhanced BIISV model does not consider heat released due to deformation. This should be included in a future variation of the model because materials dissipate energy when they are under deformation. In this same line of thinking it would be advantageous to quantify the amount of heat energy released due to a single avalanche, which should be straightforward to determine because of the multiple ISVs tracked throughout the mantle convection simulations.

Model Constants for Olivine

The BIISV model constants used in most of the simulations were for lherzolite, which contains 60%-70% olivine. We desire to have a larger range of temperatures and strain rates to come up with better constants than those determined in Chapter 2. Many experiments will be required to produce a better set of constants. Also realistic constants that have the both the elastic-plastic constants are desirable.

Initialization of Damage and Thermal Cracks

As seen in Chapter 4, damage can play a large role in breaking up the cold thermal boundary layer. In order to better understand damage and its influence on localization in this layer, different levels of damage should be initialized in the cold upper boundary layer. This should also be supplemented with finite element calculations on

subscale lithospheric material to see how thermal cracks could develop with the enhanced BIISV model. The thermal cracks developed in finite element calculations could then be used as initial conditions for a larger scale three dimensional TERRA simulation.

Multiple Materials

Currently, TERRA2D and the enhanced BIISV model only allow for one material to be included in the calculation. In reality the mantle has phase changes that begin around 440 km deep and multiple other materials that should be considered. We would like to modify TERRA2D to be able to have more than one material involved in the simulations. With multiple materials we could conceivably consider effects such as the difference between oceanic lithosphere and continental lithosphere, which have completely different material behavior. We also would like to include some sort of phase change model that could capture the multiple phase changes that happen to olivine at depths greater 440 km.

Relationship between Recrystallization and Texture

In the formulation done in Chapter 4 we assumed recrystallization and texture development were two completely decoupled mechanisms. Physically this is not the case. Recrystallization actually produces a highly textured microstructure in materials like olivine. We would like to determine the relationship between recrystallization and texture in order to include this into the enhanced BIISV model. We will need to design and perform experiments to determine this relationship.

Kinematic Hardening

For the constants found in Chapter 2 we chose to fit only the isotropic hardening constants. We would like to design and perform experiments that could allow the fitting of the kinematic hardening constants. The kinematic hardening constants were also excluded in Chapters 3 and 4. One of the reasons for this exclusion was kinematic hardening produced numerical instabilities that were never resolved. We would like to investigate possibly implementing higher order advection schemes that could advect the kinematic hardening without the instabilities. It also could be conceivable to implement a particle in cell method that would not have the same instabilities that the advection schemes inherently have.

Relate Texture Development to Seismic Anisotropy

As discussed in Chapter 4 texture has mostly been studied from a seismic anisotropy approach. We would like to relate the texture ISV determined here to seismic anisotropy found in the earth. In the formulation described in Chapter 4, texture realigns the elastic modulus. The seismic wave speed is related to the elastic modulus so it is conceivable to measure how much realignment the elastic modulus experiences. A simulation would then be possible to initialize the mantle domain with real seismic data found in the earth.

Deep Earthquake Study

We would like to understand how the recrystallization and damage model presented here could be a possible mechanism for deep focus earthquakes. Subscale finite element calculations using the TERRA simulations to provide the subscale boundary

conditions could be performed with a static slab using the enhanced BIISV model in order to study the possible mechanisms of deep focus earthquakes. This could also aid in showing the utility of using an ISV model in other types of geologic structure applications besides mantle convection simulations.

Length Scales

Introducing softening into a model brings up the possibility of mesh dependency on the numerical solution. We would like to include some nonlocal terms into the damage and recrystallization models in order to eliminate the mesh dependency and see possibility of adiabatic shear bands emerging in the upper mantle. We would also like to study the length scale changes from introducing the new parameters.

Shorter Time Scales

We would like to investigate the effect of the imposed minimum viscosity used in this study on time scales involved. For both the power law and BIISV cases the minimum viscosity conditions was always reached, which caused the time for an avalanche to fall to be slowed down. We desire to drop the viscosity minimum and let the model drive the time scales. This could admit the possibility of shorter time scales when an avalanche episode occurs.

References

Hammi, Y., Stone, T.W., Tucker, L. & Horstemeyer, M.F. 2008. Pressure-Dependent Plasticity Model for Powder Metallurgy Compaction. *First American Academy of Mechanics Conference*, New Orleans, June 17-20, 2008.